Journal of
Materials Chemistry A

ROYAL SOCIETY
OF CHEMISTRY

REVIEW

View Article Online
View Journal | View Issue

Check for updates

Cite this: *J. Mater. Chem. A*, 2024, **12**, 10614

Molecular perspective and engineering of thermal transport and thermoelectricity in polymers

Sai C. Yelishala, [a] Connor Murphy[a] and Longji Cui *[abc]

Received 28th December 2023
Accepted 2nd April 2024

DOI: 10.1039/d3ta08071d

rsc.li/materials-a

Designing polymers with desirable thermal or thermoelectric properties has been a great goal in the field of organic functional materials. This is widely considered challenging because polymers manifest complicated transport characteristics due to their intertwined molecular chains, complex intra- and inter-molecular interactions, and strong heterogeneities in both morphology and pathways of primary energy carriers. These molecular- and nano-scale attributes regulate energy transport and conversion, leading to low bulk-level thermal conductivity and moderate thermoelectric energy conversion performance. Polymers with extreme and controllable thermophysical properties hold the potential to advance many thermal management and renewable energy technologies. The past decade has witnessed significant progress on this topic, owing to the advances in micro-, nano-, and molecular-scale engineering that have created polymers with metal-like thermal conductivity for thermal management technologies and polymers with high charge carrier density for thermoelectric applications. This review focuses on molecular perspective and engineering in two key areas: thermoelectric properties in conducting polymers and thermal transport in polymers with phonons as the dominant energy carrier. The review begins with a theoretical explanation of charge and thermal transport in polymers from a molecular and mesoscale perspective. It reviews thermoelectric polymer synthesis and modification methods for increasing thermoelectric efficiency. The later section of the review surveys molecular engineering efforts in optimizing thermal transport in polymers with phonons as the dominant energy carrier and discusses the interrelated charge and thermal transport in conducting polymers. We also summarize recent efforts to study the dynamic control of thermal and thermoelectric properties of polymers using external stimuli. Finally, we discuss some outstanding challenges and potential future directions.

1. Introduction

Designing polymers with desirable thermoelectric or thermal properties represents a formidable challenge. Addressing it requires a molecular and nanoscale engineering approach that starts from the monomer level,[1] as polymers contain

Sai C. Yelishala

Sai Yelishala is pursuing a PhD degree under the supervision of Prof. Longji Cui in the Department of Mechanical Engineering at the University of Colorado Boulder. His research interests include high-resolution scanning thermal probe characterization and fundamental studies of thermal transport and thermoelectric properties in molecular/nanoscale systems and polymers.

Connor Murphy

Connor Murphy is pursuing a thesis MS degree under the supervision of Prof. Longji Cui in the Department of Mechanical Engineering at the University of Colorado Boulder. His research interests include measuring the thermal transport of micro/nanoscale polymer systems.

---

[a] Department of Mechanical Engineering, University of Colorado Boulder, CO 80309, USA. E-mail: longji.cui@colorado.edu
[b] Materials Science and Engineering Program, University of Colorado Boulder, CO 80309, USA
[c] Center for Experiments on Quantum Materials (CEQM), University of Colorado Boulder, CO 80309, USA

amorphous parts that comprise complex molecular chain networks and defects like voids and impurities.[2] These molecular- and nano-scale complex attributes fundamentally regulate charge and energy transport and scattering. For instance, macroscopic thermal conductivity (κ) of polymers is observed only in an ultranarrow range[3–5] of 0.1 to 1 W m^{-1} K^{-1}. This strongly contrasts the measured thermal conductivity of inorganic solids that spans over five orders of magnitude. The low thermal conductivity of polymers[6] could pave the way for high-performance thermal insulation applications[7,8] and enable efficient organic thermoelectric devices for waste heat recovery and renewable power generation.[9–11] Conversely, polymers with extreme and controllable energy transport hold a great potential to advance applications such as thermal interface materials, personal thermal management using fabrics[12,13] and textiles,[14,15] flexible electronics,[16–18] photovoltaic cells,[19] and energy storage.[20]

Polymer thermoelectric devices deliver inexpensive, readily available, and flexible energy conversion[21,22] and heating/cooling systems compared to inorganic devices.[23] Organic semiconductors (OSCs) make wearable thermoelectric devices a reality by opening the pathway to use thermal energy from the human body.[24–26] Despite recent advancements in molecular engineering studies, there is a significant research gap in measuring thermal transport in polymers with high thermoelectric power factors, which is crucial for evaluating thermoelectric efficiency. This research gap is narrowing due to the recent high-resolution experimental techniques, studying thermal transport[27] and thermoelectrics[28] in organic systems with atomic and molecular scale resolutions.

This review focuses on molecular perspective and engineering efforts in two primary transport characteristics of polymers. (1) Charge transport in OSCs that affect the thermoelectric properties of the polymer, like electrical conductivity and Seebeck coefficient. (2) Thermal transport in polymers with phonon as the primary energy carrier. A holistic approach covering both charge and thermal transport from molecular and nanoscale perspectives is missing from previous review articles in this field. It is of great interest to construct a complete physical picture regarding the structure–function relationship in the study of thermoelectricity in polymers. The scope of this review entails only intrinsic polymers with micro- and nano-scale or molecular-scale dimensions engineered to tune the transport and interaction properties directly. An alternative strategy to manipulate the thermal properties of polymers is to create composite materials, which integrate polymers with a diverse set of materials such as metals,[29] ceramics,[30] nanodiamonds,[31] and other inorganic constituents. Several thermally conductive fillers[32] are also highly electrically conductive, rendering the polymer less suited for scenarios requiring electrical insulation[33] and negating a significant advantage over metals. As reviewing composites is beyond the scope of this article, interested readers can refer to in-depth review articles[33–41] published in recent years.

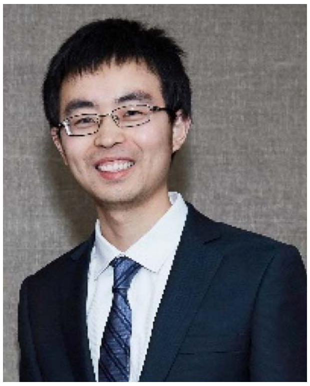

Longji Cui

Longji Cui is an Assistant Professor in the Department of Mechanical Engineering and Materials Science and Engineering program at the University of Colorado Boulder. He received his PhD in Mechanical Engineering from the University of Michigan, Ann Arbor, and did his postdoc research in the Department of Physics and Astronomy and Smalley-Curl Institute at Rice University. His research interests include atomic, molecular, and quantum energy transport and conversion, high-resolution sensing technique, functional scanning probe microscopy, and thermal renewable energy technology.

The structure of this article is as follows: Section 2 describes the basic theoretical framework and numerical modeling methods to understand charge and phonon transport in polymers. Section 3 describes a spectrum of experimental characterization methods to measure the thermal transport of polymers with nano- and micro-scale dimensions. Section 4 summarizes the molecular engineering methods used to create organic semiconducting polymers and increase the thermoelectric power factor. Section 5 explores the molecular effects and engineering endeavors to tune phonon transport in polymers for desired thermal conductivity. It also discusses the interrelated charge and thermal transport in OSCs. Section 6 delves into dynamically controlled transport characteristics under external stimuli such as light,[42] heat, pressure,[43] and humidity.[44] We provide a summary and outlook for future directions in Section 7.

2. Theory

2.1 Landauer formulation for thermoelectricity and thermal transport at the molecular scale

The basic understanding of thermal transport and thermoelectricity at the molecular scale can be formulated in the framework pioneered by Landauer.[45,46] The original picture was based on charge transport in meso- and nano-scale conductors and then generalized to energy transport of phonons and other quasi-particles. Briefly, particles are assumed to be noninteracting within the nanoscale systems and free to propagate before scattering occurs at the lead-conductor interface. Therefore, charge and energy current are proportional to the transmission probability for the particles to transverse the nanoscale structures. Electron transport described by Landauer formulation,[45]

$$I = \frac{2e}{h}\int_{-\infty}^{+\infty}\left(f_{\text{FD}}^{0}(L) - f_{\text{FD}}^{0}(R)\right)\tau_{\text{e}}(E)\text{d}E \tag{1}$$

where L and R are the left and right electrodes, f_{FD}^{0} is the Fermi–Dirac distribution, and $\tau_{\text{e}}(E)$ is the energy-dependent transmission function for electrons. Under a ballistic condition, where no scattering events occur within the molecular region

($\tau_e(E = E_F) = 1$), the electrical conductance (G_e) reduces to $G_e = 2e^2/h$. Here, E_F is the Fermi energy.

The thermoelectrical properties of molecular scale devices can also be understood within the Landauer transport picture. The generation of electrical potential (ΔV) across a material when there is a temperature gradient (ΔT) is described by the Seebeck coefficient (also called thermopower), $S = -\Delta V/\Delta T$, which can be directly related to the transmission coefficient of the nanoscale conductor by,[47,48]

$$S = -\frac{\pi^2 k_B{}^2 T}{3|e|}\frac{\partial \ln(\tau_e(E))}{\partial E}\bigg|_{E=E_F} \tag{2}$$

where k_B is Boltzmann constant, and T is the absolute temperature. The above equation shows that the slope of the transmission function at the Fermi level implies the magnitude of the Seebeck coefficient and the dominant charge carrier (holes or electrons). A positive slope indicates electrons as the major carrier, and a negative slope indicates holes as the major carrier. Studies have shown that a molecular junction can have a high and tunable Seebeck coefficient by engineering molecular structures to create a sharp transition in electron transmission function at the Fermi level.[49,50] The electrical transport of polymers and the associated Seebeck coefficient measurement has been widely studied using different techniques, as seen from recent review papers.[51–53]

Beyond simple electron transport in conventional metals, in semiconducting thermoelectric polymers, the major charge carriers are the quasi-particles known as polarons,[54,55] bipolarons,[56] and solitons,[57] which are formed by dopants in conjugated polymers. A polaron comprises an electron/hole and an accompanying lattice distortion or polarization. A bipolaron contains two electrons/holes coupled by an attractive interaction behaving as a single entity. A soliton refers to a solitary wave packet that represents a stable, localized charge carrier that forms due to Peierls distortion (*i.e.*, a spontaneous distortion in neutral conjugated polymer, which leads to the formation of alternating single and double bond lengths and breaks the symmetry of the polymer chain). These quasi-particles are found in materials with strong electron–phonon interactions, like organic semiconductors.

Solid-state heat engines can be created using the above thermoelectric effect to convert thermal energy to electrical energy through the Seebeck effect. In thermoelectric devices/materials, the energy conversion performance is determined by ZT, a nondimensional number quantifying the figure of merit of the system of interest and defined as,

$$ZT = \frac{S^2 \sigma T}{\kappa} \tag{3}$$

where, σ is the electrical conductivity and the product $S^2\sigma$ is known as the power factor. For molecular junctions, the above equation transfers to $ZT = S^2 G_e T/G_{th}$. The power generation efficiency[58] based on Carnot efficiency $\left(\eta_C = \dfrac{\Delta T}{T_h}\right)$ is given by,[59]

$$\eta_P = \eta_C\left[\frac{\sqrt{1+ZT}-1}{\sqrt{1+ZT}+\dfrac{T_c}{T_h}}\right] \tag{4}$$

Optimizing a thermoelectric material requires decreasing the thermal conductivity to make a "phonon" glass and simultaneously increasing the power factor to obtain an "electronic" crystal. From eqn (3), a high-performing thermoelectric material will have high electrical conductivity, high Seebeck coefficient, and low thermal conductivity, which can be demonstrated by semiconducting polymers.[60] Polymers are inherently bad thermal conductors; therefore, research to increase ZT is usually carried out by improving the power factor. Eqn (4) illustrates that power generation efficiency is directly related to Carnot efficiency, which depends on the temperature differential. Due to their lower melting points and susceptibility to photo-induced oxidation and degradation, polymers, unlike inorganic materials, are limited by smaller temperature differences and lower working temperatures for power generation.

The electrical and thermal conductance are partially coupled by Wiedemann–Franz (WF) law[61] through the electronic contribution to thermal transport. For inorganic materials, the WF law is given by,

$$G_{th,e} = L_0 T G_e;\ L_0 = \frac{\pi^2}{3}\left(\frac{k_B}{e}\right)^2 \tag{5}$$

where $G_{th,e}$ is the electron contribution to the thermal conductance and L_0 is the Sommerfield value ($2.44 \times 10^{-8}\ V^2\ K^{-2}$). The ratio between thermal conductance and the product of electrical conductance with temperature is Lorenz number $\left(L = \dfrac{G_{th,e}}{TG_e} = \dfrac{\kappa_e}{\sigma T}\right)$. For organic materials the expectation of having a constant Lorenz number like inorganic materials (Sommerfield value) is invalid and is further discussed in Section 5.8.

In a molecular scale system, the Landauer formulation[62–64] can be used to calculate the contribution to thermal transport from both electrons (Q_{el}) and phonons (Q_{ph}) between a hot (T_h) and cold (T_c) reservoirs,[65]

$$Q_{el} = \frac{1}{\pi\hbar}\int_0^\infty M(E)(E-\mu)\tau_e(E)\left[f_{FD}^0(T_h) - f_{FD}^0(T_c)\right]dE \tag{6}$$

$$Q_{ph} = \frac{1}{2\pi}\int_0^\infty M(\omega)\hbar\omega\tau_p(\omega)\left[f_{BE}^0(T_h) - f_{BE}^0(T_c)\right]d\omega \tag{7}$$

where and $\tau_p(\omega)$ is the frequency-dependent transmission function for phonons, and f_{BE}^0 is the Bose–Einstein distribution. Under ballistic conditions, the transmission probability reaches unity in a system that includes the molecular conductor and reservoirs, indicating a fully open quantum channel.[66] The quantized thermal conductance is expressed as,[67]

$$G_{0,th} = \frac{\pi^2 k_B{}^2 T}{3h} \tag{8}$$

The phononic thermal conductance quantum was first measured in electrically insulating silicon nitride nanostructures with a thermal conductance of $16G_{0,th}$ at temperatures below 0.6 K.[68] The electronic contribution to thermal conductance is quantized for electrical conductors due to quantized electrical transport, measured at both cryogenic (~20 mK)[69] and room temperature (~300 K).[70,71]

2.2 Thermal transport in mesoscopic polymer systems

While the macroscopic thermal transport in polymers can be well approximated using the conventional Fourier law of heat conduction, it encounters limitations when the classical law is applied in systems with spatial heterogeneity in structure and temperature at the scales comparable to the mean free path of basic energy carriers.[72,73] In electrically insulating polymers, thermal properties are dominated by phonon transport and interactions. Thermal conductivity is determined by considering the intricate dynamics of phonon-scattering mechanisms, including phonon–phonon interactions (Umklapp scattering and normal scattering), boundary scattering, and impurity scattering. Researchers often employ kinetic theory that uses a particle analogy to study thermal transport at the mesoscopic or above. It should be noted that the validity of this particle picture diminishes when effects such as interference, diffraction, and tunneling gain significance. In contrast to the Landauer transport theory above, which distinguishes the quantum properties of different energy carriers, the kinetic theory applies a universal approximation that works for all energy carriers. The thermal conductivity (κ) under summation of all phonon modes is expressed as,[74]

$$\kappa = \frac{1}{3} c_{\mathrm{v}} v_{\mathrm{g}} \lambda = \frac{1}{3} c_{\mathrm{v}} {v_{\mathrm{g}}}^2 \tau_{\mathrm{ph}} \tag{9}$$

where c_{v} is the specific heat of each phonon mode, v_{g} is phonon group velocity, λ is the phonon mean free path, and τ_{ph} is the phonon relaxation time. Each variable on the right-hand side of eqn (4) is discussed in the remaining part of the section.

The mean free path of the dominant phonon decreases with temperature, increasing the chance of scattering in an anharmonic lattice.[75] The phonon mean free path for normal processes are given as follows,[76–78]

$$\lambda_{\mathrm{L}} = \frac{Ca}{T}\left(\frac{1}{a\boldsymbol{k}}\right)^4 \tag{10}$$

$$\lambda_{\mathrm{T}} = \frac{Da}{T^4}\left(\frac{1}{a\boldsymbol{k}}\right),\ T''\ \Theta_{\mathrm{D}};\ \ \lambda_{\mathrm{T}} = \frac{D'a}{T}\left(\frac{1}{a\boldsymbol{k}}\right),\ \ T''\Theta_{\mathrm{D}} \tag{11}$$

where a is the lattice constant, $\boldsymbol{k}$ is the wave vector, and C,D,D' are experimental constants. The mean free path of longitudinal modes denoted by subscript 'L' remains unaffected by Debye temperature (Θ_{D}). Conversely, the mean free path of transverse modes, denoted by the subscript 'T', changes with Θ_{D}. Debye temperature reflects the highest frequency of atomic vibrations within a material. At temperatures well below Θ_{D}, the solid behaves like a harmonic system, with vibrations resembling simple harmonic motion. However, as the temperature increases and approaches Θ_{D}, anharmonic effects become more pronounced, leading to deviations from purely harmonic behavior. Typically, higher phonon group velocity corresponds to a higher Θ_{D}. The velocity of phonons notably depends on bond stiffness and the prevailing scattering mechanisms. In the context of a one-dimensional crystalline polymer chain, the phonon velocity is expressed as follows,[79]

$$v_{\mathrm{s}} = \frac{\omega}{|\boldsymbol{k}|} = \sqrt{\frac{2\bar{E}}{\overline{M_{\mathrm{b}}}}} \tag{12}$$

where ω is the frequency, $\bar{E}$ is the average backbone energy, and $\overline{M_{\mathrm{b}}}$ is the average mass of backbone atoms.

The specific heat of phonons is also closely related to Θ_{D}. Under the assumption of a linear dispersion relation, the specific heat for acoustic phonons is given by,[64]

$$C_{\mathrm{v}} = 234\eta_{\mathrm{a}} k_{\mathrm{B}}\left(\frac{T}{\Theta_{\mathrm{D}}}\right)^3,\ \ T \ll \Theta_{\mathrm{D}};\ \ C_{\mathrm{v}} = 3\eta_{\mathrm{a}} k_{\mathrm{B}},\ \ T \gg \Theta_{\mathrm{D}} \tag{13}$$

where η_{a} is the number of unit cells per unit volume. It shows that the specific heat follows a cubic relation at temperatures below Θ_{D} and increases linearly at temperatures above Θ_{D}. The specific heat of electrons employing the free electron theory can be expressed as follows,[80]

$$C_{\mathrm{v,e}} = \frac{\pi^2 {k_{\mathrm{B}}}^2 \eta_{\mathrm{e}}}{2E_{\mathrm{F}}} T \tag{14}$$

where E_{F} is the Fermi energy (chemical potential) and is assumed, in this context, to be substantially greater than $k_{\mathrm{B}}T$. Each polymeric system possesses distinct characteristics. The interplay of intrinsic and extrinsic effects defies straightforward equation formulation, necessitating comprehensive computational approaches.

2.3 Simulation methods

The above theories provide the basic framework for understanding thermal transport and thermoelectric properties in polymers. Quantitative details of typically complex polymer molecular systems require simulation and modeling methods. Here, we will describe three methods for predicting thermal transport and thermoelectric properties in polymers with geometrical and material constraints.

2.3.1 Density functional theory (DFT). The first principle-based DFT method is instrumental in understanding polymers' electronic and vibrational structures. It relies on Hohenberg–Kohn theorems,[81] which states that the ground state properties of a many-electron system can be determined from the electron density alone. DFT calculations yield electronic band structure, density of states, and Fermi surface, which can be used to calculate electrical conductivity and Seebeck coefficient. While DFT is inherently an electron theory, it can be extended to calculate phonon dispersion relations through Density Functional Perturbation Theory[82] (DFPT). After attaining dispersion relation, the anharmonic and harmonic force constants are obtained using Fermi's golden rule.[83] Subsequently, harmonic and anharmonic force constants are derived to estimate the thermal conductivity.[84,85] However, DFT has limitations, particularly in approximating exchange–correlation functionals and handling van der Waal's interactions. It is also limited to small-scale systems as it is computationally intensive, whereas molecular dynamics can be used for larger systems.

2.3.2 Molecular dynamics (MD). MD is an atomic-level technique based on classical mechanics and needs only materials structure and suitable interatomic potentials as input. This gives a significant advantage in simulating multi-scale systems over realistic timescales.[86] It is usually divided into Non-Equilibrium MD (NEMD) and Equilibrium MD (EMD). NEMD is computed according to Fourier's law[87,88] and simulates thermal transport by creating a temperature gradient across the simulation box. NEMD can be particularly useful for studying heat conduction mechanisms and evaluating materials' thermal conductivity. It involves direct simulation of heat flux responses to imposed temperature difference. In contrast to NEMD, EMD does not impose a temperature gradient but rather calculates thermal transport properties from the spontaneous fluctuations in the system at thermal equilibrium and is computed according to Green–Kubo formulism,[89]

$$\kappa_{\alpha\beta} = \frac{V}{k_B T^2}\int_0^\infty \langle J_\alpha(t) J_\beta(0)\rangle \mathrm{d}t \tag{15}$$

where V is the volume of the system, J_α is heat flux in α direction, and the angular brackets indicate the ensemble average. Here, thermal conductivity is computed as a time integral of the heat current autocorrelation function. Both NEMD and EMD have their unique advantages and limitations. NEMD is more straightforward and intuitive for conceptualizing thermal transport processes but may suffer from size and boundary effects. EMD, on the other hand, does not have these limitations but requires longer simulation times and careful statistical analysis.

2.3.3 **Atomistic green function (AGF).** The AGF approach is based on Green's functions, which describe the quantum wave propagation of electrons or phonons in a material. The Green's function encapsulates information about the energy levels and the states of the system. The AGF method uses self-energy matrices to represent the effect of bulk contacts on the device, thus simplifying the complexities of multiscale transport. The transmission coefficient calculation[90] used in the AGF approach for phonon transport follows,[91]

$$\tau(\omega) = \mathrm{trace}[\Gamma_L G^R \Gamma_R G^A] \tag{16}$$

where Γ_L and Γ_R represent the coupling of the material to the left and right heat reservoirs (or leads). G^R and G^A are the retarded and advanced Green's functions, respectively, which describe the phonon states in the material. After calculating the transmission function, the thermal conductance can be estimated from eqn (2). The AGF method is advantageous for modeling phonon transport in nanostructured materials[92] over other methods as it accounts for boundary and interface scattering efficiently and offers great flexibility in handling complicated geometries.

3. Experimental methods for measuring thermal conductivity in nanoscale/microscale systems

The past decade has witnessed remarkable progress in understanding and controlling the thermal properties of polymers at the micro- and nano-scale.[93] Mainly, advances in micro- and nano-engineering have created polymers with metal-like high thermal conductivity,[94] as high as ~100 W m^{-1} K^{-1}. Quantifying the thermal conductivity of polymers demands careful control of experimental variables, notably convection and radiation effects, which may otherwise dominate measurements at small scales. For this reason, experiments are conducted in high vacuum conditions and are shielded from potential radiation heat transfer. Various approaches have been developed to assess thermal conductivity in polymer materials, each with limitations and constraints. They are typically classified into optical and electrical resistive methods, where the former reads surface emission or reflection, and the latter uses a temperature-sensitive resistor to measure the heat flow through the polymer. Below, these methodologies are explored in detail, and their key attributes and comparisons are summarized in Table 1. As reviewing bulk scale methods to measure the thermal conductivity of thermoelectric materials is out of the scope of the article, the readers are referred to comprehensive

Table 1 Comparison of different thermal conductance experimental methods for single molecule and nanoscale systems

Experiment method	Minimum scale (μm)	Advantages	Limitations	Sample type	Ref.
Thermal bridge	0.01	Direct measurement	Contact resistance and complex manipulation to install samples	Fiber	97
SThM	Nano-to-atomic scale	Direct characterization of heterogeneous sample and thermal mapping	Complex microfabrication of scanning thermal probes	Fiber or single chain	70
TDTR	10	Mean free path estimation	Indirect measurement, need transducer coating	Fiber and films	98
Cantilever deflection	0.01	Micro/nano-scale, and one stop method with drawing and measurement	Laser induced deflection on cantilever, indirect measurement	Fiber	98
TTG	0.1	No transducer layer	Sample thickness limitation	Films	99
LFA	30	Non-contact and fast	Need emissive coating, indirect measurement	Fiber and films	100
3ω method	0.1	Direct measurement	Film thickness limitation	Films	101
Steady-state infrared thermography	0.1	Direct measurement and non-contact	Sample emissivity limitation	Films	102

Table 2 Experimental thermal conductivity values for different polymers, limited to microfibers, nanofibers, and thin films

Polymer	Molecular structure	Size (μm)-sample type	Method	κ (W m^{-1} K^{-1})	Fabrication technique	Ref.
PT	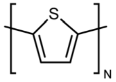	0.071 fiber	Thermal bridge	4.4	Template	109
Zylon	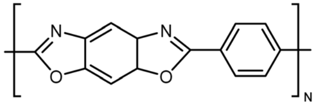	10 fiber	Thermal bridge	60	—	110
		10–30 fiber	TDTR	23	Epoxy block	111
		10–30 fiber	TDTR	19	Epoxy block	111
		16 film	LFA	36.7	Building blocks	112
PE	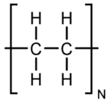	12 fiber	Thermal bridge	50	—	110
		NA fiber	Thermal bridge	90	Transient heat stretch	94
		NA fiber	Thermal bridge	100	Gel drawing	98
		NA fiber	Thermal bridge	8	Electro spinning	113
		NA film	TTG	40	Rolling and stretching	114
		0.1 fiber array	LFA	20	Nano porous template	100
		4 tape	Pulsed photothermal	30	Tensile drawing	115
		6 single crystal	Pulsed photothermal	40	Tensile drawing	115
		Mat	LFA	18.4	Hot rolling	116
		30 tape/film	Thermal bridge	1.8	Electrospinning	117
		Fiber	Steady state system	62	Extrude and roll–roll	118
		150 film	LFA	38	Gel spun	119
		NA fiber	Hot disk	10.7	Solution gel sheared	120
		NA film	Photoacoustic	7	Nanofibrous template	121
		0.2 fiber	Photoacoustic	3	Nanofibrous template	121
		0.2 fiber	TDTR	17	Epoxy block	111
		10–30 fiber	TDTR	12	Epoxy block	111
			TDTR	15	Epoxy block	111
Polysilsesquioxane-C6	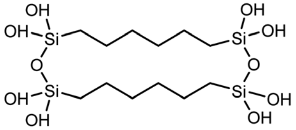	2 rod	Thermal bridge	0.4	Synthesis	122
Polysilsesquioxane-C8	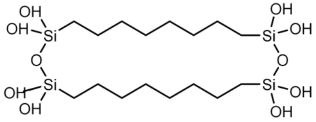	2 rod	Thermal bridge	0.5	Synthesis	122
Kevlar	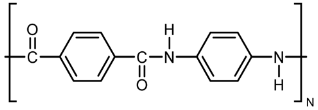	10–30 fiber	TDTR	3.5	Epoxy block	122

Table 2 (*Contd.*)

Polymer	Molecular structure	Size (μm)-sample type	Method	κ (W m^{-1} K^{-1})	Fabrication technique	Ref.
Vectra	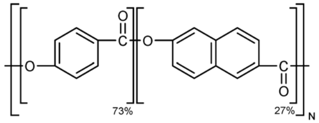	10–30 fiber	TDTR	1.75	Epoxy block	122
M5AS	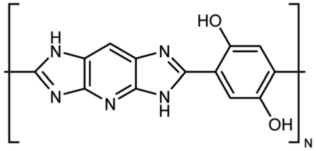	10–30 fiber	TDTR	9	Epoxy block	122
PBT	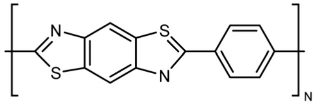	10–30 fiber	TDTR	12	Epoxy block	122
PI	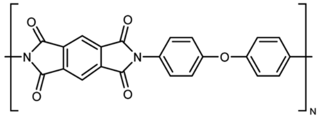	0.037 fiber 23 fiber 2.25 film 15 mat/film	Thermal bridge Transient electro 3-Omega Thermal bridge	3 2 0.1–1 1	Electrospinning Spinning and hot draw — Electro spinning and hot pressing	123 124 125 126
Azo-benzene	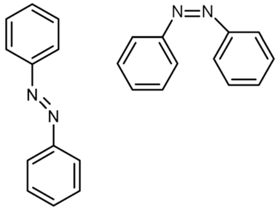	0.28 film	TDTR	*Trans*: 0.35 *Cis*: 0.1	Spin coating	42
PAC	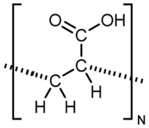	10 film	3-Omega	1.2	Spin coating	127
P3HT	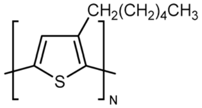	0.16 film 0.1 fiber	TDTR Photoacoustic	2.2 7	oCVD Nanofibrous template	128 121

Table 2 (*Contd.*)

Polymer	Molecular structure	Size (μm)-sample type	Method	κ (W m^{-1} K^{-1})	Fabrication technique	Ref.
Nylon-11	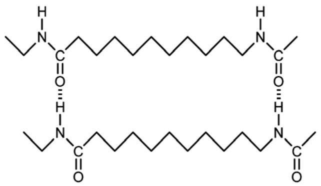	0.07 fiber	Thermal bridge	1.6	Electrospinning	129
Poly(3-methylthiophene)	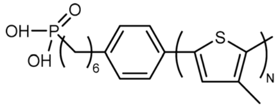	0.04 film	TDTR	2	Surface-initiated polymerization	130
PS	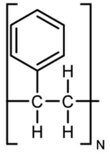	0.12 fiber	Cantilever deflection	14.4	Electrospinning	131
PVDF	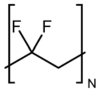	0.072 fiber	Thermal bridge	0.9	Electrospinning	117
PVA	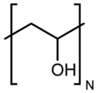	0.061 fiber	Thermal bridge	1.7	Electrospinning	117
PVC	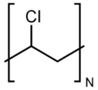	0.054 fiber	Thermal bridge	0.5	Electrospinning	117
Cellulose	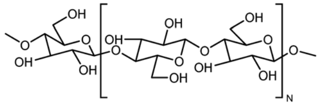	6 fiber	Thermal bridge	14.5	Hydrodynamic focusing	132

reviews.[95,96] Experimental thermal conductivity values for different polymers, limited to microfibers, nanofibers, and thin films, are tabulated in Table 2.

3.1 Thermal bridge

This method employs one or two suspended islands, each less than 100 μm in size, that are embedded with a calorimeter to record temperature changes on the islands. The suspension of the islands ensures high thermal resistance relative to the surrounding heat sink, thereby enhancing the calorimeter's sensitivity to detect small heat fluxes.[97] A micro/nanoscale polymer fiber or film bridges the two islands maintained at different temperatures (ΔT). This temperature difference drives a heat flow (q) from the hot to the cold side through the polymer, measurable *via* a small temperature change on the island (Fig. 1(b)(ii)). Subsequently, the thermal conductance of the polymer is determined by $G_{\text{th}} = q/\Delta T$, which is then used to calculate the thermal conductivity based on the measured geometry dimensions of the polymer material.

3.2 Bi-material cantilever

This technique utilizes a cantilever like those used in laser-based atomic force microscopy (AFM). However, it is constructed from two distinct materials, each with a different coefficient of thermal expansion (CTE). This bi-material cantilever, characterized by its low stiffness, exhibits deflection when the temperature on the cantilever changes due to the differential expansion rates of the materials.[103,104] In an experiment, a polymer fiber is placed between the terminal point of the cantilever and a hot thermal reservoir, as illustrated in Fig. 1(b)(ii). The heat flowing to the cantilever through the fiber causes a temperature-induced deflection, which is quantitatively measured using a laser and a photodetector in AFM. This deflection is converted into a temperature increase on the cantilever through calibration measurements. Like the thermal bridge technique, this temperature increase can be converted into the thermal conductivity of the polymer fiber using Fourier's law. Shen *et al.*[98] have employed the bi-material cantilever method to measure the thermal conductivity of polyethylene

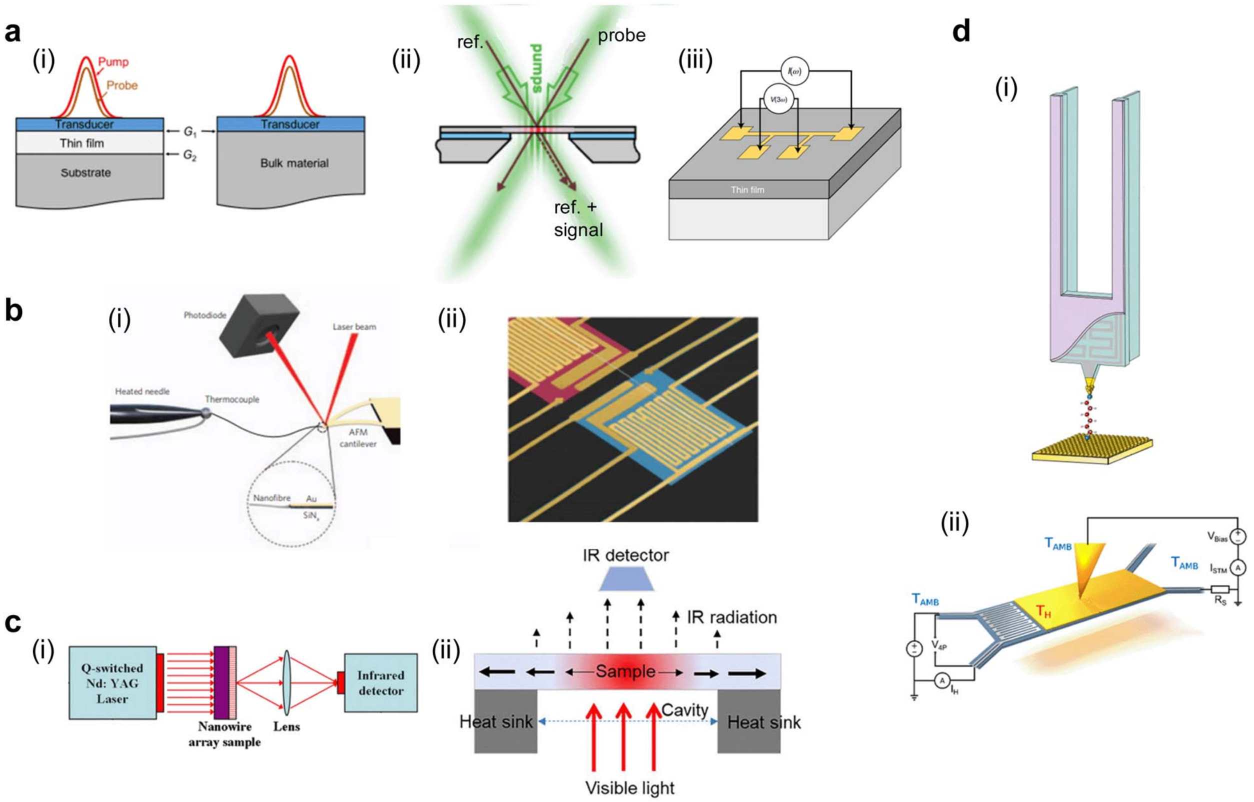

Fig. 1 Schematic of different experimental methods for thermal conductance measurements (a) Thin film measurement methods: (i) Time Domain Thermal Reflectance (TDTR). Reproduced with permission.[42] Copyright, 2018, American Institute of Physics – JAP. (ii) Transient Thermal Grating (TTG). Reproduced with permission.[99] Copyright, 2013, American Physical Society – PRL. (iii) 3-Omega method. Reproduced with permission.[105] Copyright, 2021, *Nature Materials*. (b) Microfiber and nanofiber measurement methods: (i) bi-material cantilever. Reproduced with permission[98] Copyright, 2010, *Nature Nanotechnology*. (ii) Thermal bridge. Reproduced with permission.[106] Copyright, 2019, *Science Advances*. (c) Bulk scale measurements: (i) Laser Flash Analysis (LFA). Reproduced with permission[100] Copyright, 2011, *Polymer*. (ii) Steady-state-infrared-thermography. Reproduced with permission[102] Copyright, 2017, American Institute of Physics – RSI. (d) Nanofiber and molecular level measurement methods: (i) Scanning Thermal Microscopy (SThM) with a resistor on a probe. Reproduced with permission[27] Copyright, 2019, *Nature*. (ii) Scanning Thermal Microscopy (SThM) with a resistor on the sample. Reproduced with permission[71] Copyright, 2017, *Nature Nanotechnology*.

nanofibers, thus validating its applicability for assessing the thermal characteristics of polymeric materials.

3.3 Time domain thermal reflectance (TDTR)

TDTR is a non-contact, optical method used to measure the thermal properties of thin materials,[42] particularly thermal diffusivity and thermal conductivity. It uses a dual-laser system consisting of a pump laser and a probe laser (Fig. 1(a)(i)) spit from the same laser source but with slightly different arrival times to the sample surface. The pump laser heats the sample periodically, while the probe laser measures the resulting change in the sample's reflectance due to this heating.[107] To overcome the low reflectivity of polymers and enhance the accuracy of measurements, the sample is coated with a transducer film, typically made of aluminum, known for its temperature-dependent reflectance properties. The probe laser's reflection is measured at a high frequency (femtosecond to picosecond scales), capturing how the sample's temperature changes in response to the pump laser heating. This time-resolved measurement allows for calculating the sample's thermal properties by analyzing the heat flow away from the surface over time. This analysis involves fitting the data to a thermal model that accounts for the sample's interfacial contact thermal resistance from the multi-layer structure.

3.4 Laser flash analysis (LFA)

LFA operates on the principle of transient heat propagation through a material sample.[108] In this method, a brief laser pulse is applied to the center or the extreme end of the sample, initiating a heat wave that traverses the material (Fig. 1(c)(i)). The time elapsed for the heat wave to reach the ends of the sample is recorded. Using a heat diffusion equation, this temporal data is subsequently employed to calculate the material's thermal conductivity. An added layer of complexity can be introduced by subjecting the sample to varying temperatures in a furnace; this allows for examining the temperature dependence of the material's thermal conductivity.

3.5 Three-omega method (3ω)

The 3ω method[101] utilizes a thin metallic strip, often made of platinum or another metal, which simultaneously acts as a heater and a resistive temperature sensor (Fig. 1(a)(iii)). This strip is deposited on the material's surface, whose thermal conductivity will be measured. An alternating current (I_ω) with angular frequency ω passes through the metallic strip, inducing Joule heating and creating a temperature oscillation in the material at 2ω with an amplitude of $\Delta T_{2\omega}$. This oscillation changes the metallic strip's resistance according to its temperature coefficient of resistance (α) at 2ω. Due to the nonlinear relationship between temperature and resistance, a third harmonic (3ω) component is generated in the voltage across the strip, $V_{3\omega} = \Delta T_{2\omega}\alpha I_\omega R/2$. Upon measuring $V_{3\omega}$, $\Delta T_{2\omega}$ can be calculated, which then allows for the estimation of the thermal conductance of the material beneath the metallic strip by establishing a linear relationship between $\Delta T_{2\omega}$ and the input power. Calibration measurements conducted without the polymer material allow for the estimation of the cross-plane thermal conductance of the polymer.

The 3ω method circumvents the limitations inherent to direct current (DC) techniques, particularly the radiative heat loss from the sample, which often leads to imprecise or skewed measurements.[105] A high-frequency operation intrinsic to the 3ω method effectively minimizes heat loss attributed to radiation. Operating in an alternating current (AC) regime significantly reduces shot noise and other instrumental noises compared to DC methods. This noise reduction enables the reliable measurement of materials with extremely low thermal conductivity, making the 3ω method especially valuable for accurately characterizing materials that are challenging to assess using DC techniques.

3.6 Steady-state infrared thermography

This method employs a setup incorporating a thin film placed over a hole in an opaque substrate. The role of the substrate is dual: it functions as a heat sink for thermal dissipation and, owing to its opacity, prevents light from reaching the peripheral edges of the thin film. Illumination is provided from below by visible light, which raises the temperature of the film (Fig. 1(c)(ii)). The heat generated in the film is conducted away through the substrate and the hole, thus establishing a steady-state temperature gradient across the film.[102] The feature of this technique is the utilization of an infrared detector to capture the temperature distribution across the film. The recorded data is then fitted to a theoretical temperature distribution model specific to the hole's geometry. Through this fit, the in-plane thermal conductivity of the thin film is ascertained.

3.7 Transient thermal grating (TTG)

TTG evaluates thermal conductivity utilizing the constructive interference of two crossed laser beams to generate a sinusoidal thermal grating on the sample's surface. Another probe laser beam is then incident on this thermal grating and undergoes diffraction. The diffracted light pattern is then analyzed to deduce the thermal conductivity of the material[99] (Fig. 1(a)(ii)). One of the distinguishing attributes of TTG is its high sensitivity to in-plane thermal conductivity, negating the need for transducer deposition on the sample surface like TDTR. Moreover, the method offers insight into the material's phonon mean free paths (MFP). Specifically, when the heater's dimensions—the laser beam diameter, thermal penetration depth, or grating spacing—are on the same order of magnitude as the MFPs of the phonons. The measured thermal conductivity is observed to be reduced due to the enhanced phonon scattering that occurs even in the absence of physical boundaries. This property has been leveraged to derive the accumulative thermal conductivity over the mean free path spectrum. By doing so, TTG allows for the spectral probing of non-diffusive phonon transport phenomena, thereby facilitating the validation of first-principles and nanoscale simulations of thermal transport properties.[114]

3.8 Scanning thermal microscopy (SThM)

SThM[133] is a scanning probe-based technique for measuring the thermal conductance of materials with ultrahigh spatial resolution, down the level of single atoms and molecules. Central to the technique is a thermal probe fabricated using state-of-the-art nanofabrication methods (Fig. 1(d)). This thermal probe is integrated into a scanning tunneling microscope (STM)[70,71] or AFM.[134] The integration allows for a non-thermal signal feedback mechanism, enhancing the method's versatility and applicability. A scanning thermal probe can be nanofabricated using MEMS techniques and then be used to scan the surface of a material to obtain its temperature profile with nanometer scale features.[135,136] Other thermophysical properties obtained using SThM include thermal conductivity, thermal expansion coefficient, thermal contact resistance, and heat capacity. In conjunction with electrical or even magnetic field measurements, SThM can create multi-modal scanning probe platforms to evaluate dissipation and energy conversion properties in various materials. Specifically for molecular chain measurement, an STM beak junction (STMBJ) technique is developed,[137] creating a bonded molecular junction between the scanning probe tip and the sample. The probe is retracted until the junction breaks, and a thermal signal change before and after the junction's breaking indicates the individual molecule's thermal conductance. The STMBJ technique is particularly useful for studies focused on fundamental phonon and charge transport in molecular systems, and it offers the precision required to validate quantum-level thermal and thermoelectrical transport theories and simulations.

4. Thermoelectricity in semiconducting polymers

Intrinsically synthesized polymers become electrically semiconductive only when they possess conjugated chemical backbones and delocalized π-electrons.[138] Further, most polymers have a wide bandgap, and their electrical transport properties must be tuned *via* doping, ionic polymerization, and chain alignment to create organic semiconductors (OSCs).[139] These techniques also correspondingly affect the thermal transport in polymers, which for semiconducting polymers are attributed to more complicated charge and phonon transport effects than the thermal transport characteristics in phonon-dominated polymers. This section discusses creating OSCs through doping and then delves into optimizing doping concentration through de-doping methods. Synthesis methods like blending polymers, non-solution-based polymerization techniques, and chain alignment are discussed. The later part of the section discussed molecular engineering methods to modify the backbone, side chain, molecular weight, crystallinity, and morphology.

4.1 Doping

Doping allows the electrons in the polymer's π-bonds to move around the polymer chain, increasing their transport mobility (μ). It also introduces geometric distortion,[57] which creates non-neutral polarons, bipolarons, and solitons as charge carriers. Doping enhances coulombic interactions and the coupling of polarons in transition states. Such interactions can alter the material's local state and shift energy levels. Consequently, these changes can significantly enhance the thermoelectric

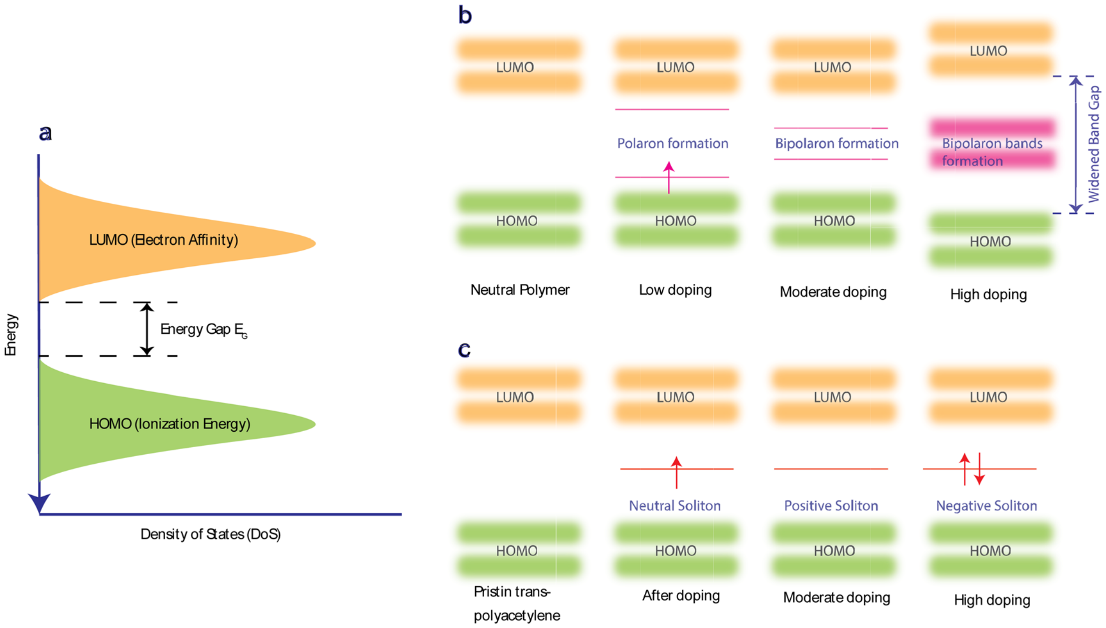

Fig. 2 Charge transport in organic semiconductors (OSCs). (a) Lowest unoccupied molecular orbitals give the electronic energy levels of OSC – LUMO (approximated electron affinity) and highest occupied molecular orbital – HOMO (approximated ionization energy). (b) A band structure schematic showing the formation of polarons, bipolarons, and bipolaron bands as a function of doping level. (c) A band structure schematic of *trans*-polyacetylene showing a neutral soliton, positive soliton, and negative soliton.

properties of the material. Doping can be n-type (reduction) or p-type (oxidation).

The selection of dopant is dependent on the HOMO (highest occupied molecular orbital) and LUMO (lowest unoccupied molecular orbital) energy levels of the conjugated polymer (Fig. 2(a)). A polymer with a high HOMO level will more readily give up electrons and become oxidized. Hence, p-dopants are used to accept electrons and form positive polarons. In n-doping, the polymers with lower LUMO levels are used as they can more readily accept electrons and form negative polarons.[9] Fig. 2(b) illustrates how polaron, bipolaron, and bipolaron bands develop relative to the doping level in various OSCs. Initially, at low doping levels, polarons with spin-1/2 are generated. As doping increases, these polarons combine to form spinless bipolarons.

Further doping causes these bipolaron levels to overlap, eventually leading to the formation of continuous bands.[138,140] The band gap between the conduction and valence bands widens as states at the edges of these bands evolve to form the bipolaron bands/states. However, at very high doping levels in many OSCs, the upper and lower bipolaron bands converge with the conduction and valence bands, resulting in partially filled bands akin to those in metals. If the two charges comprising a bipolaron are loosely bound and can easily separate due to the degenerate state of the OSC. The energy between these two charges on either side of them is identical, causing them to behave like a solitary wave that propagates without distortion or energy loss.[141] Precisely, in pristine *trans*-PAc, a soliton is termed neutral if an odd number of conjugated carbons leads to an unpaired electron. Adding another unpaired electron transforms it into a negatively charged soliton, while its removal results in a positive soliton. This process generates new localized states within the middle of the energy gap (Fig. 2(c)), which are half-filled in the case of a neutral soliton and either empty or fully filled for a positive or negative soliton, respectively. As doping levels rise, these charged solitons interact, forming a soliton band. This band can eventually merge with the edges of the valence/conduction band, leading to metallic conductivity.[142]

Doping can be achieved by two primary methods:[143] acid–base doping, which is by introducing a cation or anion to the polymer backbone, and charge neutrality is preserved through the accompaniment of a counterion (Fig. 3). The other method is redox doping, which entails the transfer of electrons, forming a donor–acceptor charge-transfer complex or ion pair. The proton (H^+) is added to the polymer backbone in acid doping, like polyaniline with camphor sulfonic acid (CSA)[144] or with hydrochloric acid (HCl) and acetic acid,[145] polythiophenes with ethylbenzene sulfonic acid (EBSA).[146] The hydride (H^-) is added to the polymer backbone in base doping, like napthalenedicarboximide-bithiophene copolymer P(NDIOD-T2)[147] and benzodifurandione-based poly(*p*-phenylene vinylene) derivatives (BDPPV)[148] with benzimidazole derivatives. Redox doping needs a slight offset in HOMO and LUMO levels, as discussed previously, to form polarons. The HOMO and LUMO levels are sensitive to the conditions of polymer synthesis, but the energy levels for dopants are constant. A widely studied p-type conjugated polymer is poly(3,4-ethylenedioxythiophene) (PEDOT)[149] as it can allow readily solution processing. Further, p-type polymers are preferred to n-type polymers as they are more oxidation resistant and chemically stable.[150]

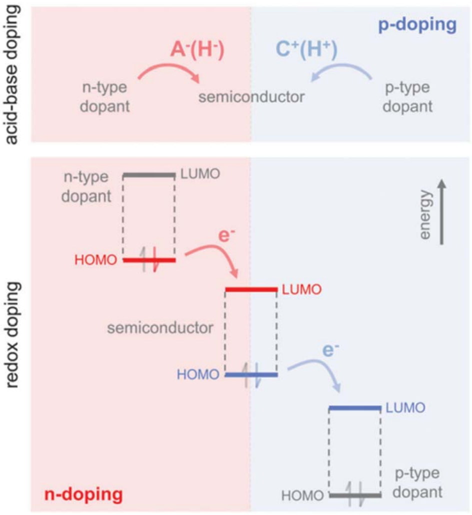

Fig. 3 Mechanisms for n-type and p-type doping: the top panel is acid–base doping showing anion (H^-) or cation (H^+) addition to the polymer backbone. The bottom panel is redox doping, showing the transfer of electrons to the LUMO level or the transfer of electrons from the HOMO level of the polymer. Reproduced with permission.[143] Copyright, 2017, Wiley – *Advanced Materials*.

The homogeneity[151] and concentration of the dopant[152] are two critical factors influencing the thermoelectric properties of OSCs. An increase in dopant concentration increases the charge carrier's density, increasing electrical conductivity but decreasing the Seebeck coefficient (Fig. 4(a)). Glaudell *et al.*[153] found an empirical relationship between the Seebeck Coefficient and electrical conductivity for different doping concentrations from several experimental studies of polythiophenes as $S \propto \sigma^{-\frac{1}{4}}$. Controlling doping concentration to get the highest power factor during doping has been proven difficult owing to the long chain length of the dopant.[154] Several methods have been developed to optimize and get the maximum power factor at a desired dopant concentration (as described below). However, it should be noted that most of these studies measured electrical conductivity and not the Seebeck coefficient, and rarely, thermal conductivity gives an incomplete picture of *ZT* of thermoelectric material.

4.2 De-doping

A viable approach for controlling dopant concentration to reach a high power factor is initially doping the polymers and then proceeding with de-doping.[155] Several techniques for de-doping are summarized below, including chemical reduction de-doping, solvent de-doping, electrochemical de-doping,[156] and acid–base de-doping.

4.2.1 Chemical reduction de-doping. The mechanism for doping a p-type conjugated polymer like PEDOT with tosylate (Tos) ions is[157]

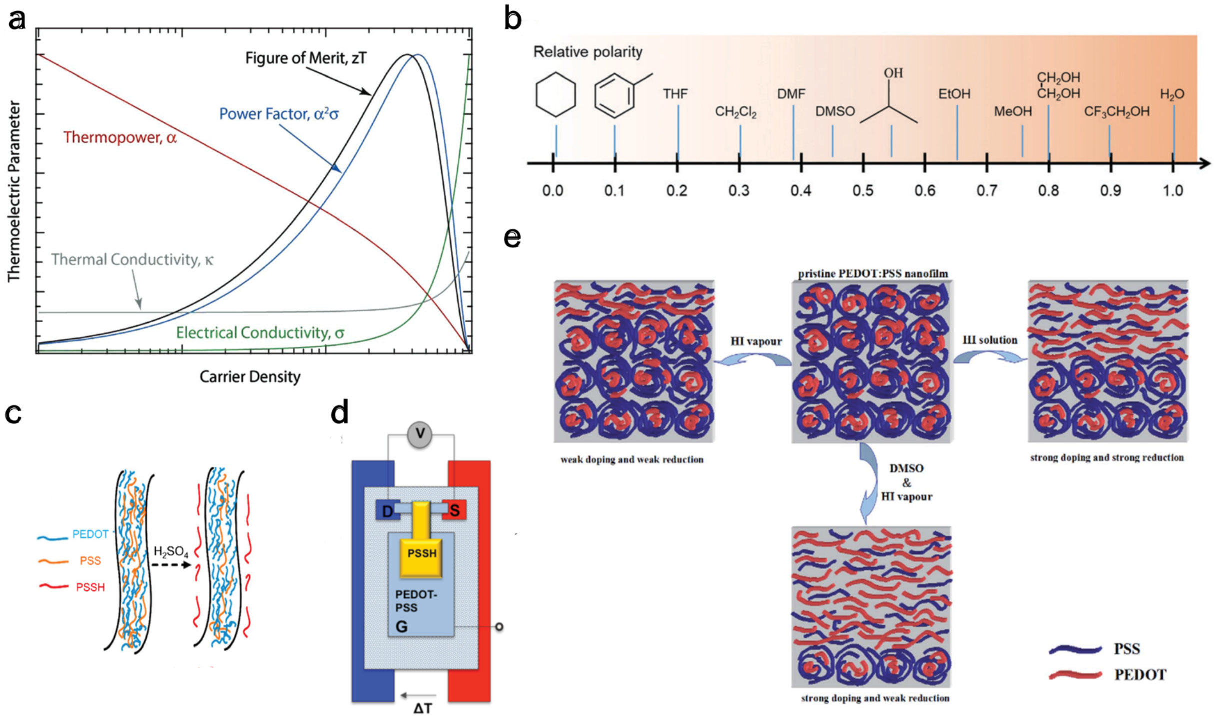

Fig. 4 De-doping mechanisms (a) schematic showing carrier density dependence for different thermoelectric properties, including electrical conductivity and thermopower. Reproduced with permission.[160] Copyright, 2018, Wiley – *Advanced Materials*. (b) Typical solvents used for solvent de-doping and their relative polarity to water. Reproduced with permission.[161] Copyright, 2022, Royal Society Chemistry – CSR. (c) Schematic illustration showing the removal of PSS from PEDOT:PSS polymer using sulfuric acid to reduce the oxidation level. Reproduced with permission.[162] Copyright, 2020, *Nano Energy*. (d) Schematic of the thermoelectric characterization electrochemical setup with PEDOT:PSS between source (S) and drain (D) in a three-terminal organic electrochemical transistor. Reproduced with permission.[163] Copyright, 2012, American Chemical Society – JACS. (e) Schematic of PEDOT:PSS at the top center of the panel, undergoing only vapor chemical reduction de-doping to the left, undergoing only solvent de-doping to the right, and combined vapor chemical reduction de-doping with solvent de-doping at the bottom.[164] Copyright, 2015, Royal Society of Chemistry – *Advances*.

$$\text{EDOT} + \text{Fe}^{3+}(\text{ToS}^-)_3 \rightarrow \text{EDOT}^{\bullet+}\text{Tos}^- + \text{Fe}^{2+}(\text{Tos}^-)_2$$

The oxidized polymer is then reduced with tetrakis(dimethylamino)ethylene (TDAE – an n-type dopant) to control the oxidation level. Bubnova *et al.*[158] noted a consistent rise in electrical conductivity and a falling Seebeck coefficient with increased oxidation level, as illustrated in Fig. 5(a). At the optimized oxidation level of 22%, a *ZT* of 0.25 was measured at room temperature. Massonnet *et al.*[159] oxidized PEDOT with poly(styrene sulphonate) (PSS) and reduced with several agents: sodium sulfite (Na_2SO_3), sodium borohydride ($NaBH_4$), sodium thiosulfate ($Na_2S_2O_3$), hydrazine monohydrate ($NH_2NH_2 \cdot H_2O$), and TDAE. The researchers discovered that employing TDAE (tetrakis(dimethylamino)ethylene) and hydrazine monohydrate as reducing agents resulted in significantly higher Seebeck coefficients of 150 μV K^{-1}, which is about three times higher than those achieved with other reducing agents. This increase in performance is attributed to the formation of neutral chains from di-cation chains observed in PEDOT:PSS, whereas the sulfates create radical cation chains from di-cation chains, showing their weak strength as a reducing agent. This finding highlights the importance of selecting appropriate reducing agents to enhance the thermoelectric properties of conducting conjugated polymers.

4.2.2 Solvent de-doping.

When a dopant is hydrophilic like PSS, and the conjugate polymer is hydrophobic like PEDOT, the doped polymer can be exposed to a polar solvent to dissolve/remove the dopant and control the concentration. Using this method, Kim *et al.*[165] oxidized PEDOT with PSS and used ethylene glycol (EG) as the polar solvent. They obtained a *ZT* of 0.42 after a 100 minutes EG treatment (Fig. 5(b)), the highest observed in the literature. They also found that thermal conductivity diminished from 0.32 W m^{-1} K^{-1} to 0.23 W m^{-1} K^{-1} following EG treatment. The thermal conductivity reduction was attributed to the loss of PSS, a molecule significantly larger than PEDOT, which impacts the covalent contribution. One major limitation of solution de-doping is accurately controlling the process.[166] Moreover, accurately determining the oxidation level is complex, and the choices of counterions are limited.[167] To overcome these limitations, Zhang *et al.*[164] combined solvent de-doping and chemical reduction de-doping to achieve better results than the individual methods (Fig. 4(e)). They used PEDOT:PSS with dimethyl sulfoxide (DMSO) as a solvent and hydrogen iodide (HI) vapor as a chemical reducing agent.

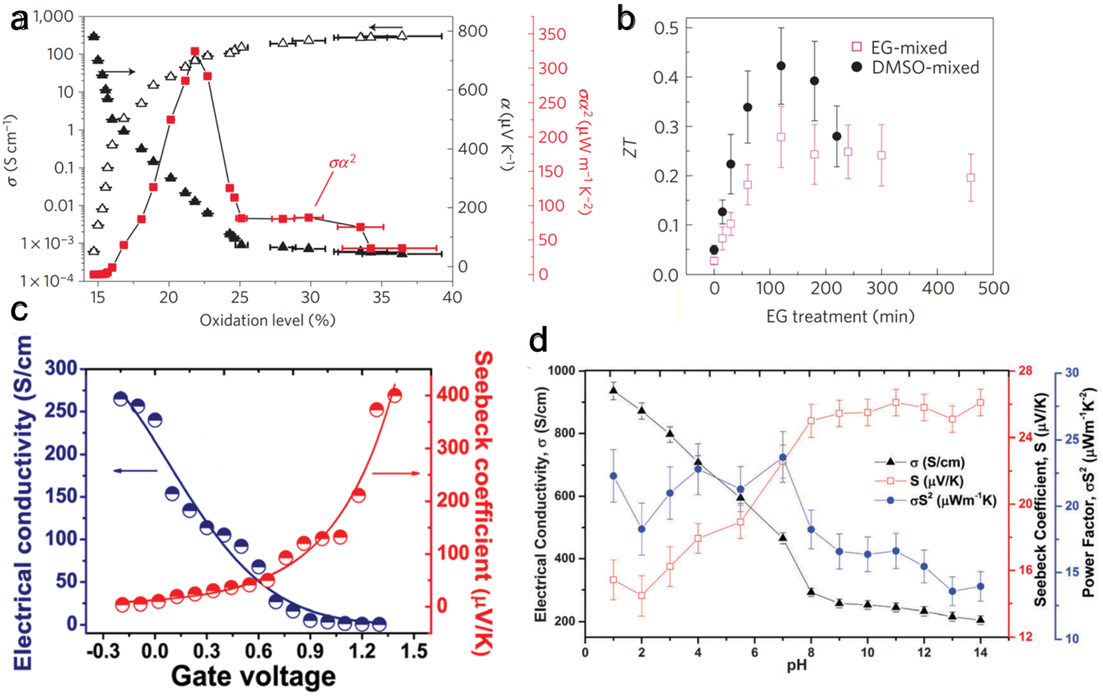

Fig. 5 Effect on thermoelectric properties from different de-doping methods. (a) Chemical reduction de-doping, showing Seebeck coefficient (α), electrical conductivity (σ), and Power factor ($\alpha^2\sigma$) change with varying oxidation levels for PEDOT:Tos. Reproduced with permission.[157] Copyright, 2011, *Nature Materials*. (b) Solvent de-doping, thermoelectric figure of merit (*ZT*) *versus* solvent (EG) treatment time for EG-mixed and DMSO-mixed PEDOT:PSS. Reproduced with permission.[165] Copyright, 2013, *Nature Materials*. (c) Electrochemical de-doping, electrical conductivity, and Seebeck coefficient for varying gate voltage with a peak at 0.8 V. Reproduced with permission.[163] Copyright, 2012, American Chemical Society – JACS. (d) Acid–base de-doping, showing Seebeck coefficient (S), electrical conductivity (σ), and Power factor ($S^2\sigma$) for varying pH level for PEDOT:ToS films. Reproduced with permission.[170] Copyright, 2015, Royal Society of Chemistry – JMCC.

4.2.3 Electrochemical de-doping. This technique offers enhanced control over the oxidation level by adjusting the electrode potential and monitoring the charging current.[168] Bubnova *et al.*[163] employed this method using an organic electrochemical transistor (OECT) composed of PEDOT:PSS, and constructed an electrochemical cell as depicted in Fig. 4(d). Once a positive gate voltage is applied, the gate and channel are gradually oxidized and reduced. The equation below shows electrochemical half-life reactions, one at the channel and the other at the gate,

$$\text{PEDOT}^+\text{PSS}^- + \text{M}^+ + \text{e}^- \rightleftarrows \text{PEDOT}^0 + \text{M}^+\text{PSS}^-$$

Under a gate voltage of 0.8 V (corresponding to a 14.5% oxidation level), the maximum power factor is observed (Fig. 5(c)), with a *ZT* of 0.041. Controlling the oxidation level allows for dynamically altering the material's thermoelectric properties through gate voltage adjustments—similarly, Park *et al.*[169] reported a significantly higher power factor (1270 μW m^{-1} K^{-2}) using PP:PEDOT at a gate voltage of 0.1 V.

4.2.4 Acid–base de-doping. The power factor of an OSC can be enhanced by controlling the pH of the polymer, as changing pH leads to a change in oxidation level. PEDOT:PSS with sulfuric acid (H_2SO_4)[162] is depicted in Fig. 4(c) and follows the reaction

$$\text{PSS}^- + \text{H}_2\text{SO}_4 \rightarrow \text{PSSH} + \text{HSO}_4^-$$

Khan *et al.*[170] used HCl and sodium hydroxide (NaOH) to tune the pH of PEDOT:ToS and found the highest power factor to be at a pH of 7 (Fig. 5(d)). Surface characterization methods showed that the Cl^- and OH^- anions replaced ToS ions. An exciting benefit of acid–base de-doping is that it can provide dynamic control of the thermoelectrical properties of the polymer by simply changing the pH of the environment.

4.3 Blending

Doping and de-doping discussed above showed that increasing dopant concentration decreases the Seebeck coefficient and electrical conductivity increases. Contrarily, to improve both the Seebeck coefficient and electrical conductivity with dopant concentration, the density of states (DOS) of the blended polymers needs to be matched, which was first achieved by Sun *et al.*[171] is done by blending P3HT and poly(3-hexylthiothiophene) (P3HTT) and doping it with F_4TCNQ. A blend of P3HT:P3HTT = 0.8 : 0.2 can increase the Seebeck coefficient and electrical conductivity until 1% of F_4TCNQ (wt%), as depicted in Fig. 6(a). Here, the HOMO level of P3HT is −5.2 eV, the HOMO level of P3HTT is −5.05 eV, and the LUMO level of F_4TCNQ is −5.24 eV. The P3HTT energy level is slightly below the energy level of P3HT, so P3HTT defines the Fermi

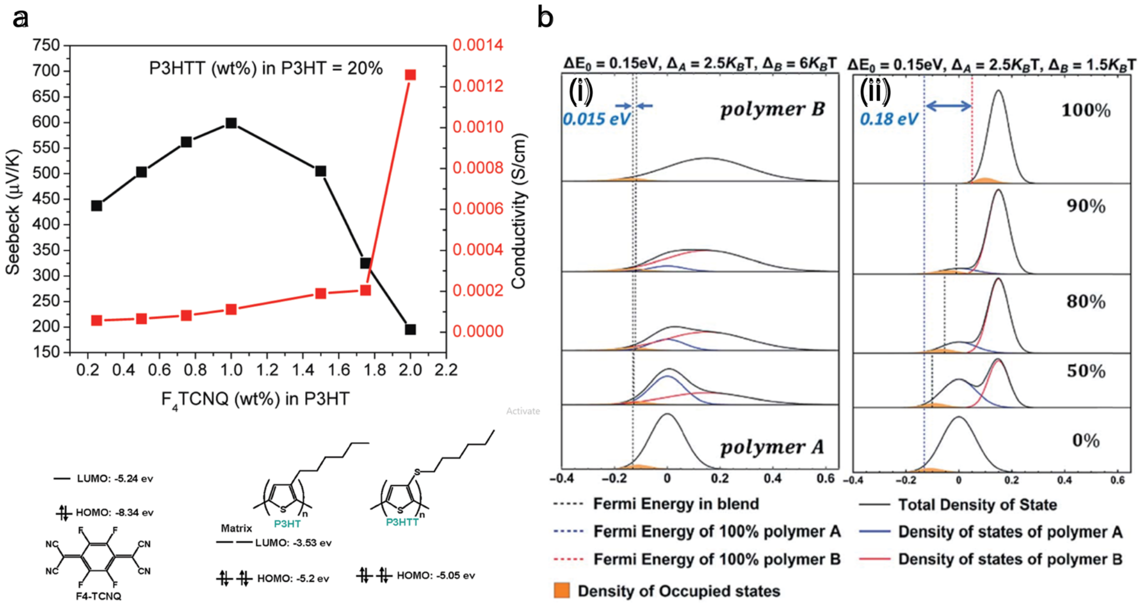

Fig. 6 Improving the thermoelectric performance of conjugated polymer by density of states (DOS) matching through blending. (a) Molecular structures and orbital energies of P3HT, P3HTT, and F_4-TCNQ are shown. It also shows the Seebeck coefficient and electrical conductivity for a blend of P3HTT and P3HT (0.2 : 0.8 wt%). Reproduced with permission.[171] Copyright, 2010, American Chemical Society – *Macromolecules*. (b) DOS of polymer blends with varying composition; (i) the polymer with its DOS centered at higher energies has a broader DOS than the polymer with its DOS centered at lower energies, (ii) the polymer with the higher energy DOS has a narrower DOS. Reproduced with permission.[172] Copyright, 2019, Royal Society of Chemistry – JMCA.

level, while the electrons predominantly traveled in the higher energy orbitals of P3HT. The equilibrated hole carriers in P3HTT chains need to be promoted into higher energy states of P3HT for efficient transport.

The technique of DOS matching[172] is depicted in Fig. 6(b), showing the variation in Fermi energy level as the composition of the polymer blend changes. The left panel is when the width of the DOS is broad ($6k_BT$), and the right panel is when it is narrow ($1.5k_BT$), against a consistent energy offset of 0.15 eV. It is observed that with a broad DOS for polymer B, the Fermi energy exhibits negligible alteration with an increasing concentration of polymer B. In contrast, with a narrow DOS for polymer B, there is a more substantial change (0.18 eV) in the Fermi level as the blend composition changes. Considering the relative position of the Fermi level to the DOS in these scenarios, a broad DOS results in a relatively even distribution of charge carriers between the two polymers.

Conversely, with a narrow DOS, most charge carriers will likely remain on polymer A, leading to its predominance in charge transport until polymer B is present in high concentrations. Intuitively, when charge transport is dominated by one polymer, it's improbable that the power factor in the blends will surpass that of the individual polymers. Therefore, it's anticipated that the most favorable scenario for an enhanced power factor in the blends would be where the Fermi energy shifts gradually and charge carriers are distributed across both polymers. Other studies[172–175] also showed a factor of two enhancement in thermoelectric power factor with different blends.

4.4 Polymerization

When ions are added to monomers during synthesis, interlinked polymerization can occur, potentially increasing the electrical conductivity beyond the original conjugated polymer. Two primary methods for polymerization are electrochemical polymerization and oxidative polymerization. Following the former method, Hirashi *et al.*[176] synthesized doped polythiophene films using nitrobenzene as a solvent and tetra-*n*-butylammonium perchlorate ($TBAClO_4$) as an electrolyte. The polymerization of thiophene, induced by anodic oxidation on indium tin oxide (ITO) electrodes, was carried out in an electrolyte bath containing $TBAClO_4$, thiophene, and nitrobenzene under a nitrogen atmosphere. They observed high Seebeck coefficients and electrical conductivity for 0.1 M thiophene and noted no significant change in these values with varying concentrations of $TBAClO_4$, as depicted in Fig. 7(a).

Similarly, Culebras *et al.*[177] studied PEDOT electropolymerization with several counter-ions, ClO_4, PF_6, and bis(trifluoromethyl sulfonyl)imide (BTFMSI), and observed a relatively high *ZT* value of 0.23 for PEDOT:BTFMSI. This shows another viable approach to achieving high *ZT* values compared to de-doping.

In contrast to electrochemical polymerization, oxidative polymerization[180] involves the oxidation of monomers, forming polymers with extended π-conjugation, crucial for their conducting properties. This process forms the polymer backbone and introduces positive charges (holes) along the chain, enhancing the material's conductivity. Common oxidants include iron(III) chloride ($FeCl_3$) for pyrrole and persulfate for

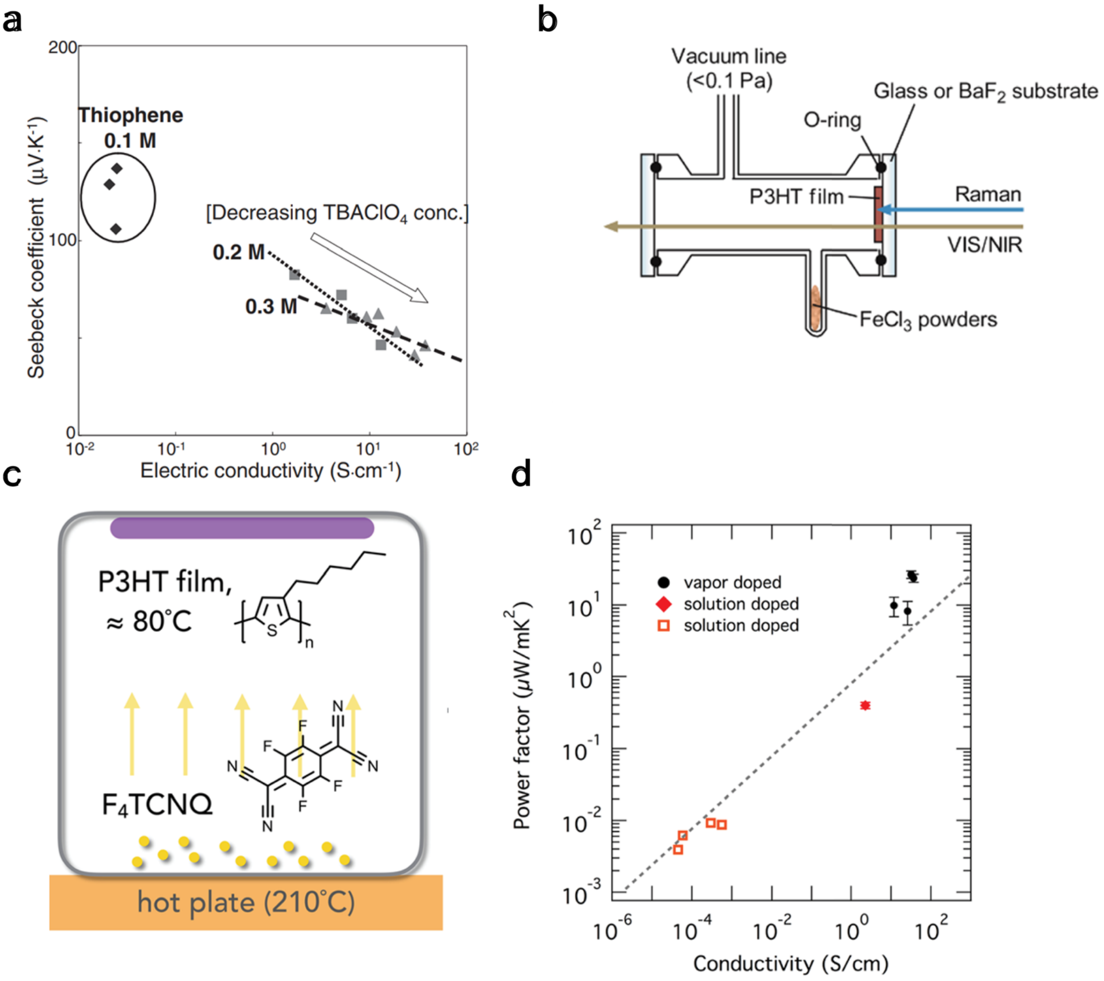

Fig. 7 Thermoelectric properties from polymers made through electrochemical polymerization (a) and oxidative polymerization (b–d). (a) Seebeck coefficient *vs.* electrical conductivity of polythiophene thin films produced at 2 mA cm^2 for changing concentrations of thiophene and tetra-*n*-butylammonium perchlorate (TBAClO$_4$). Reproduced with permission.[176] Copyright, 2009, *Japanese Journal of Applied Physics*. (b) Schematic of a cell for *in situ* absorption of FeCl$_3$ onto a P3HT film. Reproduced with permission.[178] Copyright, 2015, American Chemical Society – JPCB. (c) Schematic of a vapor doping method with organic dopant F$_4$TCNQ onto a P3HT film, (d) power factor of P3HT film as a function of electrical conductivity for different doping methods; filled circles is vapor doped,[179] filled rhombus is solution doped,[146] and hollow square is solution doped.[153] Reproduced with permission.[179] Copyright, 2018, American Chemical Society – CM.

aniline.[181] Yamamoto and Furukawa[178] demonstrated vapor phase oxidation of P3HT thin films with FeCl$_3$ (Fig. 7(b)). Upon creating a vacuum (<0.1 Pa), doping initiates, and through VIS/NIR absorption and Raman spectra, it was found that positive polarons form. These polarons convert to bipolarons upon further doping over approximately 10 hours. Lim *et al.*[179] explored an alternative vapor doping method for P3HT film with F$_4$TCNQ by placing the dopant on a hotplate parallel to the film (Fig. 7(c)). They discovered that this method, suitable for organic dopants, is much quicker (approximately 20 minutes) and results in a higher power factor by an order of magnitude compared to solution-based introduction techniques of F$_4$TCNQ to P3HT, as depicted in Fig. 7(d).

4.5 Chain alignment and microstructure orientation

An increased chain alignment reduces phonon scattering and enhances thermal conductivity. It also diminishes charge carrier scattering, thereby boosting electrical conductivity without necessarily increasing the number of charge carriers. Hynynen *et al.*[182] demonstrated that stretching P3HT doped with either the molybdenum tris(dithiolene) complex Mo(tfd-COCF$_3$)$_3$ or F$_4$TCNQ leads to an increase in electrical conductivity while maintaining a constant Seebeck coefficient (Fig. 8(a)). Meanwhile, Hiroshige *et al.*[183,184] demonstrated that butoxy-substituted phenylenevinylene polymer (P(BuOPV-*co*-PV)) has the Seebeck coefficient initially decreasing and then increasing, following an inverted parabolic shape with increasing draw ratio. The regular peak for electrical conductivity and the inverted peak for the Seebeck coefficient are observed at a stretching ratio of 7, as shown in Fig. 8(b). They noted that the initial rise in electrical conductivity is due to increased carrier concentration, and further stretching broke the chain ends due to increased strain, which decreases the carrier concentration. This suggests a trade-off between the

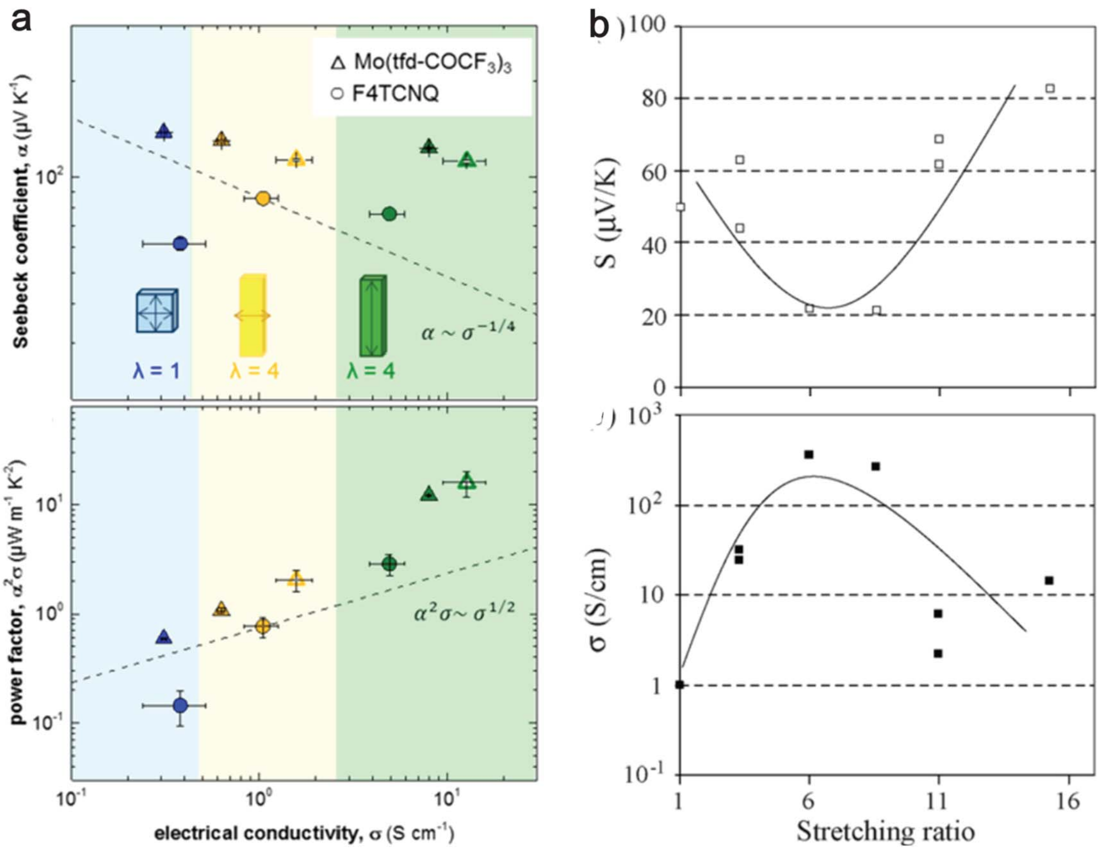

Fig. 8 Effect of stretching ratio on thermoelectric properties of conducting polymers. (a) The top panel shows the electrical conductivity *vs.* Seebeck coefficient, and the bottom panel shows the power factor *vs.* electrical conductivity for P3HT doped with Mo(tfdCOCF$_3$)$_3$ (triangles) and F$_4$TCNQ (circles); closed symbols indicate 48 h doping; open symbols indicate 72 h doping; dashed lines show the empirical trends $\alpha \sim \sigma^{-1/4}$ and $\alpha^2\sigma \sim \sigma^{-1/2}$. λ is the stretching ratio, with the blue shaded region being unstretched, the yellow shaded region being stretched perpendicular to temperature difference, and the green shaded region indicating the stretched region in the direction of temperature difference. Reproduced with permission.[182] Copyright, 2019, American Chemical Society – ML. (b) The top panel shows the Seebeck coefficient with the stretching ratio, and the bottom panel shows the electrical conductivity with the stretching ratio for P(BuOPV-*co*-PV) at 313 K. Reproduced with permission.[184] Copyright, 2007, *Synthetic Metals*.

Seebeck coefficient and electrical conductivity in highly oriented polymers.

Nevertheless, this improvement in power factor may be offset by a rise in thermal conductivity due to the alignment of the chains. Typically, a high draw ratio (greater than 10) is necessary to enhance thermal conductivity significantly. However, it is noted from Fig. 8(a) that a relatively lower draw ratio of 4 can amplify electrical conductivity by a factor of 40. This suggests the possibility of searching for an optimal draw ratio where electrical conductivity increases substantially without a corresponding significant increase in thermal conductivity and a decrease in the Seebeck coefficient. Future studies with measurements of all three critical properties (κ,σ,S) of thermoelectric materials with changes in draw ratio will be able to address the optimal draw ratio for maximal *ZT* of OSCs.

In the study of OSCs, various techniques are available for achieving chain alignment and creating oriented microstructures, such as mechanical stretching,[185,186] friction transfer,[187] secondary doping,[188,189] mechanical rubbing,[190] electric field,[191] electrodeposited nanowires,[192] printing using thermoelectric inks,[161] and flow coating.[193] However, previous research employing these methods lacks comprehensive data on the thermal conductivity and thus does not completely understand the material's thermoelectric performance, specifically its *ZT*. This article will not delve deeper into these alignment methods and direct readers to the review by Deng and Chen[194] for a detailed review.

4.6 Modifications in backbone and side chain

The molecular design of conjugated polymers, encompassing both the backbone and sidechain, enables the engineering of HOMO and LUMO levels. Modifying the molecular structure tunes the band gap of the conjugated molecule and the absolute energy level compared to the dopant. Beyond adjusting energy levels, other aspects, such as charge carrier mobility and chain packing, are also influenced.[198] Notably, the impact of molecular design on energy levels is more pronounced in small-molecule OSCs. Consequently, the studies discussed in this subsection focus on n-type polymers, as p-type polymers have longer chain lengths and more complex morphology. Molecular design methods (Fig. 9) include adding polar groups to the

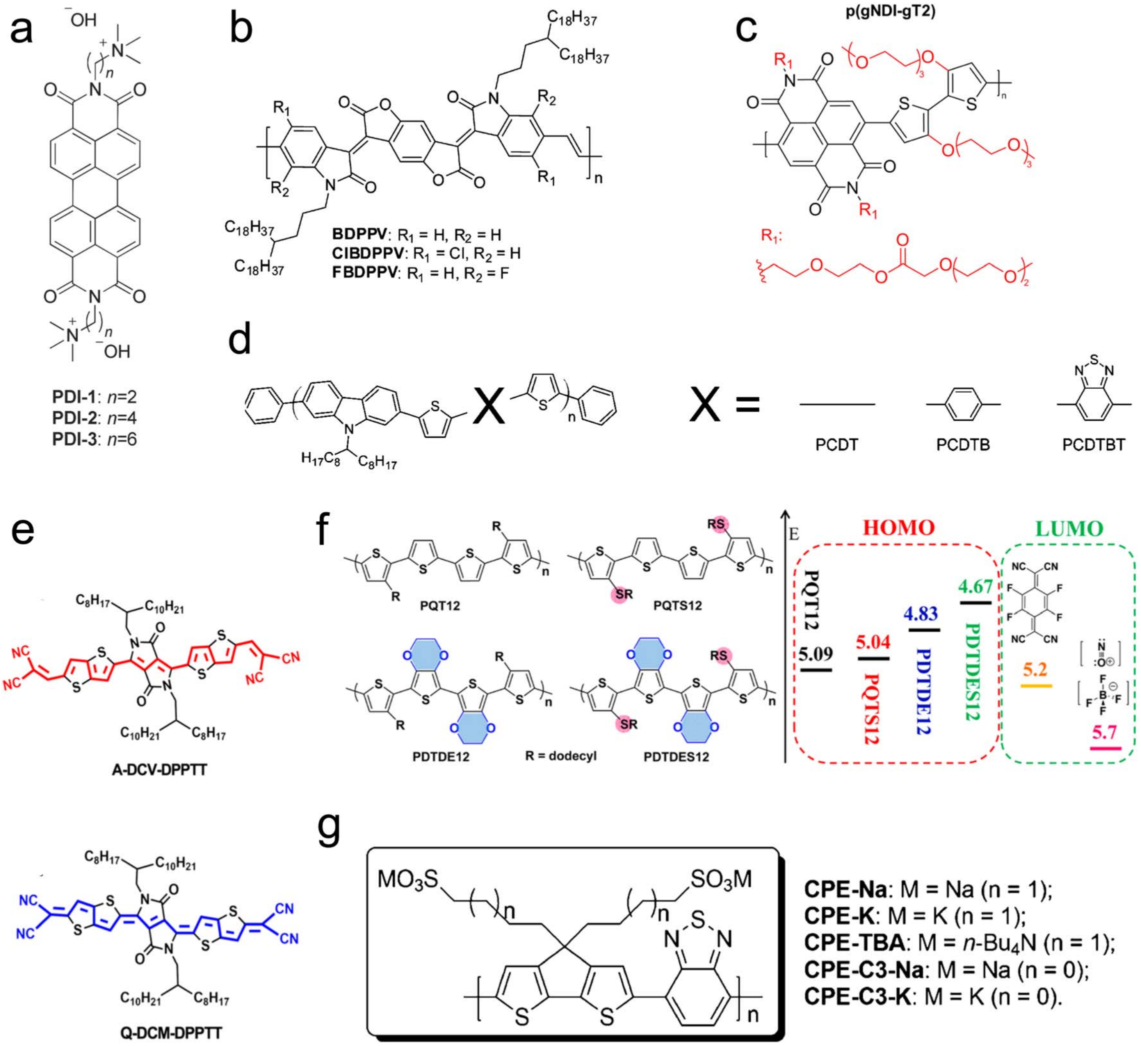

Fig. 9 Chemical structures of conjugated polymers showing different strategies to modify the polymer backbone and side chain. (a) Changing the tethering alkyl chain length between the perylene diimides (PDI) polymer and charged dopant/side-group in the self-doped polymer. Reproduced with permission.[195] Copyright, 2014, Wiley – *Advanced Materials*. (b) Introducing halogen atoms to benzodifurandione-based polyphenylene vinylene (BDPPV) polymer backbone. Reproduced with permission.[148] Copyright, 2015, American Chemical Society – JACS. (c) Adding polar side chains to naphthalenediimide-based co-polymer. Reproduced with permission.[196] Copyright, 2018, American Chemical Society – EL. (d) Changing a backbone with different groups for poly(2,7-carbazole) derivatives. Reproduced with permission.[197] Copyright, 2009, American Chemical Society – CM. (e) Different molecular orientation of solution-processable dipyrrolo-[3,4-*c*] pyrrole-1,4-diylidene)bis(thieno [3,2-*b*]thiophene (DPPTT) derivatives. Reproduced with permission.[198] Copyright, 2017, *Materials Science and Engineering Reports*. (f) Chemical structures and orbital energy levels for poly(bisdodecylquaterthiophene) derivatives. Reproduced with permission.[199] Copyright, 2017, American Chemical Society – JACS. (g) Changing counterions and tethering alkyl chain lengths for self-doped conjugated polyelectrolyte cyclopenta-[2,1-*b*;3,4-*b*′]-dithiophene-alt-4,7-(2,1,3-benzothiadiazole). Reproduced with permission.[200] Copyright, 2014, American Chemical Society – JACS.

backbone,[196] alteration of the backbone orientation, modification of the side-chain length, changes in the dopant, polymer tethering length, and incorporation of halogen atoms into the backbone.

Russ *et al.*[195] employed a self-doping method to investigate the thermoelectric properties of an n-type conjugated polymer, perylene diimides (PDI), with a charged doping group attached to the end, as illustrated in Fig. 9(a). They varied the alkyl chain length, tethering the conjugated backbone to the dopant (2, 4, and 6 methyl groups). Their findings revealed that increasing the alkyl chain length by two carbons increased the power factor by one order of magnitude—similarly, Mai *et al.*[200] delved deeper into self-doping by varying the side-chain length and counter ions for a conjugated polyelectrolyte (cyclopenta-[2,1-*b*;3,4-*b*]-dithiophene-alt-4,7-(2,1,3-benzothiadiazole)) (Fig. 9(f)). They observed that shorter chain lengths increase power factors and improve molecular orientation. Additionally, they demonstrated that altering counter-ions from potassium to sodium can quadruple the power factor. Endrődi *et al.*[201] also reported that shorter alkyl side chains between the polymer and counterion correlate with a higher power factor (Fig. 9(g)).

To examine the role of molecular orientation, Huang *et al.*[198] utilized two n-type molecules: aromatic-dicyanovinyl-dipyrrolo [3,4-*c*] pyrrole-1,4-diylidene)-bis(thieno[3,2-*b*] thiophene (A-

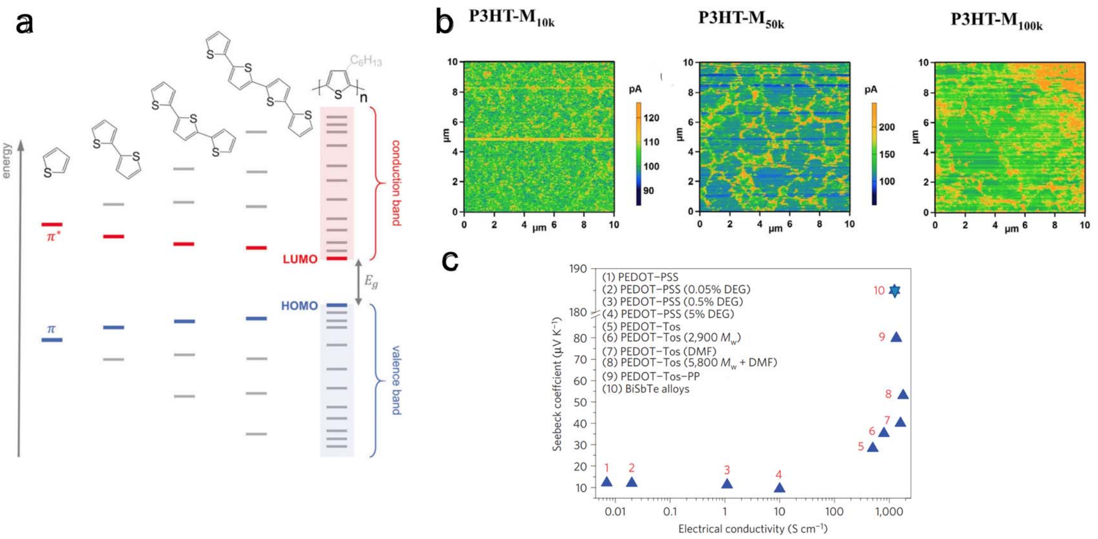

Fig. 10 Effect of molecular weight or chain alignment on charge and thermoelectric transport. (a) Evolution of HOMO and LUMO levels with increasing thiophene units. Reproduced with permission.[143] Copyright, 2017, Wiley – *Advanced Materials*. (b) Conductive AFM scans for a bias of 0.1 V for P3HT films with different molecular weights. Reproduced with permission.[202] Copyright, 2018, Wiley – CAJ. (c) Seebeck coefficient and electrical conductivity of various PEDOT derivatives (including variation of dopants, solvent concentration, and molecular weight). Reproduced with permission.[203] Copyright, 2012, Royal Society of Chemistry – EES.

DCV-DPPTT) and quinoid-dicyano-methylene-dipyrrolo[3,4-*c*]pyrrole-1,4-diylidene)bis(thieno-[3,2-*b*]thiophene (Q-DCM-DPPTT), with a dopant of N-DMBI. A slight variation in the backbone and molecular orientation of A-DCV-DPPTT and Q-DCM-DPPTT is shown in Fig. 9(e). The LUMO level of A-DCV-DPPTT is −3.9 eV, compared to −4.5 eV for Q-DCM-DPPTT, while the HOMO level of N-DMBI is −4.4 eV. The energy level alignment between A-DCV-DPPTT and N-DMBI facilitates efficient charge transfer and results in an order of magnitude difference in the power factor between the two conjugated polymers. Furthermore, a high *ZT* of 0.23 at 373 K and 0.11 at room temperature was observed.

Backbones can also be modified by incorporating a halogen atom or adding a molecular group. Employing the former approach, Shi *et al.*[148] studied an n-type polymer, benzodifurandione-based polyphenylene vinylene (BDPPV), doped with N-DMBI. They discovered that introducing a halogen atom, as shown in Fig. 9(b), significantly enhances charge carrier mobility and doping levels, with chlorine introduction increasing the power factor fivefold and fluorine introduction tenfold. Utilizing the latter approach, Aïch *et al.*[197] changed the polymer backbone for poly(2,7-carbazole) derivatives by introducing different molecules, as shown in Fig. 9(d), resulting in a threefold improvement in the power factor.

4.7 Effect of molecular weight and chain length

The molecular weight, or chain length, critically affects the conjugated polymer's solubility and viscosity, influencing its processability from solution and melt.[143] One notable challenge associated with high molecular weight polymers is their reduced processability, which can impede doping efficiency and complicate the fabrication of flexible thermoelectric devices. However, a significant effect of increased molecular weight in polymers like polythiophene is the narrowing of the bandgap between the HOMO and LUMO levels (Fig. 10(a)). This reduction in bandgap is associated with an increase in electrical conductivity, albeit at the cost of a decreased Seebeck coefficient.

The molecular weight reflects the non-uniform chain lengths within the polymer. This non-uniformity can potentially hinder effective connectivity between chains. It has been shown by Qu *et al.*[202] that increasing molecular weight increases connectivity. They investigated the thermoelectric performance of P3HT films with three different molecular weights of ∼10k, 50k, and 100k g mol^{-1}. They found that P3HT-M$_{50k}$ has higher electrical conductivity than P3HT-M$_{100k}$ and P3HT-M$_{10k}$. In contrast, the Seebeck coefficient remains the same for all three molecular weight polymers. Conductive-AFM analysis at 0.1 V bias revealed that longer molecular chains facilitate better connectivity (Fig. 10(b)). Here, regions with high conductivity (electrical current $I > 200$ pA) indicate domains with enhanced carrier delocalization, likely due to a more ordered structural arrangement. In contrast, regions with poor conductivity ($I < 200$ pA) can be seen as domains with reduced carrier delocalization, possibly arising from a disordered structural configuration. The P3HT-M$_{10k}$ film displays a scattered distribution of high-conductivity areas. In contrast, the P3HT-M$_{50k}$ and P3HT-M$_{100k}$ films demonstrate the presence of conductive zones forming network-like structures. Notably, the network structure in the P3HT-M$_{100k}$ film appears more aggregated compared to that in the P3HT-M$_{50k}$ film. Further, Bubnova *et al.*[203] observed increased Seebeck coefficient and electrical conductivity with increasing molecular weight in PEDOT:Tos, a conjugated p-type polymer (Fig. 10(c)). This increase in charge carrier mobility, accompanied by a rise in the Seebeck coefficient, is attributed to improved molecular orbital energy level alignment at higher molecular weights.

4.8 Effect of crystallinity and morphology

Increasing crystallinity within conducting polymers enhances charge carrier mobility and chain packing[204] while simultaneously reducing dopant miscibility. Crystallinity can be affected by synthesis protocol and post-synthesis methods. Deng *et al.*[205] studied melt and solution processing protocols using P3HT as a model system. They showed that solution-processed films have higher TE performance due to their edge-on crystalline orientation and solid-state ordering. Meanwhile, melt processing leads to reduced conjugation length and TE performance. Several post-synthesis methods exist to alter the crystallinity, such as annealing, adjusting the pH level[206] using an ionic liquid, modifying side-chain length, and employing solvent treatment.[203,207]

Most OSCs cannot endure very high temperatures, rendering annealing processes less explored for pure polymers. Wolfe *et al.*[208] conducted post-treatment thermal annealing on a blend of nickel ethenetetrathiolate (NiETT), an n-type organic thermoelectric material, and PVDF. They observed a steady increase in both electrical conductivity (from 6 ± 2 to 23 ± 3 S cm^{-1}) and the Seebeck coefficient (from -28 ± 3 to -74 ± 4 μV K^{-1}) with rising annealing temperatures (Fig. 11(a)). This enhancement was attributed to improved chain packing, as evidenced by thermogravimetric analysis-mass spectroscopy (TGA-MS) results. Huang *et al.*[209] studied the effect of annealing on the most popular PEDOT:PSS systems and found an optimized annealing temperature of 220 °C, which increased the thermoelectric power factor by 162 times compared to pristine film. They showed that annealing leads to microstructural evolution, characterized by improved crystallinity, increased grain size, and a transformation in domain morphology from spherical granule to nanofibril. These changes facilitate more efficient carrier transport mechanisms, improving the materials' electrical conductivity and overall thermoelectric properties. In a different study,[210] they explored solvent de-doping on 220 °C annealed PEDOT:PSS systems and found that a DMSO treatment increased the power factor by 216 times compared to pristine film.

In a recent study by Duan *et al.*,[211] three different polymers with varying side chains were examined: C12NR ($C_{12}H_{25}$), CFNR ($C_{10}H_{20}$–C_6F_{13}), and C16NR ($C_{16}H_3$). It was found that C16NR, possessing the longest alkyl chain, exhibited the weakest crystallinity. Conversely, CFNR, which has the shortest alkyl chain, displayed the highest crystallinity. Interestingly, the power factor for C12NR was two to four times higher than the other two polymers. This suggests that increasing crystallinity negatively impacts the uniformity and miscibility of doping, as shown in Fig. 11(b), leading to decreased electrical conductivity. The shorter alkyl chain in C12NR enhances molecular packing and morphology.

The influence of pH level on polymer properties also extends to conformational and packing changes and de-doping effects[212] as shown in Fig. 11(c). Kong *et al.*[214] discovered that the intrinsic pH of PEDOT:PSS is approximately 2.3. They noted increased grain size and power factor by reducing the pH using oxalic acid or HCl. The highest power factors were achieved at a pH of 0.2 with oxalic acid and 0.4 with HCl, indicating a synergistic effect of grain modification and oxidation level changes—furthermore, Luo *et al.*[213] investigated the impact of various solvents on doped PEDOT:PSS. They found that PEDOT grains elongated by DMSO exposure resulted in a higher power

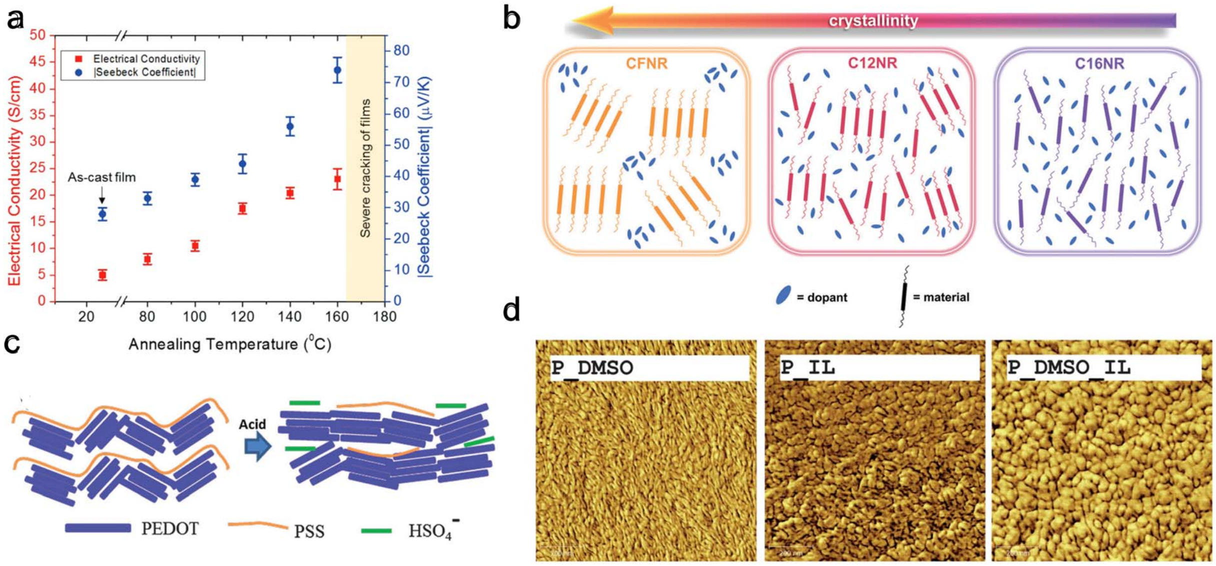

Fig. 11 Modifying crystallinity and morphology through different methods. (a) Annealing, Seebeck coefficient, and electrical conductivity with increasing annealing temperature for nickel ethenetetrathiolate and PVDF blend. Reproduced with permission.[208] Copyright, 2018, Wiley – AFM. (b) Doping uniformity and miscibility for polymers with different crystallinity and side chains. Reproduced with permission.[211] Copyright, 2023, Wiley – *Advanced Science*. (c) Schematic of possible conformations changes upon exposure to sulfuric acid for PEDOT:PSS. Reproduced with permission.[212] Copyright, 2016, Royal Society of Chemistry – JMCC. (d) AFM scanning (surface morphology) after different solvent treatments for PEDOT:PSS, scanning area (1 μm × 1 μm). Reproduced with permission.[213] Copyright, 2013, Royal Society of Chemistry – JMCA.

factor compared to the circular grains formed following exposure to an ionic liquid, 1-ethyl-3-methylimidazolium tetrafluoroborate ($EMIMBF_4$) or (IL) Fig. 11(d). This improvement is attributed to a more favorable orientation of the polymer backbone in elongated grains *versus* circular ones. Notably, the highest power factor was achieved when the polymer was treated with a combination of $EMIMBF_4$ and DMSO. Chen *et al.*[215,216] showed that ionic liquid acts as a de-doping agent and induces phase separation in PEDOT:PSS single-walled carbon nanotube (SWCNT) systems forming linear quinoid conformation. This showed an improvement in thermoelectric performance. In a different study, Chen *et al.*[217] showed that ionic liquid also increases the mechanical strength and self-recoverability of PEDOT:PSS/PVA/SWCNT composites.

5. Molecular scale effects for thermal transport in polymers

This section discusses the complex relationship between polymer molecular-scale traits, phonon transport characteristics, and the resultant thermal conductivity. Typically, electrically insulating polymers have phonons as the dominant energy carrier. In contrast, for semiconducting polymers, both polarons and phonons can be dominant energy carriers depending on the polymer's electrical conductivity.

A primary focus here is polymers with phonon as the dominant energy carrier; however, Section 5.8 discusses the effect of inter-related charge and phonon transport on thermal transport in OSCs. Notably, the contribution of charge transport to thermal transport can be engineered to create a low thermally conductive polymer. The discussion begins with the effect of molecular chain length. Then, it explores various molecular properties that deviate from ideal phonon transport observed in a single chain, such as backbone structure, conformation, and inter- and intra-molecular interactions. Further, the section covers nano- and molecular-engineering approaches to reduce phonon scattering by enhancing polymer crystallinity, aligning molecular chains, engineering intermolecular interactions, and reinforcing bond stiffness and long-range order offer ways to improve thermal conductivity in polymers.[218] The molecular effects and engineering methods discussed in the sub-sections cover many polymers.

5.1 Molecular chain length

Single polymer chains are widely considered model systems for studying unusual thermal transport effects in one dimension (1-D). The pioneering work was performed by Fermi, Pasta, and Ulam (FPU)[219] in the 1950s. FPU computationally studied a 1D non-linear dynamic system with quadratic, cubic, and broken-linear terms. A striking observation from their numerical simulation was that the thermal conductance of an atomic chain increases divergently with the chain length ($G_{\text{th}} \propto L^{\beta}$, $\beta > 0$), in conflict with the Fourier law, which states that thermal conductance is inversely proportional to the chain length ($G_{\text{th}} \propto L^{-1}$). Such a counterintuitive prediction has attracted increasing attention over the past decades and has been studied extensively from a theoretical perspective.[220] In particular, simulations have been performed based on various methods such as molecular dynamics,[184] Green–Kubo,[218] and non-equilibrium Green function (NEGF),[221] and some calculations have reported the value of $\beta = 0.4$ as a general characteristic of 1D chains. Addressing the FPU divergence question necessitates a non-perturbative approach rooted in many-body physics.[105,222,223]

Beyond the idealized 1D atomic chain, polymer chains with well-defined molecular backbone and side chains have also been studied extensively due to their direct relevance to potential applications of the FPU problem. Simulations on single polyethylene chains and polymer chains of aromatic monomers have found that a single polymer chain could be 1000 times more conductive thermally than a typical bulk polymer. Specifically, Henry and Chen[232] used MD simulations to calculate the thermal conductivity of 1D polyethylene (PE) chains and confirmed the divergent thermal transport behavior predicted by FPU (Fig. 12(a)). They have observed the highest thermal conductivity in carbon-based materials (>1000 W m^{-1} K^{-1}) with phonon group velocities reaching 15 000 m s^{-1}. This divergence is primarily attributed to increased phonon relaxation time due to aligned monomer segments.[224]

Shorter molecular junctions (MJs) are another essential model system for understanding the length-dependent thermal transport in polymers. Segal *et al.*[220] calculated the thermal conductance of short alkane MJs using the Langevin equation and found that thermal conductance increases for MJs with less than five carbon atoms and is constant for MJs with more than ten carbon atoms. In contrast, *ab initio* simulations[225,226] suggested that phononic conductance in alkane MJs is nearly independent of the molecular length—further, recent work by Leitner *et al.*[227,228] found that ballistic phonon transport is valid for short MJs with slow thermalization. Phonon transport in longer molecules with quick thermalization is predicted to break the ballistic picture, leading to inelastic phonon scattering in MJs. These results suggested significant contradictions in different models, which could be resolved by experimentally quantifying the length-dependent thermal conductance of single MJs.

For a realistic polymer system, the extended chain length introduces mechanical constraints like bending, torsion, nonbonding, and convection.[229] Jiang *et al.*[221] studied a PE chain of 100 nm in length and calculated a definitive upper limit for thermal conductivity ($\kappa = 310$ W m^{-1} K^{-1}) and Young's modulus ($E = 374.5$ GPa). Further computational studies on materials other than PE have found diverging thermal conductivity in single-chain forms. For instance, crystalline polythiophene[230] (PT) was found to have $\kappa = 198$ W m^{-1} K^{-1} at 100 nm in length. Nonetheless, not all polymers exhibit FPU divergence since some mechanical constraints are more pronounced in specific systems. For example, the unsaturated hydrocarbons, such as carbyne and cumulene chains, exhibit finite thermal conductivities[231] as the angular bending potential shown in these chains effectively curbs the extensive fluctuations within the chain.

Beyond the 1D polymer structures, a higher-dimensional configuration with one dimension constituted of long single

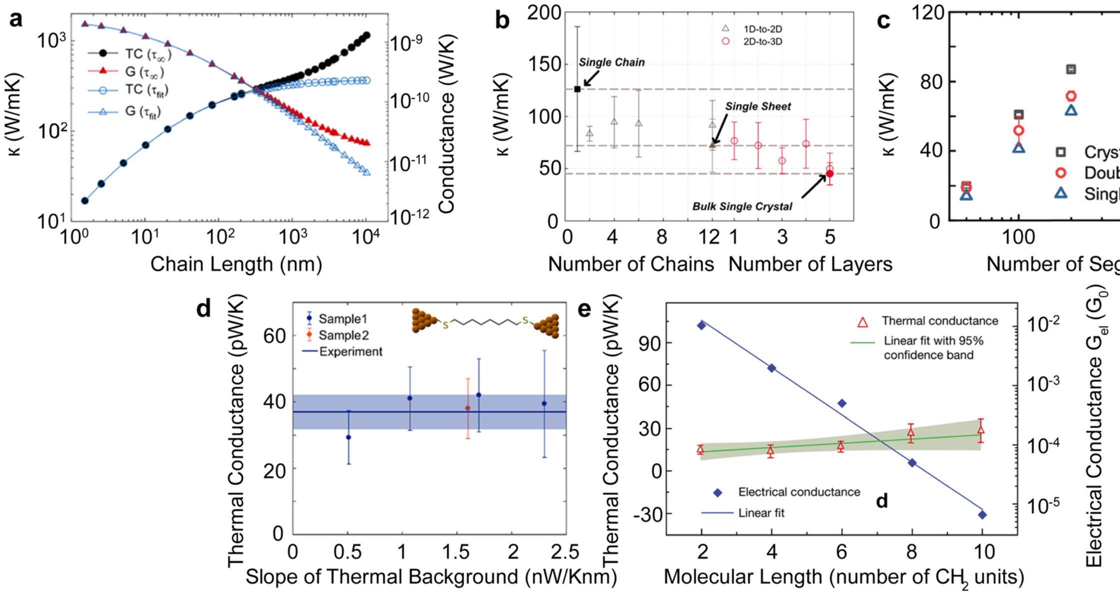

Fig. 12 Thermal conductivity divergence studies. (a) The infinite diverging thermal conductivity and corresponding thermal conductance of polyethylene single chain. Reproduced with permission.[232] Copyright, 2008, American Physical Society – PRL. (b) Thermal conductivity transition from 1D (single chain) – 2D (single sheet) – 3D (single crystal) for polyethylene. Reproduced with permission.[218] Copyright, 2010, American Physical Society – PRB. (c) Thermal conductivity for single-chain, double-chain, and crystal as a function of a number of segments of poly(*p*-phenylene). Reproduced with permission.[233] Copyright, 2023, American Chemical Society – JPCB. (d) Experimental measurement of thermal conductance for octane-dithiol. Reproduced with permission.[234] Copyright, 2019, American Chemical Society – NL. (e) Thermal conductance and electrical conductance of single-molecule (alkanedithiols) with increasing length. Reproduced with permission[27] Copyright, 2019, *Nature*.

chains has thermal conductivity decreasing with increasing dimensionality due to augmented inter-chain interactions[218] ($\kappa_{1D} > \kappa_{2D} > \kappa_{3D}$) (Fig. 12(b)). Conversely, the relation between thermal conductivity and dimensionality can be inverted if the chains are bonded and aligned in the perpendicular plane to the chain length, as demonstrated by Yang *et al.*[233] in their study of aromatic poly(*p*-phenylene). They showed that the 3-D crystalline form exhibits greater thermal conductivity compared to both double-chain (2-D) and single-chain (1-D) configurations, as depicted in Fig. 12(c). This is because of π–π stacking, a non-covalent interaction between aromatic rings, which leads to the parallel alignment of the rings. This alignment curbs the free rotation of polymer chains and enhances thermal transport along the chain. Notably, this impact appears limited to the interchain thermal conductance between phenyl rings. The above work suggested that a 3-D polymer crystal, engineered through π–π stacking, can serve as a model system to investigate the FPU problem experimentally at the bulk level.

Quantifying the thermal conductance of a single chain and gaining insights into the FPU phenomenon poses significant experimental challenges as it requires the simultaneous control of an atom-sized system and measurement of ultrasmall thermal signal. Two methods are typically employed for experiments involving single-molecule chains. The first method involves placing a self-assembled monolayer between two temperature-differing thermal reservoirs.[235] In this setup, the signal comes from an ensemble of more than 100 molecules, assumed to be thermally parallel. The second technique, single molecule break junction (SMBJ), requires a covalently bonded individual molecule or chain between the thermal reservoirs.[27] The difference in measurement signal before and after breaking the junction accurately determines the molecule's thermal conductance. It is worth noting that this approach yields valuable insights into the FPU problem, as it allows for a direct examination of the length-dependent single-chain thermal transport.

Wang *et al.*[235] conducted a study on the thermal conductance of an alkane monolayer system employing the ultrafast flash technique, encompassing chains with 24 carbon atoms. Their results unveiled a constant thermal conductance across varying chain lengths. However, the extent of chain lengths examined in this study was less than 3 nm and fell short of addressing the divergence described by the FPU problem. The first direct measurement on a single molecule chain was performed by Cui *et al.*,[27] in which they employed SMBJ in conjunction with a time-averaging measurement scheme to quantify the thermal conductance of various lengths of alkane dithiols with carbon atoms from 2 to 10. This approach allowed them to achieve an ultra-high resolution of 80 picoWatt (pW) at room temperature, facilitating the quantification of thermal conductance for single molecules. Their findings revealed that the measured thermal conductance (approximately 25 pW K^{-1}) exhibited a nearly constant value irrespective of chain length (Fig. 12(e)). This result underscores the remarkable consistency of thermal conductance across varying chain lengths for a smaller number of segments. Using a similar technique, Mosso *et al.*[234] investigated the thermal conductance of octane-dithiol, which was found to be 35 pW K^{-1}, as illustrated in Fig. 12(d).

In bulk polymers, the chain length effect on thermal transport is commonly referred to as the molecular weight of the polymer.[237] To study the impact of molecular weight on thermal conductivity, Zhang *et al.*[117] utilized the electrospinning technique to create various types of vinyl nanofibers. Their observations suggested a clear trend that thermal conductivity is strongly correlated with molecular weight, as shown in Fig. 13(a). However, such observations do not provide a definitive insight into the FPU divergency because nanofibers consist of many polymer chains rather than a single chain. This results in more complex inter-chain interactions and chain alignment scattering, potentially overshadowing the increase in thermal conductivity due to divergent phonon transport.

Furthermore, using a post-synthesis method to alter the molecular weight, Yamanaka *et al.*[236,238] irradiated ultra-high molecular weight PE fibers with γ-rays. This study demonstrated that γ-ray exposure effectively broke down the polymer chains, reducing molecular weight and concurrently decreasing thermal conductivity (Fig. 13(b)). It should be noted here that this approach could be practical in introducing defects into conducting conjugated polymers to reduce thermal conductivity without significantly affecting the power factor of the thermoelectric material.

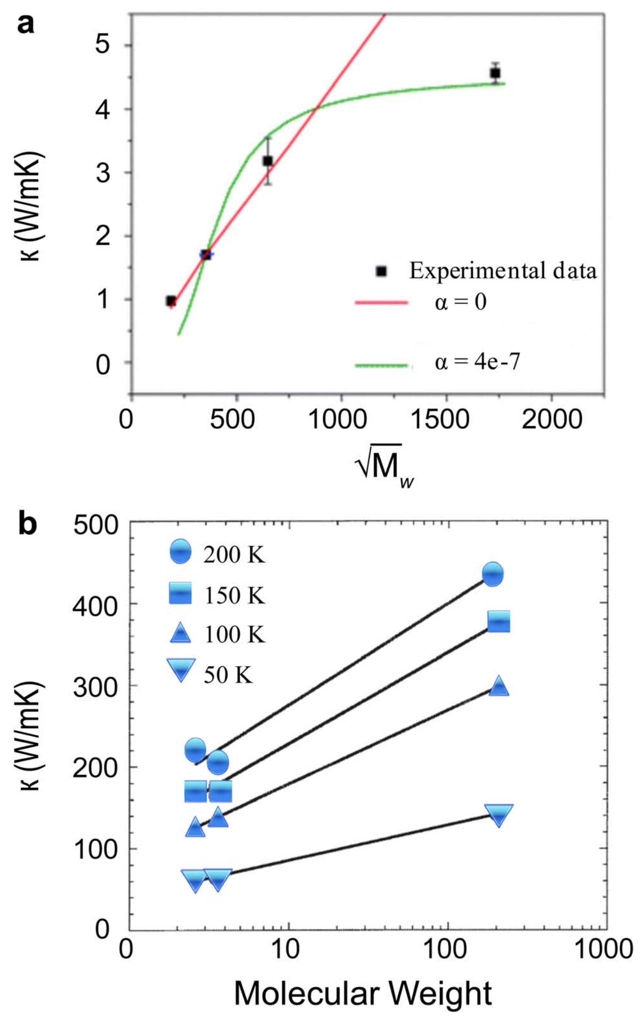

Fig. 13 Experimental engineering methods for varying molecular weight. (a) Measured thermal conductivity of polyethylene nanofibers at 200 K as a function of the square root of the molecular weight. Reproduced with permission.[117] Copyright, 2018, Royal Society of Chemistry – SM. (b) Thermal conductivity as a function of molecular weight for gamma rays irradiated polyethylene fibers. Reproduced with permission.[236] Copyright, 2006, Wiley – JAPC.

5.2 Molecular orientation and chain alignment

A widely studied approach to controlling the thermal transport in polymers involves the manipulation of molecular orientation and chain alignment. Molecular orientation is defined as the specific alignment of molecules within the polymer along a particular axis. This orientation can be induced through various factors,[239] including mechanical stretching, drawing, rolling, extrusion, and exposure to external magnetic and electric fields. Additionally, modification of pH level, bottom-up templating techniques,[130] and fluidic conditions during processing can induce preferable molecular orientation. These techniques often lead to an increased thermal conductivity along the direction of alignment, coupled with decreased thermal conductivity in the perpendicular direction. This section will summarize research efforts in both mechanical strain and non-strain-based nanoengineering methods to improve molecular orientation and chain alignment in polymers.

One of the non-mechanical methods to induce better chain conformation is changing the pH level during solution-based polymer synthesis. By adjusting the pH of polyacrylic acid (PAA), Shanker *et al.*[127] ionized the carboxyl acid groups into carboxylates, facilitating the stretching of the molecular chain. This leads to a stiffer chain conformation with compact chain packing and reduced inter-chain interactions. The increased pH level also changed the inter-chain interactions to include stronger ionic bonding rather than van der Waal's and H-bonding forces. The thermal effect due to different bonding interactions is discussed in Section 4.5. These changes manifested as a notable increase in thermal conductivity, ranging from 0.34 W m^{-1} K^{-1} at a pH of 1 to 1.17 W m^{-1} K^{-1} at a pH of 12, as shown in (Fig. 14(e)).

Shin *et al.*[240] showed that liquid crystal networks (LCN) synthesized under a directional magnetic field ($B_\perp$ or $B_\parallel$) can exhibit preferential molecular orientation. They found an increase in thermal conductivity up to two orders of magnitude for LCN synthesized with a perpendicular magnetic field compared to a parallel magnetic field, as illustrated in (Fig. 14(c)). In the context of the template synthesis method, Cao *et al.*[100] made nanowire arrays (Fig. 14(b)) using a nanoporous template wetting technique and found thermal conductivity to be two orders of magnitude higher than the bulk counterpart.

Besides non-mechanical methods, the most direct method to achieve a higher degree of molecular orientation in semicrystalline polymers involves increasing strain[242] by stretching[243] polymers under temperature (Fig. 14(a)). Stretching temperature and stretching rate play a vital role in improving

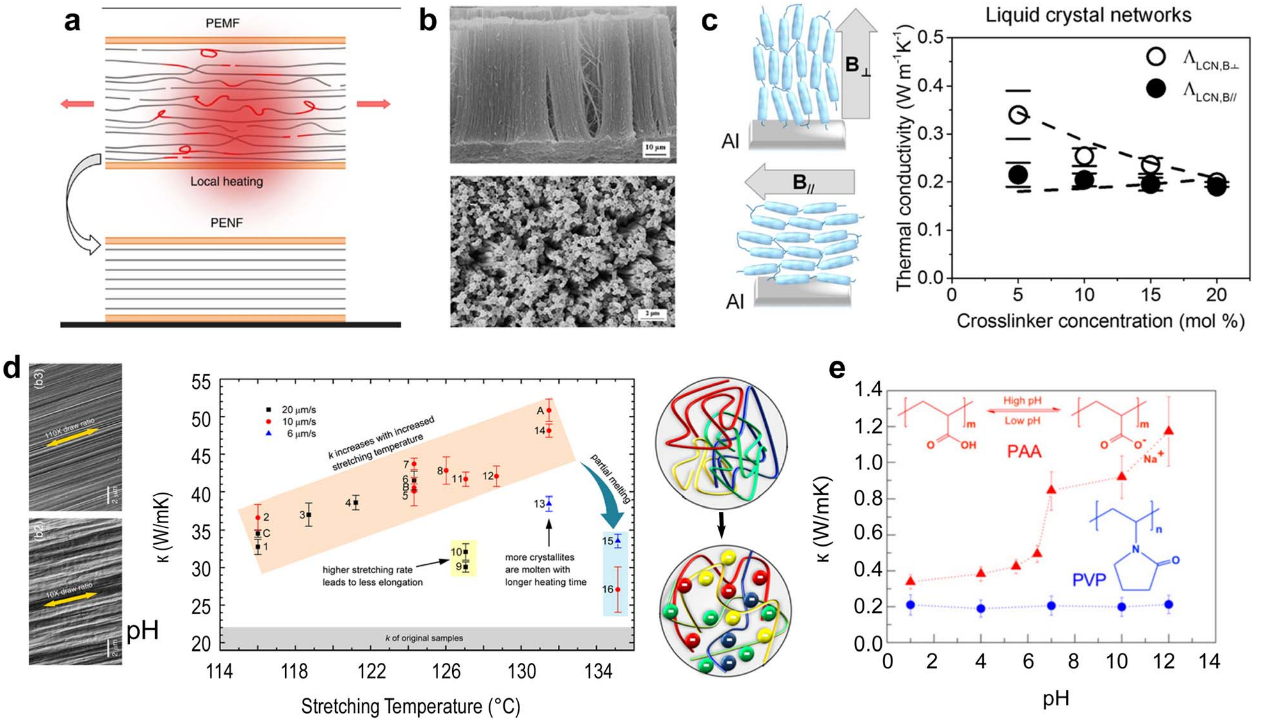

Fig. 14 Different methods to align polymer chains. (a) Schematic of polymer chain stretching with localized heating and under strain to make polyethylene-nanofibers (PENF) from polyethylene-microfibers (PEMF). Reproduced with permission.[94] Copyright, 2018, *Nature Communications*. (b) Scanning Electron Microscopy (SEM) images of high-density polyethylene nanowire array top (side view), bottom (top view). Reproduced with permission.[100] Copyright, 2011, *Polymer*. (c) (Left) Chain alignment with change in magnetic field direction and (Right) thermal conductivity of Liquid Crystal Network (LCN) with varying thiol crosslinker concentration. The two curves show the direction of the applied magnetic field during synthesis. Reproduced with permission.[240] Copyright, 2016, American Chemical Society – ML. (d) (Left) SEM images of polyethylene with drawing ratio and (Right) thermal conductivity as a function of stretching temperature and stretching speed.[241] Copyright, 2017, American Chemical Society – Omega. (e) (Left) Change in polymer chain packing and (Right) thermal conductivity of polyacrylic acid (PAA) and poly(*N*-vinyl pyrrolidone) (PVP) with different pH. Reproduced with permission.[127] Copyright, 2017, Science – SA.

thermal conductivity. Even minor alterations in stretching temperature can significantly impact thermal conductivity. When the rate is slow, the crystallites are molten; when the rate is higher, it leads to the elongation of chains (Fig. 14(d)). Therefore, an ideal stretching rate and temperature can give the desired thermal conductivity for different polymers.[79] Although diverse strategies have been employed to induce strain in polymers, one of the most common techniques involves reducing the fiber diameter or film thickness. The following sub-section provides insight into the methodologies used for synthesizing nanofibers with aligned molecular structures.

5.2.1 **Tensile drawing and rolling.** Plastic deformation, a consequence of the rolling or drawing process, can facilitate chain alignment within a polymer.[244] Ronca *et al.*[116] employed sintering and hot-rolling techniques to stretch polymer sheets into films. Upon performing both uniaxial and biaxial stretching, they revealed that even a straightforward approach like hot rolling can significantly enhance thermal conductivity in all three spatial dimensions. The least conductive plane exhibited a thermal conductivity of 18.4 W m^{-1} K^{-1}, while the highest conductive plane had a thermal conductivity of 60 W m^{-1} K^{-1}. The films prepared through these hot stretching processes appear to comprise self-assembled nanofibers, likely attributed to inter-chain van der Waals couplings[118,245]—additionally, Xiang *et al.*[124] investigated the effects of drawing on PI fibers and observed changes in crystallinity size, which increased from an initial 3.85 nm to 9 nm.

5.2.2 **Sharp tip drawing.** Harfenist *et al.*[246] demonstrated a unique way of drawing PMMA nanofibers using an AFM tip. Initially, micro/nano-droplets of PMMA and solvent mixture are dispensed onto a substrate and joined using the AFM tip before solvent evaporation. Using this technique, fibers with diameters as small as 50 nm and lengths up to 1 mm were successfully fabricated (Fig. 15(a)), with the diameter limited by the tip diameter—similarly, Shen *et al.*[98] employed a sharp tungsten tip or a tipless AFM cantilever to draw PE fibers from a hot decalin and PE gel. The fiber solidifies as the solvent evaporates, resulting in fibers with diameters of 130 nm and draw ratios as high as 400 with thermal conductivity greater than 100 W m^{-1} K^{-1}—another approach by Nain *et al.*[247] utilized a micro-pipette probe-based drawing technique, which led to fibers with a diameter of 200 nm. In this method, a polymer solution is dispensed from a custom pipette probe; the fiber is then slowly drawn vertically, solidifying due to solvent evaporation, before finally separating and falling onto the substrate horizontally (Fig. 15(a)(iv)).

5.2.3 **Transient heat stretching.** Shrestha *et al.*[248] employed a pulsed microheater to reduce PE microfibers to nanofibers

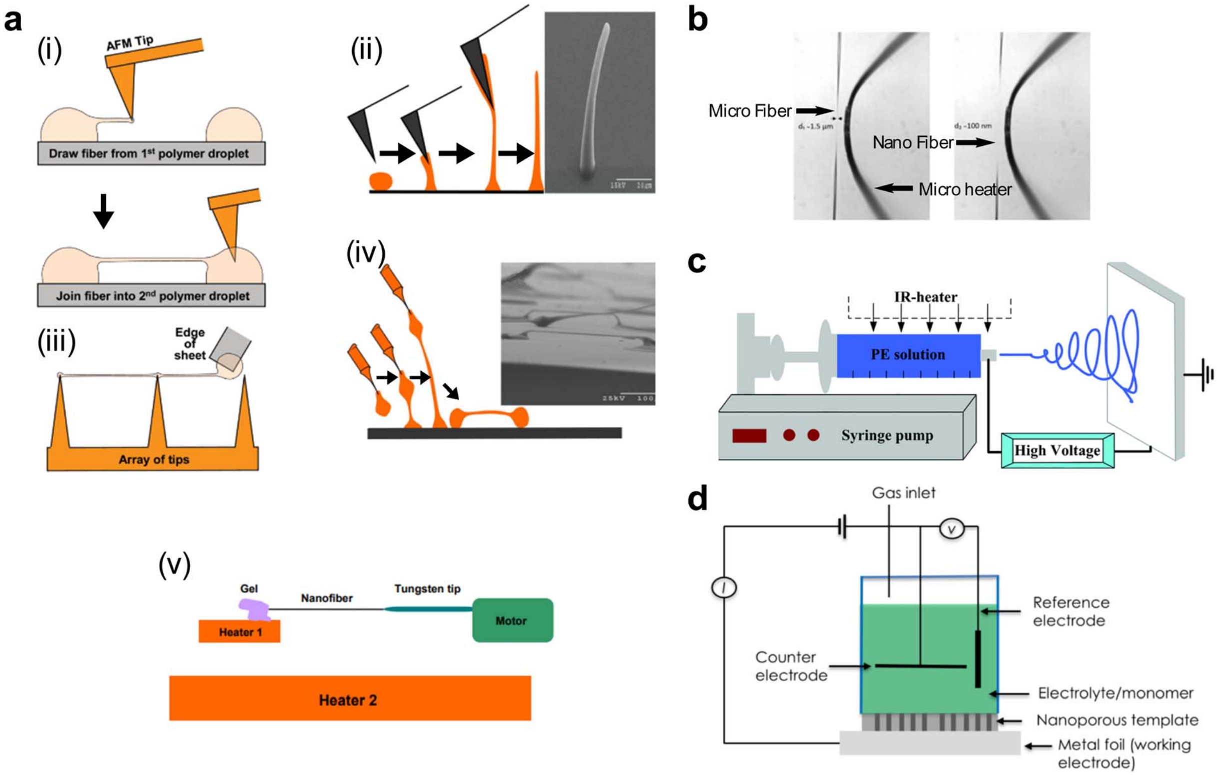

Fig. 15 Different methods to make nanofiber. (a) Sharp tip drawing. (i) Atomic force microscopy (AFM) tip joining two PMMA droplets to make nanofiber. Reproduced with permission.[246] Copyright, 2004, American Chemical Society – NL. (ii) Vertical drawing of PMMA with AFM tip. Reproduced with permission.[247] Copyright, 2006, *Institute of Electrical and Electronics Engineers*. (iii) Joining two sharp tips with the edge of a sheet. Reproduced with permission.[246] Copyright, 2004, American Chemical Society – NL. (iv) Micro-pipette probe-based drawing technique. Reproduced with permission.[247] Copyright, 2006, *Institute of Electrical and Electronics Engineers*. (v) Polyethylene drawing using a sharp tungsten tip on a heating stage. Reproduced with permission.[98] Copyright, 2010, *Nature Nanotechnology*. (b) Transient heat stretching (left) before heating and microfiber, (right) after heating and nanofiber. Reproduced with permission.[138] Copyright, 2018, *Nature Communications*. (c) Schematic of electrospinning setup with an embedded IR heater. Reproduced with permission.[113] Copyright, 2015, Royal Society of Chemistry – *Nanoscale*. (d) Schematic of nanoscale templating technique. Reproduced with permission.[109] Copyright, 2014, *Nature Nanotechnology*.

(Fig. 15(b)). In this method, a microfiber is fixed under strain, and the microheater is pulsed for less than a second to create a turbulent boundary layer with the microfiber in this boundary layer. This quickly stretches the microfiber to nanofiber, yielding a favorable molecular alignment due to the increased temperature. This approach showcases the potential of transient thermal methods in precisely engineering polymer fibers for optimal thermal properties.

5.2.4 Nanoscale templating. In this method, polymers are melted and infiltrated into a porous structure, often made from anodic alumina (Fig. 15(d)). An array of polymer nanofibers with improved chain alignment is formed upon removing the template using a basic aqueous solution. The directional flow of the polymer melt within the nano-porous template serves as the primary factor for this enhanced alignment. Higher thermal conductivity is observed along the axial direction of these nanofibers.[109] Notably, the method results in a bulk-scale thermal interface material comprised of axial nanoscale fibers exhibiting improved thermal conductivity.[249]

5.2.5 Electrospinning. This method applies a high voltage between a sharp conductor—often a syringe needle containing a polymer solution—and a grounded collector.[113] The ensuing electric field induces the formation of a cone-shaped polymer solution from which a jet is propelled toward the collector. As the jet advances, it undergoes significant thinning while the solvent quickly evaporates, culminating in a solid fiber being deposited onto the collector, as depicted in Fig. 15(c). However, one potential issue of this method is that the jet can exhibit instability, causing it to whip erratically and resulting in a disorderly fiber deposition pattern on the collector. Such variations affect the structure and the thermal properties of the resultant nanofibers. Typically, electrospinning is faster than the other stretching methods above but does not give the chains enough time to align. If the spinning speed is slow, the fibers formed will be at micron meter scale instead of nanoscale. However, even with poorly aligned fibers, electrospinning can still have thermal conductivity up to one order higher than its bulk counterparts. As described in detail by Wei *et al.*,[93] several spinning methods are used to make nanofibers.

To facilitate the understanding and comparison of the methods described above, we have provided Table 2 with the measured thermal conductivity using different stretching methods for various polymers.

5.3 Backbone and side-chain effect

The atomic composition, types of bonding interactions, and molecular conformation of a polymer's backbone differ markedly among various polymers, influencing their thermal conductivity. This effect is observed when comparing the thermal conductivities of polymers with identical segment counts but different compositions. For instance, a single PE chain comprising 1000 segments[224] exhibits a thermal conductivity of 50 W m^{-1} K^{-1}, and a single polydimethylsiloxane (PDMS)[250] chain, also with 1000 segments, has a much lower thermal conductivity of 5 W m^{-1} K^{-1}. Despite the same number of segments or chain lengths, this one-order-of-magnitude difference in thermal conductivity can be attributed to the complex influences of the molecular backbone and side chains. The backbone of a polymer refers to the central chain formed by connecting the monomer segments. The backbone, the central chain formed by monomer segments, is crucial as it facilitates approximately 80% of phonon transport in polymers with aligned single chains.[4] Therefore, manipulating the polymer backbone's structure, stiffness, and length is crucial for modifying thermal conductivity.

A key feature determining the backbone effect on thermal transport is the type of chemical bonds between the organic chains. Carbon atoms form planar rings through conjugated π-bonds and sp^2 hybridization in polymers with an aromatic backbone, rendering the structure significantly stiffer than those with aliphatic backbones. This stiffness is due to the restricted rotation and bending of the chains. Liu and Yang[224] calculated that polymers with aromatic backbones exhibited thermal conductivity that is 2.6 times higher than their aliphatic counterparts, as illustrated in Fig. 16(a). When a polymer chain is extended, it may experience increased torsion, leading to a loss of straightness through bending and kinking, which introduces additional phonon scattering.[251] Duan *et al.*[252] found that increasing the number of kinks in PE chains leads to more phonon scattering centers, leading to reduced thermal conductivity, as shown in Fig. 16(b). Remarkably, even a single kink can induce diffusive-like scattering for more than half of the phonons, significantly diminishing the thermal conductivity by half in a 141 nm long polymer.

In polymers with side chains, additional thermal pathways are introduced beyond transport through the backbone. Generally, incorporating heavier and longer side chains results

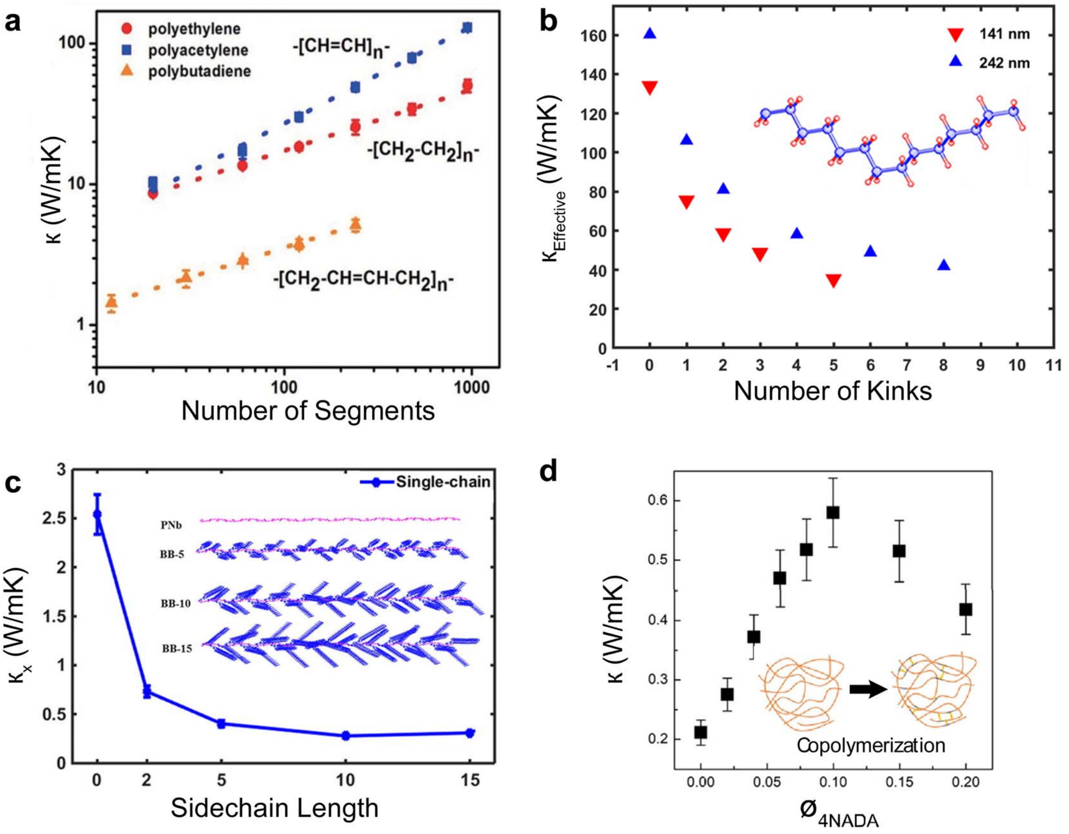

Fig. 16 Backbone and side-chain effects. (a) Thermal conductivity of aliphatic (polyethylene) and aromatic (polyacetylene and polybutadiene) single-chain polymer with increasing chain segments. Reproduced with permission.[224] Copyright, 2012, American Physical Society – PRB. (b) Thermal conductivity of polyethylene chain with increasing kinks in the backbone for two different chain lengths (141 nm and 242 nm). Reproduced with permission.[252] Copyright, 2019, American Institute of Physics – JAP. (c) Thermal conductivity of a single-chain polymer with increasing side chain length, inset showing polymer chain with increasing length of sidechain. Reproduced with permission.[253] Copyright, 2017, American Institute of Physics – APL. (d) Thermal conductivity of co-polymerized polyimide with changing mole fraction of 2,4,5,7-tetraamino-1,8-dihydroxyanthracene-9,10-dione (4NADA), inset showing a schematic of polymer before and after copolymerization. Reproduced with permission.[254] Copyright, 2022, Cellpress – *iScience*.

in lower thermal conductivity than lighter and shorter side chains.[255] Furthermore, asymmetric side chains or reducing the distance between neighboring side chains further diminishes thermal conductivity.[117] Ma *et al.*[253] found that the high sensitivity of thermal conductivity to side-chain length diminishes when the length surpasses ten monomer segments (Fig. 16(c)). This is due to phonons decaying and scattering before reaching the end of long side chains, rendering their length inconsequential beyond a certain point. It should be noted that while the absence of side chains is typically preferred for high thermal conductivity in polymers, incorporating longer side chains can be strategically employed to design polymers with extremely low thermal conductivity that favors thermoelectric applications.

Experimentally, a polymer's backbone and side chain can be altered by modifying the monomer segments during chemical synthesis. Adding molecules to the backbone or side chains post-polymerization does not yield a covalently bonded and uniformly distributed alteration throughout the polymer structure. Liu *et al.*[254] copolymerized or doped 2,4,5,7-tetraamino-1,8-dihydroxyanthracene-9,10-dione (4NADA) into the backbone of polyimide (PI) and observed a threefold increase in thermal conductivity at a 10% loading of 4NADA as shown in Fig. 16(d). This enhancement was attributed to the improved intermolecular interactions and heightened structural order facilitated by integrating 4NADA into the polymer backbone. The exploration of doping or polymerization techniques to modulate thermal conductivity, whether to increase or decrease it, has yet to be extensively studied. However, identifying an appropriate combination of these techniques could yield materials with optimized thermoelectric properties or as thermally conductive thermal interface materials.

5.4 Molecular conformation

Molecular conformation refers to the specific spatial shape adopted by a molecule due to the arrangement of its constituent atoms and bonds. In the context of thermal transport along a polymer chain or within the bulk material, the collective molecular conformation of monomer segments can have a significant effect, as molecular conformation is not static and is susceptible to change from factors beyond the monomer level. For example, the lack of long-range order in amorphous regions of polymers leads to complex and irregular molecular conformations.[258]

Three key factors influencing molecular confirmation are chain rotation, dihedral energy, and the nature of chemical bonds and atoms. Chain rotation involves the twisting or turning of monomer segments around their connecting bonds that link them to the rest of the chain. An elevation in the chain rotation factor corresponds to a direct decrease in thermal conductivity, as shown in Fig. 17(a). This decrease stems from a reduction in phonon group velocity, resulting from diminished stiffness from an elevated chain rotation factor.[256] Dihedral energy is the potential energy associated with the rotation of two interconnected chemical groups around a single bond axis. Increased dihedral energy leads to improved lattice order and higher strain, increasing thermal conductivity[257] (Fig. 17(b)).

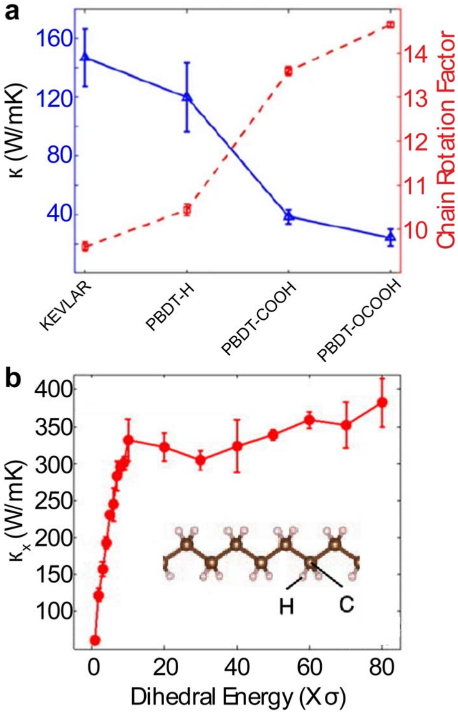

Fig. 17 Molecular confirmation effects on thermal conductivity. (a) Thermal conductivity of stretched single chain as a function of chain rotation factor for Kevlar (polyparaphenylene terephthalamide) and PBDT (poly(2,2′-disulfonyl-4,4′-benzidine terephthalamide)) derivatives. Reproduced with permission.[256] Copyright, 2019, *Journal of Materials Research*. (b) Thermal conductivity of single polyethylene chain with varying dihedral energy. Reproduced with permission.[257] Copyright, 2012, American Institute of Physics – JAP.

Furthermore, certain atoms or molecules within the polymer chain can introduce more significant disorders than others. Liu *et al.*[224] found that poly(methylene oxide) exhibits a lower thermal conductivity than PE due to the oxygen atom's introduction of mass disorder in the poly(methylene oxide) chain—a notable finding by Zhang *et al.*[5] pertains to pi-conjugated polymers, where the overlap of p-orbitals suppresses chain rotation, thereby reducing phonon scattering. Their research underscores that from a molecular conformation perspective, the pi-conjugated polymers are optimal for generating highly thermally conductive nanofibers due to their organized backbones, strong bonds, and robust dihedral angles.

5.5 Inter- and intra-molecular interactions

Intermolecular interactions refer to the forces of attraction or repulsion between molecules in a polymer. These interactions are classified into van der Waals forces (London dispersion, Keesom, and Debye interactions), hydrogen bonding (H-bond), electrostatic, and ion–dipole interactions. The strength and nature of these interactions significantly influence phonon transport between chains. For instance, in crystalline polymers, interchain H-bonds can act as “soft grips”, limiting the twisting motion of polymer chains and enhancing thermal conductivity[259] (Fig. 18(a)). In contrast, intramolecular interactions are the forces that bind the atoms within a molecule together, dictating the molecule's structure and stability. These interactions encompass covalent, ionic, and metallic bonds. The strength or energy associated with these interactions profoundly impacts the polymer's thermal conductivity.[79] The energy tied to bond stretching and angular bending potential affects the rigidity of the molecular structure. When these interactions intensify, they limit the mobility of the polymer chains, which minimizes phonon scattering and boosts thermal conductivity, as illustrated in Fig. 18(b).[260]

The energy associated with different types of interactions varies significantly: van der Waals forces have an energy of (ε) ∼ 0.01 eV, H-bond has an energy (ε) ∼ 0.1 eV, and intermolecular

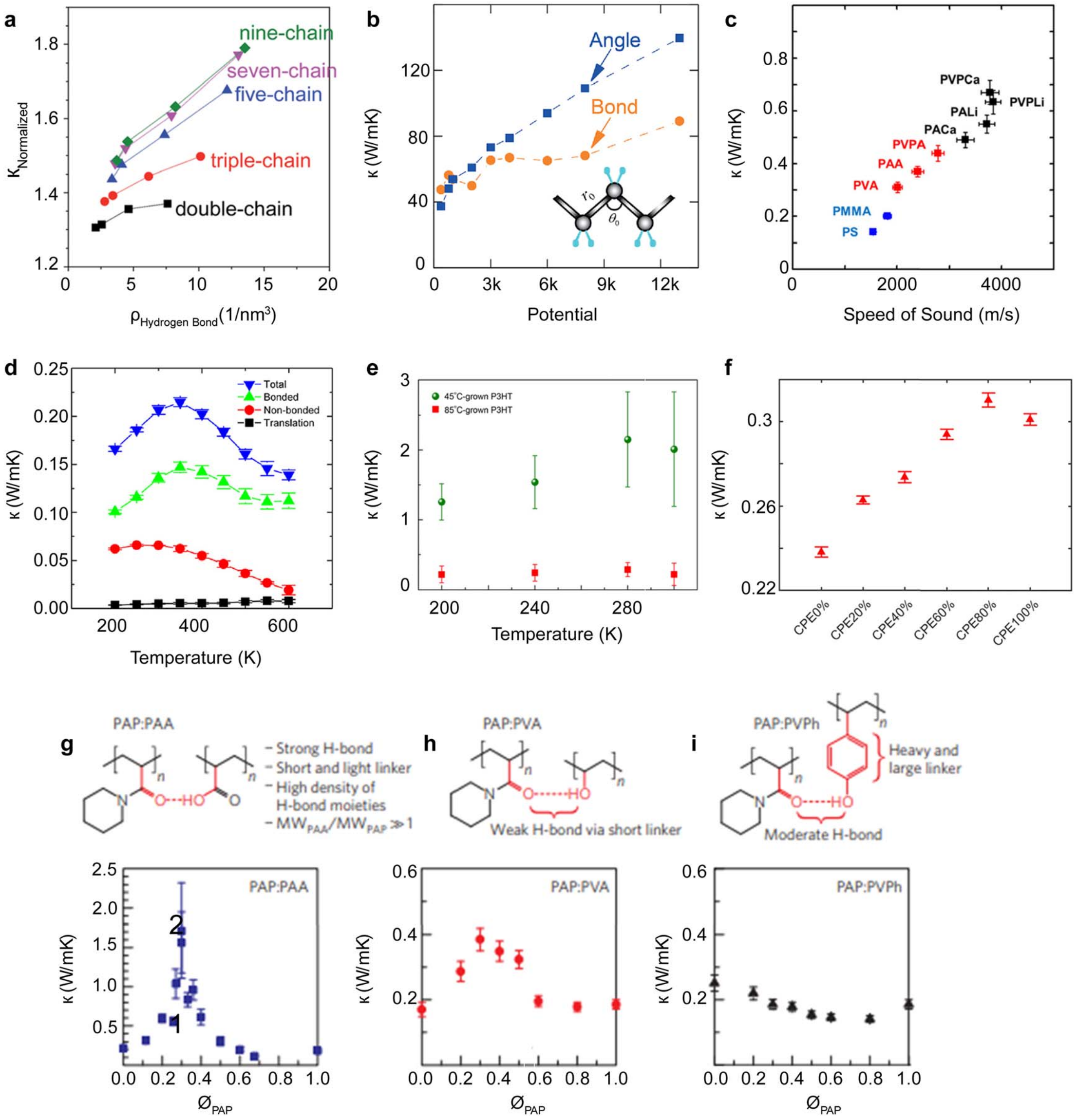

Fig. 18 Effect of inter- and intra-molecular interactions. (a) Normalized thermal conductivity of 20 nylon nanosheets *versus* different density of hydrogen bonds for different number of chains (the thermal conductivity of each nanosheet is normalized by that of a nylon single chain ($m = 1$) that has the same type). Reproduced with permission.[259] Copyright, 2015, Royal Society of Chemistry – *Advances*. (b) Thermal conductivity as a function of bond stretching and angular bending potential. Reproduced with permission.[260] Copyright, 2019, American Institute of Physics – JAP. (c) Speed of sound and thermal conductivity of different polymers with same backbone, PS and PMMA (blue symbols) dominated by van der Waals interactions, PVA, PAA, and PVPA (red symbols) dominated by hydrogen-bond interaction, and PALi, PACa, PVPLi, and PVPCa (black symbols) are polymer salts with ionic interchain bonds. Reproduced with permission.[261] Copyright, 2017, American Physical Society – PRB. (d) Bonded, non-bonded, and covalent contributions to total thermal conductivity for amorphous polyethylene tangled chains with varying temperatures. Reproduced with permission.[262] Copyright, 2016, American Chemical Society – JPCB. (e) Thermal conductivity for poly(3-hexylthiophene) (P3HT) films grown using oxidative chemical vapor deposition at two different temperatures. Reproduced with permission.[128] Copyright, 2018, Science – SA. (f) Thermal conductivity of liquid crystal polyester with a change of the ratio of hydrogen bond donor. Reproduced with permission.[263] Copyright, 2023, Wiley – JAPS. (g) Thermal conductivity of PAP:PVA at various mole fractions of PAP, (h) thermal conductivity of PAP:PVPh at various mole fractions of PAP, (i) Thermal conductivity of PAP:PVPh at various mole fractions of PAP. Reproduced with permission.[264] Copyright, 2014, *Nature Materials*.

bonding has an energy of (ε) ~ 1–10 eV. Xie *et al.*[261] calculated the speed of sound for different bulk polymers, which is related to thermal conductivity from eqn (9). Their findings suggested that polymers characterized by weak van der Waals interactions exhibit the lowest speed of sound, followed by those with hydrogen bonds and ion bonds. This shows that phonon velocity (the speed of sound) increases with the strength of molecular interactions, as shown in Fig. 18(c).

Molecular interactions are subject to external physical effects such as temperature, pressure, pH level, and humidity. As the temperature increases, the contribution of van der Waals interactions to the total thermal conductivity diminishes[262] (Fig. 18(d)). This decrease can be attributed to diminished material weight density and increased molecular spacing at elevated temperatures. Moreover, the vibrational energy of molecules rises with temperature, often surpassing the energy of van der Waals forces at room temperature (vibrational energy at room temperature is $\sim k_\mathrm{B}T = 26$ meV). Concurrently, the contribution of translational (diffusivity) movements to thermal conductivity intensifies at higher temperatures. Different polymerization techniques and control of external conditions make it possible to engineer molecular interactions to tailor the thermal conductivity of polymers to desired specifications. The discussion on the effect of external control on thermal transport and thermoelectricity in polymers is detailed below in Section 7.

Experimentally, bottom-up synthesis methods, involving either modification of the synthesis procedure or adding foreign molecules, are commonly used for engineering molecular interactions and are summarized below.

Xu *et al.*[128] grew thin films of poly(3-hexylthiophene) (P3HT) using the oxidative chemical vapor deposition (oCVD) method, which showed stronger conjugated carbon–carbon double bonds along the extended polymer chains and stronger π–π stacking interactions between chains when compared to chemically synthesized P3HT film. Notably, the thermal conductivity of P3HT films grown at a relatively lower temperature of 45 °C is higher than films grown at 85 °C, as depicted in Fig. 18(e). The enhancement observed in lower temperature growth is attributed to better bond formation and chain alignment.

Wu *et al.*[263] made a liquid crystal co-polyester (CPE) with varying ratios of H-bond donor molecules. Their findings revealed that at an H-bond donor ratio of 80%, the intermolecular forces reached their strongest, resulting in a 25% enhancement in thermal conductivity and a 21-fold increase in strength compared to the CPE without an H-bond donor (Fig. 18(f)).

Kim *et al.*[264] delved into diverse H-bonding strategies employing poly(*N*-acryloyl piperidine) (PAP) as the receptor and introducing polyacrylic acid (PAA), poly(vinyl alcohol) (PVA), and poly(4-vinyl phenol) (PVPh) as donors. Their study revealed a range of interactions, with PAP and PAA forming the strongest hydrogen bond, PAP and PVPh generating a moderate H-bond, and PAP and PVA establishing a weaker H-bond. As depicted in Fig. 18(g), at a PAP mole fraction of 0.3, a peak in thermal conductivity at 1.5 W m^{-1} K^{-1} was observed, about 7.5 times higher than the individual components. This increase is due to the homogeneous distribution of strong H-bonds at a concentration that exceeded the percolation threshold.

Understanding how these molecular interactions affect phonon behavior and thermal transport, coupled with the precision engineering of polymer structures, is crucial in designing polymers with tailored thermal properties. Such advancements pave the way for next-generation materials in various applications, from efficient thermoelectric devices to effective thermal interface materials, demonstrating the impact of molecular-level modifications on macroscopic thermal behavior.

5.6 Covalent cross-linking

Covalent cross-linking refers to forming strong chemical bonds between polymer chains or molecules, creating a 3D network. Introducing cross-linkers to a polymer provides additional thermal transport pathways and restricts chain rotation, bending, and torsion, thereby increasing stiffness. This process introduces a competing effect between introducing additional thermal pathways and increasing stiffness.[265,266] The influence of increased cross-linker density on thermal transport varies with the polymer type. For instance, augmenting cross-linking creates new phonon transport channels in inherently stiff crystalline PE. Here, the incremental stiffness change and its effect on thermal transport are relatively minor. However, the additional channels can interfere with the original ballistic channels, creating phonon scattering centers and thus reducing thermal conductivity.

Conversely, adding new phonon transport channels through cross-linking in an amorphous system does not necessarily reduce thermal conductivity due to the complex and intertwined channel morphology. Specifically for PE,[267] new channels from cross-linking enhance bonded interactions, thus increasing overall thermal conductivity. However, for polystyrene (PS), new phonon transport channels from cross-linking negligibly affect thermal conductivity, a behavior attributed to the strong structural heterogeneity of amorphous PS, which already includes a dense network of phonon transport channels.

Rashidi *et al.*[268] showed that for two cross-linked poly (methyl methacrylate) (PMMA) chains, thermal transport along covalent cross-linkers is insignificant when compared to transport along the backbone. Consequently, the addition of cross-linkers increased thermal conductivity. Intriguingly, the study demonstrated that when the cross-linker is of shorter length, it brings the polymer chains closer, fostering strong non-bonding interactions that, in turn, enhance heat transfer. Fig. 19(a) further illustrates that the contribution of cross-linking interactions to thermal conductivity is 3–10 times higher than that of other covalent interactions, highlighting the significant role of cross-linking in modulating thermal transport in polymers.

Experimentally, Yu *et al.*[269] studied the effect of dicumyl peroxide (DCP) as a cross-linking agent in high-density polyethylene (HDPE). Their findings revealed that as the weight percentage of DCP increases, the polymer's thermal conductivity and crystallinity decreases (Fig. 19(b)). This trend is likely

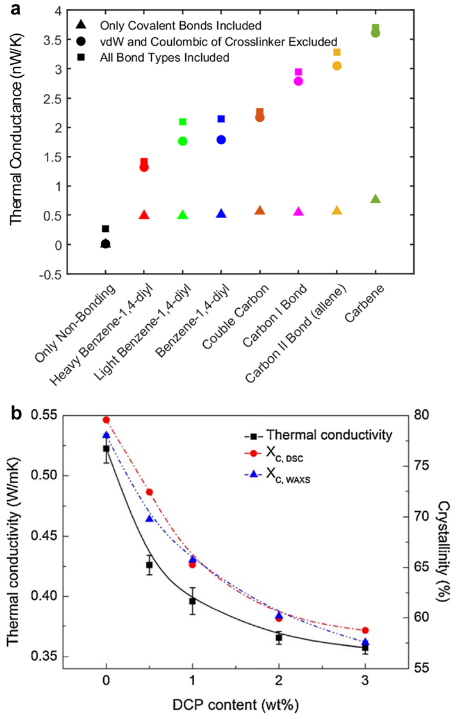

Fig. 19 Effect of cross-linking on thermal conductivity. (a) Thermal conductance of polymer chains with different cross-linking species under different conditions of nonbonding interactions. Reproduced with permission.[268] Copyright, 2017, American Chemical Society – JPCB. (b) Thermal conductivities and crystallinities of pristine and crosslinked HDPE with varying cross-linker (DCP) content. Reproduced with permission.[269] Copyright, 2014, *Thermochimica Acta*.

due to DCP's inhibitory influence on the crystallization process of HDPE, which results in reduced crystalline domain size and overall bulk density, thereby affecting the thermal transport properties of the polymer. These findings underscore the importance of carefully selecting the right combination of crosslinker and polymer to manage the undesirable effects of crosslinking.

5.7 Crystallinity, strain, and stiffness

Generally, increased polymer crystallinity (χ) leads to a monotonous rise in thermal conductivity[271,272] due to the increased phonon transmissivity. However, variations in thermal conductivity across different crystalline structures are attributed to differences in phonon group velocities[273] and relaxation times of different phonon modes.[274,275] Many polymers exhibit a semi-crystalline nature, characterized by a mixture of crystalline and amorphous regions.[276,277] The interface between these regions, known as the interlamellar region, introduces additional phonon scattering due to complex molecular bridges, loops, folds, and tails,[278] as visualized in Fig. 20(a).[279]

Strain in semi-crystalline polymer exists within the interlamellar region, influenced by molecular bridges and loops. An increase in strain typically increases thermal conductivity[257,280,281] as it straightens the loops and folds in the region. However, such an increase might be confined to the strain direction, potentially decreasing the thermal transport in other directions.[282] The impact of strain on thermal conductivity depends on the presence of loops and bridges that can be straightened; therefore, polymers with few bridges will show a minimal effect from strain,[270] as shown in Fig. 20(c). In polymers with low crystallinity and high loop numbers, the increased strain may result in tails and broken chains, reducing molecular weight and thermal conductivity. In contrast, highly crystalline polymers with small interlamellar regions allow for the straightening of loops and bridges without breakage, thus preserving the polymer structure.

For single-chain polymers, strain only pertains to the stretching of bonds in the backbone, which can weaken the bond energies. This weakening leads to increased phonon lifetime and decreased phonon group velocity, both of which influence thermal conductivity in a competing fashion. In unsaturated single-chain hydrocarbons, the effect of strain varies; for example, strain rate does not affect the thermal conductivity of cumulene but increases that of carbyne,[231] as shown in Fig. 20(d). It can be surmised that in cumulene, the improvement in thermal conductivity due to increased phonon relaxation time is counterbalanced by a deterioration in thermal conductivity by decreased phonon group velocity.

Crystallinity and stiffness in polymers are two interconnected physical effects. Typically, a polymer with high crystallinity also demonstrates a high Young's modulus.[111] Crystallinity can only increase the thermal conductivity to the limit of inhibiting molecular interactions. For instance, the carbon–carbon bond with the high covalent bond stiffness would be expected to possess exceptional thermal conductivity. However, the presence of H-bonding[283] and permanent dipoles in polymers with carbon backbones introduces intermolecular interactions that hinder them from achieving phonon transmission efficiency akin to that of crystalline diamonds. A key factor determining the thermal transport in semi-crystalline polymers is persistence length—an intrinsic property characterizing polymer chain stiffness. A larger persistence length facilitates the adoption of an extended chain morphology, leading to significantly increased thermal conductivity. This effect arises from the ability of an extended chain structure to support longer thermal transport channels along the covalently bonded backbone (Fig. 20(b)).

Many experimental studies have investigated the influence of crystallinity,[115,118,241,275,284,285] crystalline size,[114,118,241,284] and stiffness[111,115,286–288] on the thermal conductivity of polymers. Notably, Zhu *et al.*[241] observed that crystallinity reduced with drawing of PE films but still led to increased thermal conductivity. This counterintuitive behavior is attributed to the fact that the decrease in thermal conductivity caused by the reduction of crystallinity is outweighed by the increase in thermal conductivity due to chain alignment caused by the increase in strain. This finding highlights the complex relationship between crystallinity and strain affecting thermal transport properties in polymers. Exceptionally high thermal conductivities of up to 100 W m^{-1} K^{-1} were observed when PE nanofibers were subjected to increased strain through stretching or drawing.[94] As the draw ratio increases, crystallinity[228] and Young's modulus

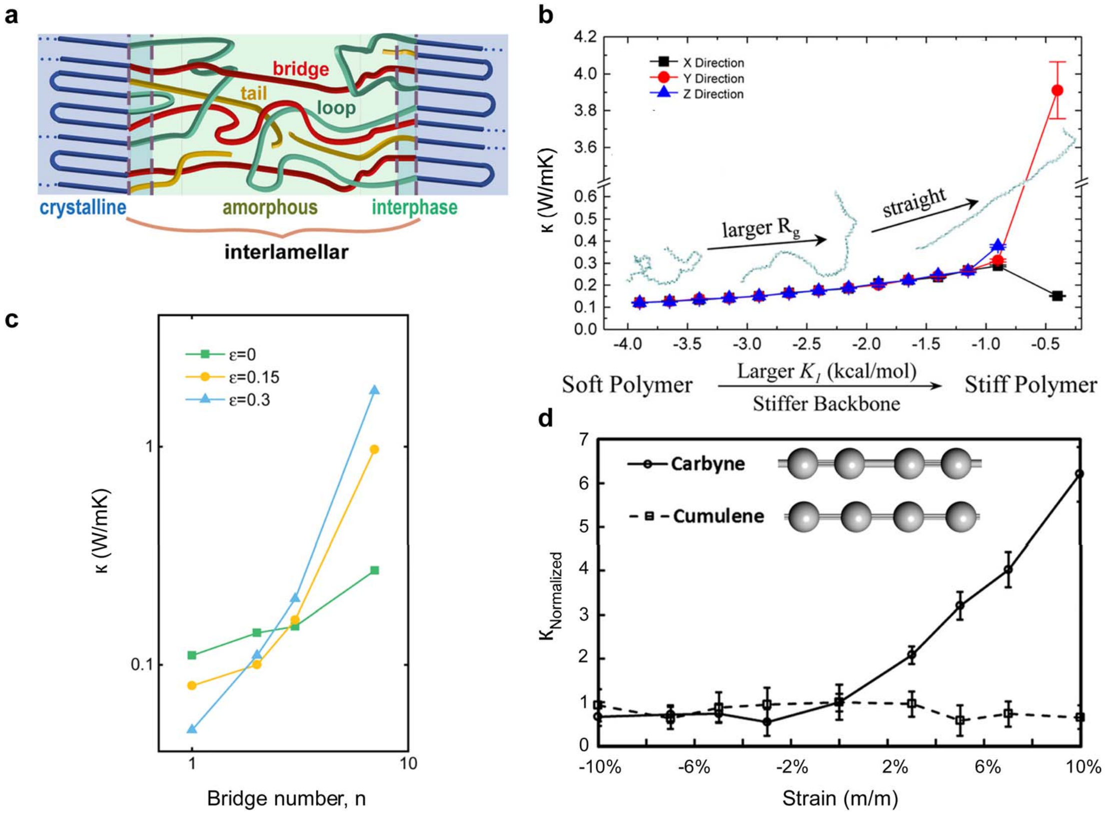

Fig. 20 Effect of stiffness and strain on a polymer. (a) Schematic of interlamellar region showing tail, bridge, and loop. Reproduced with permission.[270] Copyright, 2021, American Institute of Physics – JAP. (b) Change in thermal conductivity for different directions with an increase in energy constant of dihedral angle energy (stiffness of backbone). Reproduced with permission.[262] Copyright, 2016, American Chemical Society – JPCB. (c) Change in thermal conductivity with increasing bridge number in the interlamellar region of the polymer, under different strain rates. Reproduced with permission.[270] Copyright, 2021, American Institute of Physics – JAP. (d) Normalized thermal conductivity as a function of tensile strain for carbyne and cumulene. Reproduced with permission.[231] Copyright, 2015, *Nature*.

increase significantly. Notably, Choy *et al.*[229] measured that a draw ratio 200 for PE tape resulted in a shift of crystallinity from 81.8% to 92.6%, accompanied by a significant increase in thermal conductivity from 1 W m^{-1} K^{-1} to 30 W m^{-1} K^{-1}.

Other than post-synthesis approaches like drawing, annealing, and external pressure to change the crystallinity of polymers, bottom-up synthesis approaches can also alter crystallinity and are often more effective than post-synthesis techniques, which typically increase crystallinity by a few percentage points. Petran *et al.*[289] conducted a notable study involving the synthesis of poly(benzofuran-*co*-arylacteic acid) and poly(tartronic-*co*-glycolic acid) under enzymatic conditions-Novozym-435. This research revealed a remarkable increase in thermal conductivity up to 265%. The enhancement was attributed to the augmentation of crystallinity achieved through enzymatic synthesis conditions.

Furthermore, Lv *et al.*[290] investigated ethylene vitrimer, a unique material with dynamic covalent (B–O) bonds capable of slow exchange reactions at room temperature without needing a catalyst. This exceptional property facilitated gradual crystallization over seven days, resulting in a notable increase in thermal conductivity from 0.1 W m^{-1} K^{-1} to 1 W m^{-1} K^{-1}. This enhancement occurred without any extrinsic influences. These findings exemplify how controlled crystallinity manipulation can offer practical strategies for engineering thermal conductivity in polymer materials.

5.8 Interrelated thermal and charge transport in OSCs: validity of Wiedemann–Franz law

Another topic that has fundamental and practical interest and is worth highlighting here is the study of the Wiedemann–Franz (WF) law in semiconducting polymers. Strong violation of WF law provides insight into the unexplored charge and thermal transport mechanisms in inorganic materials. Furthermore, the definition of Lorentz number $\left(L = \frac{\sigma T}{\kappa_{el}}\right)$ in WF law is part of ZT ($\sim S^2/L$), when charge carrier contribution of thermal conductivity is much higher than phonon contribution ($\kappa_{phonon} \ll \kappa_{el}$).[291] In a free electron gas model, the Lorenz number is given by the Sommerfeld value ($L_0 = 2.45 \times 10^{-8}$ W Ω K^{-2}), and has been consistently observed in inorganic thermoelectric materials.[292] However, organic thermoelectric materials often exhibit a Lorenz number that can deviate significantly from the Sommerfeld value, indicating that the WF law does not strictly apply to organic semiconductors (OSCs).[293]

For charge carrier contribution to thermal conductivity to be observable, electrical conductivity should be greater than

Table 3 Wiedemann–Franz law deviation when $L^* = \kappa \dfrac{L_0}{\sigma T} < 1$

Polymer	σ (S m^{-1})	κ (W m^{-1} K^{-1})	T (K)	$\kappa L_0 \sigma^{-1} T^{-1}$	Ref.
PEDOT:ClO$_4$	7.75×10^4	0.35 ± 0.02	300	0.62	177
PEDOT:PF$_6$	10×10^4	0.22 ± 0.02	300	0.3	177
PEDOT:BTFMSI	20.75×10^4	0.19 ± 0.02	300	0.13	177
PEDOT:PSS	9×10^4	0.52 ± 0.11	297	0.8	165
PEDOT:PSS	9.6×10^4	0.31 ± 0.05	295	0.44	298
P(EtOPV-*co*-PV)	3.5×10^4	0.25	313	0.94	184
PANI:CSA	2.5×10^4	0.02	300	0.11	55
PEDOT (gate)	7.5×10^4	0.35 ± 0.02	300	0.64	168
PEDOT:PSS (MAI treated)	18.7×10^4	0.29 ± 0.02	300	0.2	166
PEDOT:PSS	7.5×10^4	0.37 ± 0.02	300	0.68	158
PEDOT:PSS	12×10^4	0.26 ± 0.03	300	0.3	44

100 S cm^{-1} so that $\kappa_{\text{el}} \sim \kappa_{\text{phonon}}$, since total thermal conductivity is the sum of both ($\kappa = \kappa_{\text{el}} + \kappa_{\text{phonon}}$). Experimentally, it is challenging to separately identify κ_{phonon} and κ_{el} contributions to the total thermal conductivity.[296] With this in mind, experimental measurements with $\sigma > 100$ S cm^{-1} and dimensionless Lorenz number $\left(L^* = \kappa \dfrac{L_0}{\sigma T}\right)$ less than one are tabulated in Table 3. This indicates a WF law violation, even if the phonon contribution is assumed to be zero ($\kappa_{\text{phonon}} = 0$). Consistent L^* values between 0.3 and 0.8 for untreated PEDOT:PSS across different studies suggest a systematic violation of the WF law rather than an experimental error.

To further demonstrate the violation of the WF law when $L^* > 1$, the contribution of phonon thermal conductivity in a polymer is assumed to be between ($0.1 \leq \kappa_{\text{phonon}} \leq 0.6$ W m^{-1} K^{-1}) for all experimental studies that showed $L^* > 1$ with $\kappa_{\text{phonon}} = 0$. Under

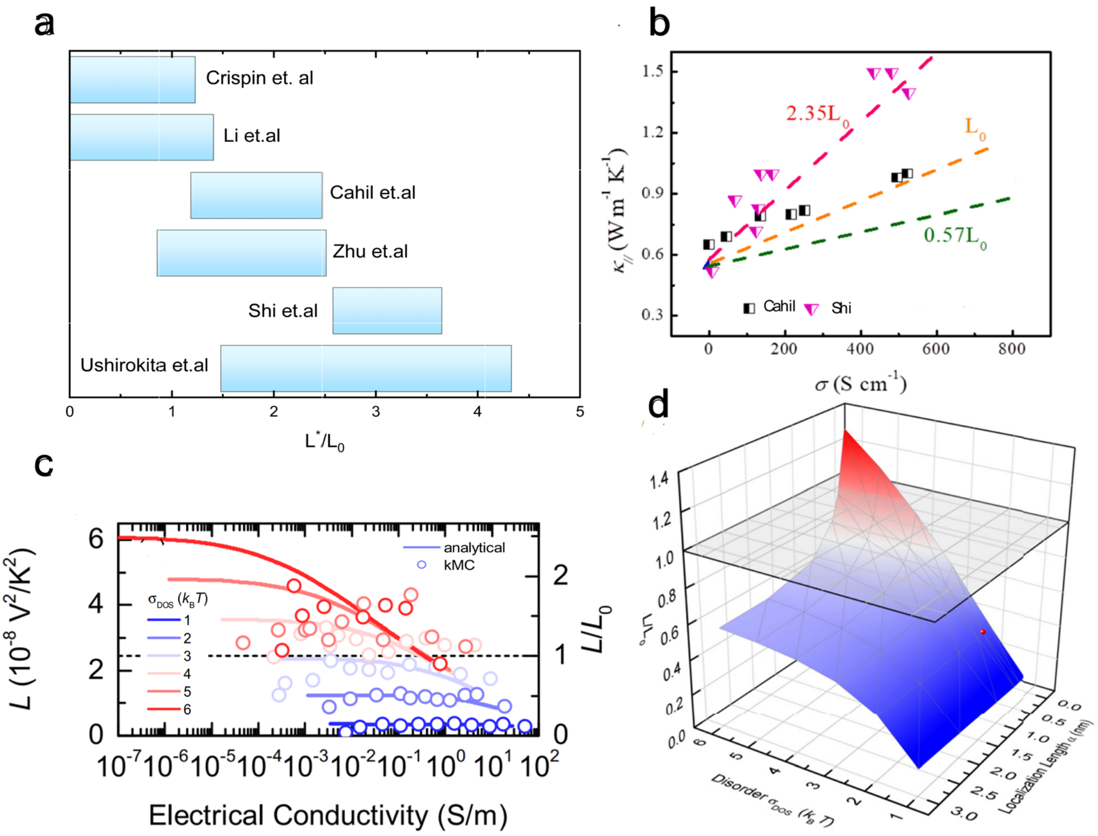

Fig. 21 Wiedemann Franz law in polymeric thermoelectric materials. (a) Range of dimensionless Lorenz number for different experimental studies[54,157,199,294–296] ($\sigma_{\text{min}} > 100$ S cm^{-1}) with respect to the Sommerfield value for a phonon thermal conductivity range of 0.1–0.6 W m^{-1} K^{-1}. (b) Thermal conductivity with varying electrical conductivity for two different studies.[54,296] Reproduced with permission.[291] Copyright, 2022, *Applied Materials Today*. (c) Lorenz number and dimensionless Lorenz number from the analytical model (solid lines) and kinetic Monte Carlo simulations (symbols) for different energetic disorder values; the dashed line is when Lorenz number is same as Sommerfield value, (d) Dimensionless Lorenz number for varying energetic disorder and localization length for a carrier concentration of 0.1. Reproduced with permission.[297] Copyright, 2020, American Physical Society – PRB.

this assumption, a modified Lorenz number is calculated, and a ratio between the Lorenz number and the Sommerfeld value $\left(\frac{L}{L^0}\right)$ is plotted in Fig. 21(a). The results show that the modified Lorenz number can be up to four times greater than the Sommerfeld value, providing further evidence of the WF law's violation in both directions relative to the Sommerfeld value. When $\kappa \sim 1$ W m^{-1} K^{-1}, a thermal conductivity change is observed with changing dopant level or electrical conductivity, as shown in Fig. 21(b), with a constant Lorenz number. This is likely because $\kappa_{\text{el}} > \kappa_{\text{phonon}}$. However, when thermal conductivity is small, no change was observed with changing oxidation level (or electrical conductivity).

Scheunemann and Kemerink[297] conducted theoretical and computational studies to investigate the validity of WF law in organic semiconductors (OSCs) using analytical models and kinetic Monte Carlo (kMC) simulations based on hopping transport mechanisms. Their study varied parameters such as energetic disorder ($\sigma_{\text{DOS}} \sim k_{\text{B}}T$) and charge carrier localization length (α) to understand how these factors influence the Lorenz number. As previously discussed, adding a dopant introduces defects (altering localization lengths) and changes the density of states (DOS), thus modifying the energetic disorder.

Their findings revealed that the Lorenz number in OSCs can deviate from the Sommerfeld value in both directions, being either greater or lower, depending on the charge carrier localization length, energetic disorder, and charge carrier concentration (Fig. 21(d)). A notable observation from their study is that to achieve high electrical conductivity or charge carrier concentration, the σ_{DOS} needs to be very narrow (Fig. 21(c)). Under such conditions, they suggested that a figure of merit (ZT) greater than three could be achievable using OSCs with large localization lengths (greater than 3 nm), $\sigma_{\text{DOS}} = k_{\text{B}}T$, and high electrical conductivity ($\sigma = 1 \times 10^5$ S m^{-1}). However, as electrical conductivity increases, the phonon contribution to thermal conductivity might not remain negligible and could become dominant, mirroring challenges faced in inorganic thermoelectric materials.

The WF law is violated in OSCs. Different polymers have different Lorenz numbers, often determined by their unique amorphous nature and dependent on the synthesis procedure. This indicates that understanding and manipulating these molecular and material characteristics for thermoelectric applications using OSCs is crucial for optimizing performance.

6. External control of thermal transport and thermoelectricity in polymers

Besides the intrinsic effects that affect polymers' transport and thermoelectric properties, recent years have seen an increasing amount of research studying the extrinsic effects and potential dynamic control of thermal transport and thermoelectricity in polymer materials. For thermal transport, environmental effects such as temperature and pressure play a critical role, as they can induce phase transitions that change the molecular conformation and orientation of the backbone. For organic thermoelectricity, the doped state of the conjugated polymer exhibits high sensitivity to external factors, including exposure to air, light, and varying temperatures. We will summarize recent results on the above topics and highlight how these external control capabilities can significantly tune polymer materials' thermal and energy conversion performance.

6.1 Glass transition temperature (T_g)

The glass transition temperature (T_g) is the temperature point at which an amorphous or semi-crystalline polymer transition from a glassy, rigid state to a more rubbery or flexible state (Fig. 22(a)). Below T_g the polymer has low molecular mobility and is an anharmonic lattice, and above T_g it is more mobile and is in a higher disordered state. The change in phonon group velocities during this transition can significantly impact the thermal conductivity of the polymer.[302] Understanding the range of phase transition temperatures is crucial, as it can influence the applicability of highly conductive polymers over a wide temperature range.

Morikawa *et al.*[303] have theoretically studied and shown that bulk polymers exhibit varying thermal conductivity with temperature before reaching T_g. However, the thermal conductivity becomes asymptotic beyond T_g and shows less sensitivity to temperature changes as there are competing effects between phonon group velocity and relaxation time. Utimula *et al.*[299] conducted an in-depth study using *ab initio* methods to analyze the temperature dependence of thermal conductivity in different polymer crystals and fibers. Their findings revealed distinct trends for these two forms of polymers. In polymer crystals, the thermal conductivity tends to increase as the temperature decreases. In contrast, the thermal conductivity for polymer fibers demonstrates a parabolic trend with temperature, often peaking at T_g, as illustrated in Fig. 22(b).

Muthaiah *et al.*[300] conducted a study investigating the impact of temperature on amorphous polyethylene, considering various strain rates. The results demonstrated that the peak thermal conductivity occurs at T_g, and this temperature decreases with increased strain rate (Fig. 22(c)). They explained that increasing strain decreases disorder, allowing anharmonic scattering to dominate at lower temperatures as there will be a crossover from disorder to anharmonicity at T_g.

High-density PE nanofiber has a glass transition temperature close to 100 K, and Shrestha *et al.*[94] have conducted experimental measurements and showed a distinct thermal conductivity peak at this temperature for nanofibers, as illustrated in Fig. 22(d). Contrarily, Robbins *et al.*[284] conducted a study involving bulk PE films and identified a dip in thermal conductivity precisely at T_g, as shown in Fig. 22(e). This observation contradicts the findings from other nanofiber experiments, yet it still suggests a significant structural order alteration occurring at—similarly, Bai *et al.*[301] investigated the thermal conductivity of poly-L-lactide (PLLA) with varying crystallinity. Their results indicated that the peak in thermal conductivity observed at T_g undergoes a less abrupt change for higher crystalline PLLA, as depicted in Fig. 22(f). This

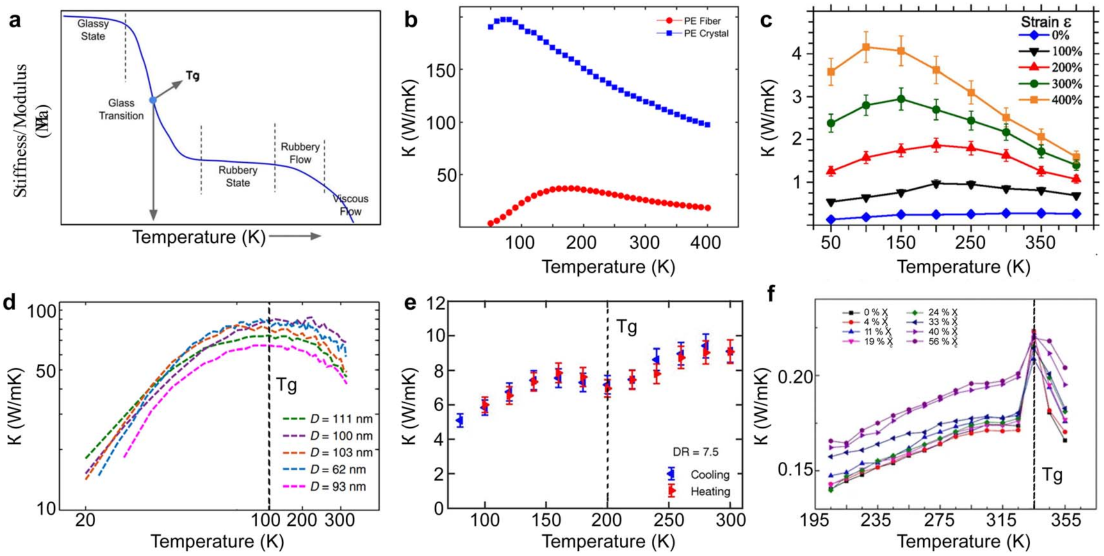

Fig. 22 Effect of glass transition temperature on thermal conductivity. (a) Qualitative plot showing stiffness transition through glass transition temperature; (b) theoretical work: a comparison between PE crystal and PE fiber showing different behavior with changing temperature. Reproduced with permission.[299] Copyright, 2019, American Chemical Society – CM. (c) Theoretical work: amorphous PE thermal conductivity with change in temperature for different strain rates. Reproduced with permission.[300] Copyright, 2018, American Institute of Physics – JAP. (d) Experimental work: thermal conductivity with varying temperatures for ultra-high molecular weight polyethylene nanofibers. Reproduced with permission.[94] Copyright, 2018, *Nature Communications*. (e) Experimental work: thermal conductivity of semi-crystalline polyethylene films showing a dip at glass transition temperature. Reproduced with permission.[284] Copyright, 2019, *Proceedings of the National Academy of Sciences*. (f) Experimental work: effect of crystallinity on thermal conductivity change around glass transition temperature. Reproduced with permission.[301] Copyright, 2018, *Journal of Materials Science*.

observation agrees with the previously discussed theoretical predictions from Utimula *et al.*,[299] showing crystalline materials do not affect T_g.

6.2 External temperature and pressure

External pressure can modify chain packing and increase the crystallinity of a material, while external temperature can alter molecular conformations. However, the direction of change in thermal conductivity with temperature is polymer-dependent due to the various competing factors. Utilizing MD simulations, Zhou *et al.*[43] probed the thermal behavior of two organic compounds, namely *N*,*N*-dicarbazolyl-3,5-benzene (mCP) and *N*,*N*′-diphenyl-*N*,*N*′-di(3-methylphenyl)-(1,1′-biphenyl)-4,4′-diamine (TPD). Their investigation revealed an inverse relationship between thermal conductance and temperature. Conversely, thermal conductance directly correlated with pressure, with elevated pressure enhancing thermal conductivity and thermal diffusivity, attributed to increased phonon group velocity. Concurrently, a decline in specific heat was observed, highlighting the complex interplay of thermal properties under varying environmental conditions.[304]

In an extreme thermal environment, Zhong *et al.*[129] conducted a detailed study on nylon-11 nanofibers subjected to annealing at 500 K. The resultant fibers exhibited substantially lower thermal conductivity than their pre-annealed counterparts. Notably, the unmodified fiber displayed a pronounced peak in thermal conductivity at its glass transition temperature of 330 K, but the peak was absent in annealed fiber. This absence is attributed to the breaking of polymer chains during the annealing process, resulting in shorter chains forming. These shorter chains introduce additional phonon scattering centers, thereby reducing the overall thermal conductivity of the material.

6.3 Dynamic thermal transport in intrinsic polymers

The ability to control thermal pathways can be used to create dynamic and regulatory thermal devices in analogy to electrical devices such as diode,[305] gate, regulator, switch,[306] rectifier,[307,308] memristor, and transistor.[309] One common way to achieve thermal regulation is through molecular structural changes caused by phase transition,[310] which can be achieved from temperature control, light-triggered transitions, and strain. Further, thermal rectification, *i.e.*, thermal diode, can be achieved by having a polymer with two distinct phases, with one phase at the cold end and the other phase at the hot end,[311] leading to directional heat flow similar to that in a semiconductor diode.

6.3.1 Dynamic thermal control *via* temperature-induced phase transition. Shrestha *et al.*[312] demonstrated that polyethylene nanofibers can undergo reversible thermal conductance alterations at a critical transition temperature of 440 K, as shown in Fig. 23(b). Remarkably, they reported a thermal conductance switching ratio as high as 10, surpassing all existing literature for materials undergoing solid-to-solid phase transitions. Nonetheless, it was observed that this thermal switching capability deteriorated over repeated cycles, ceasing entirely after three iterations—a notable study by Li *et al.*[313] employed thermoresponsive aqueous poly(*N*-

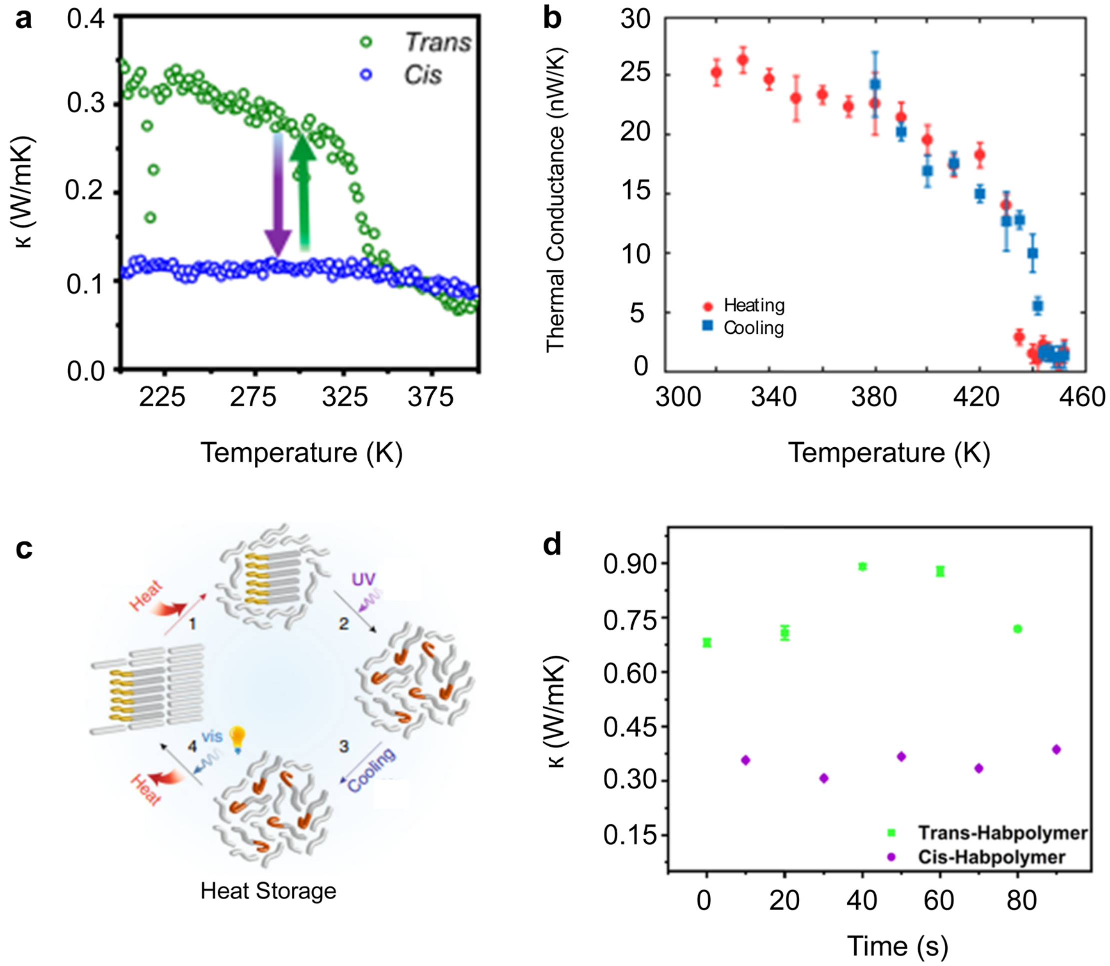

Fig. 23 Dynamic thermal control in polymers. (a) Thermal switching achieved from light-triggered azobenzene. Reproduced with permission.[42] Copyright, 2019, *Proceedings of National Academy of Sciences*. (b) Thermal switching was achieved from the phase transition of polyethylene at 440 K. Reproduced with permission.[312] Copyright, 2019, Science – SA. (c) Thermal storage mechanism using azobenzene. Reproduced with permission.[315] Copyright, 2017, *Nature Communications*. (d) Thermal conductivity switching cycle using light-triggered Habpolymer. Reproduced with permission.[316] Copyright, 2023, American Chemical Society – APM.

isopropylacrylamide) to construct a functional thermal switch operational at ambient conditions, achieving a switching ratio 1.15. Although the switching ratio induced by the higher-order phase transition is modest due to the aqueous nature of the polymer, the thermal switching capability does not deteriorate over several cycles—additionally, Feng *et al.*[314] utilized hydrogel-based polymer poly(*N*-iopropylacrylamide) (PNIPAm) to enact thermal switching at 35 °C, achieving a switching ratio 3.6. This is attributed to reduced water content with temperature, indicated by the shrinking of the hydrogel.

6.3.2 Dynamic thermal control *via* light-triggered phase transition. Several polymer-based molecules exhibit molecular conformation change when exposed to light illumination.[317] For instance, azobenzene molecules transition from the *trans* to the *cis* configuration upon exposure to UV light and revert from *cis* to *trans* upon exposure to green light. Shin *et al.*[42] studied light-triggered thermal conductivity in polymeric azobenzene thin films, demonstrating a switching ratio 3.5 (Fig. 23(a)). Specifically, this configurational change induces alterations in molecular alignment, consequently augmenting phonon scattering events. Notably, the durability of this switching mechanism is unlimited in terms of cycling, highlighting its potential for applications requiring frequent or continuous modulation of thermal properties—further, Wan *et al.*[316] investigated a bulk polymeric material composed of poly-6-(4-(phenyldiazenyl) phenoxy)hexyl methacrylate (referred to as Habpolymer), which, like azobenzene polymer, can be optically toggled between *cis* and *trans* isomeric states using UV and green light. Their findings revealed thermal conductivities switching between 0.78 W m^{-1} K^{-1} and 0.35 W m^{-1} K^{-1} for the *trans* and *cis* configurations, respectively (Fig. 23(d)). Remarkably, the transition between these states could be achieved in less than 10 seconds, highlighting the material's potential for rapid and reversible modulation of thermal properties through optical means. This fast-switching capability, coupled with the significant difference in thermal conductivity between the states, underscores the potential of such materials in dynamic thermal management applications.

6.3.3 Thermal rectification. A thermal rectifier is a device that allows heat to flow preferentially in one direction, like how an electrical diode allows current to flow primarily in one direction. This asymmetric heat flow means the thermal rectifier has a higher thermal conductivity or heat transfer rate in one direction than the opposite direction. Shrestha *et al.*[318] demonstrated the concept of thermal rectification by employing a technique of spatially selective exposure to different irradiation levels *via* a scanning electron microscope. This process allows the manipulation of phase transition temperatures within some regions of the nanofiber. By judiciously controlling the irradiation zones relative to the hot island within the thermal bridge, a rectification factor reaching up to 50% was achieved. Han *et al.*[315] extended the thermal rectification scope to energy storage applications, using a composite of azobenzene and phase change material (Fig. 23(c)). This composite can be activated thermally or through light exposure (UV/visible). Their study illustrated that over 100 optical cycles could be maintained, revealing a straightforward strategy for thermal energy storage *via* light stimuli.

6.4 Tuning polymer thermoelectricity *via* external temperature

The energy conversion efficiency of a thermoelectric material is directly related to the temperature gradient between its hot and cold sides. In the context of using thermoelectric generators (TEGs) to convert human body heat into electricity, the maximum Carnot efficiency noted is about 6%.[319] Additionally, for a thermoelectric material with *ZT* of 1, only about 1% efficiency can be achieved, as illustrated in Fig. 24(a). Consequently, TEGs using body heat are suitable for low-power-demand applications like biosensing.[320]

The temperature dependence of electrical conductivity varies significantly with the degree of disorder and doping in the polymers. In general, conductivity increases with temperature for disordered samples due to thermally activated hopping processes. For samples with a certain degree of structural order, there might be transitions from insulating to metallic behavior as temperature decreases.[140] Here, the temperature dependence on electrical conductivity is broadly classified into four cases depending on the charge transport mechanisms and their activation energy, as shown in Fig. 24(b). Case-(a) represents electrically insulating disordered polymers (because of high activation energy), dominated by thermal hopping transport.[295,321,322] Case-(b) some polymers undergo metal-to-insulator transition as the temperature decreases. This transition is attributed to improved electronic coupling between polymer chains or an increase in the inter-chain localization length of the carriers. Case-(c) here, the polymer is transitioning from insulator to metal as temperature increases.[323,324] The precise mechanism for this transition is not fully understood. However, some models consider the role of three-dimensional metallic regions electronically coupled *via* one-dimensional chains that undergo a decrease in the localization length of the carriers as the temperature decreases. Case-(d) highly doped and ordered conducting polymers that behave like a metal.

Like electrical conductivity, the Seebeck coefficient's dependence on temperature can be classified into seven cases, as shown in Fig. 24(c). Case-(a) conducting polymers with highly p-doped, narrow metallic bands,[325] similar to case-(d) from the electrical conductivity. Case-(b) polymer dominated by electron–phonon interaction,[326] which does not involve the phonon drag effect. Case-(c) characterized by a hump that disappears at higher temperatures, indicative of phonon drag effects in the material.[327–329] Case-(d and e) represents Mott's variable range hopping transport between localized states. This decrease is often characterized by a $T^{1/2}$ dependence. Case-(f) conducting polymers on the insulating side of the metal-insulator transition.[330] This behavior is attributed to the nearest-neighbor hopping thermopower with the Fermi energy within localized states. Case-(g) represents low doping level samples,[331] with low charge carrier density. The cases presented above for Seebeck coefficient and electrical conductivity are generalized, and polymers could be more complex, representing a combination

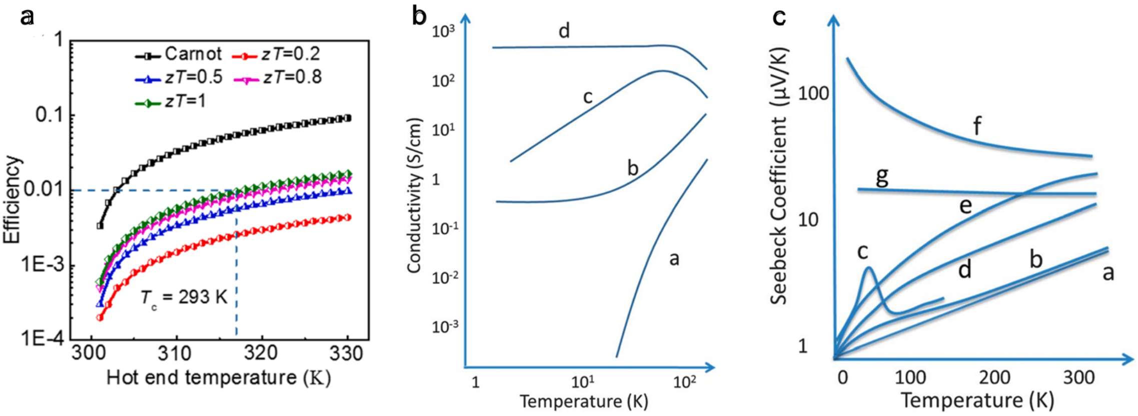

Fig. 24 External temperature effects on thermoelectric polymers. (a) Carnot efficiency and power generation efficiency for materials with different *ZT* with ambient temperature as cold side temperature. Reproduced with permission.[319] Copyright, 2021, *Progress in Material Science*. (b) Different cases for the effect of temperature on electrical conductivity, (c) for the effect of temperature on the Seebeck coefficient. Reproduced with permission.[140] Copyright, 2012, Royal Society of Chemistry – EES.

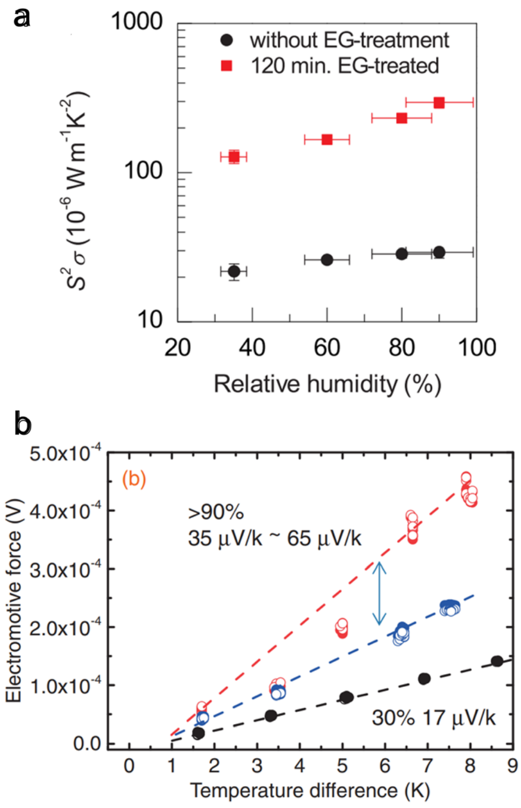

Fig. 25 Effect of relative humidity on thermoelectric properties. (a) The power factor for pristine and 120 min EG-treated PEDOT:PSS films at varying humidity. Reproduced with permission[44] Copyright, 2016 American Physical Society – APL. (b) Thermoelectric voltage for varying temperatures and different humidity variations. Reproduced with permissions.[333] Copyright, 2014, The Japan Society of Applied Physics – APE.

of multiple scenarios with temperature. However, one can conclude that organic thermoelectric properties can increase or decrease with temperature.

6.5 Tuning polymer thermoelectricity *via* humidity effect

Water saturation content varies with humidity levels in the doped conjugated polymer. As water is a high-polar molecule, it can act as a solvent for de-doping and affect thermoelectric properties significantly.[332] Additional water can reduce the coulombic interaction between the PEDOT and PSS chains, facilitating better carrier mobility.[333] Kim *et al.*[44] studied the effect of humidity on the thermoelectric properties of PEDOT:PSS. For films with PSS content (more hydrophilic), the electrical conductivity was observed to decrease with increasing humidity. A higher PSS content leads to greater water absorption, swelling the film and likely increasing the tunneling distance between PEDOT molecules, which reduces electrical conductivity.

On the other hand, PEDOT:PSS EG-treated films have less PSS and hence less water absorption; the electrical conductivity increases with increasing humidity. The increase is attributed to a reduction in the binding energy of mobile holes on PEDOT and possibly due to the re-alignment of PEDOT chains by solvent vapor annealing effects. These factors lead to increased mobility of charge carriers, outweighing the adverse effects of increased tunneling distance due to swelling. However, the Seebeck coefficient increases with humidity, regardless of the PSS content for both pristine and EG-treated PEDOT:PSS films. This increase indicates a reduction in carrier concentration and, potentially, scattering while carrier mobility increases. The overall impact increases the power factor with humidity, as shown in Fig. 25. Varying the humidity of the environment is a promising technique for dynamically controlling the thermoelectric performance of the OSCs.

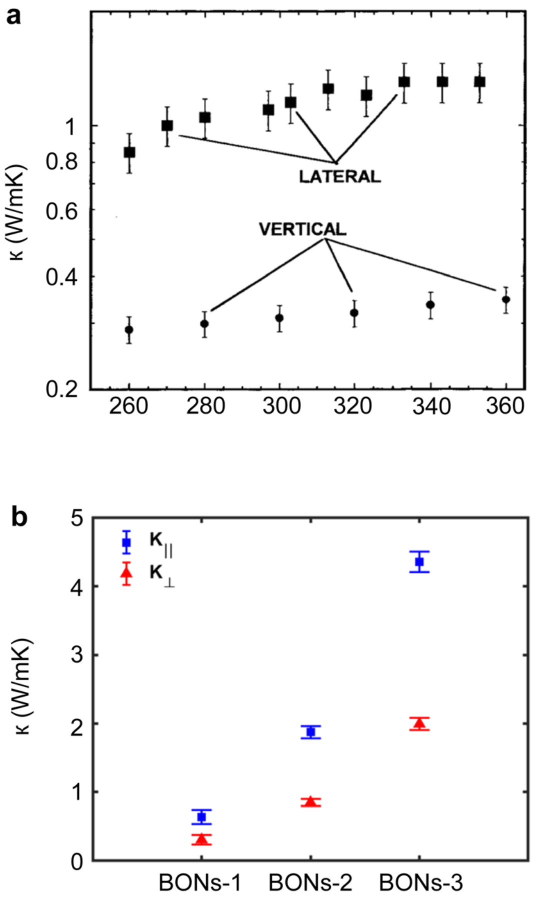

Fig. 26 Homogeneity effects of thermal conductivity. (a) Temperature dependence of thermal conductivity anisotropy of a polymer film with a thickness of 2.25 μm. Reproduced with permission.[125] Copyright, 1999, *Journal of Microelectromechanical Systems*. (b) Thermal conductivity of polyvinylidene (PVDF) film showing near isotropic behavior by engineering the lamellae. BON-1 is 10 MPa, BON-2 is 50 MPa, and BON-3 is 100 Mpa. Reproduced with permission.[334] Copyright, 2023, *Polymers*.

7. Conclusions and outlook

This review presents our theoretical understanding of experimental progress on thermal transport and thermoelectricity in polymer materials based on molecular and nanoscale perspectives. In contrast to the vast amount of literature on charge transport in organic semiconductors and thermal transport and thermoelectric studies in inorganic materials, obtaining the fundamental structure–property-function relationship between molecular-scale constituents and their thermal functions remains an open question. We conclude this review by discussing some open challenges in the field.

7.1 Isotropically high thermal transport in polymers

Amorphous bulk polymers typically exhibit low isotropic thermal conductivity[335] below 0.5 W m^{-1} K^{-1}. In many applications, a high isotropic thermal conductivity is desirable to reject or absorb heat dissipated by the operating devices uniformly. However, commonly used techniques to enhance the thermal conductivity of polymers, such as stretching for chain alignment, modifying backbone, and engineering molecular conformation, tend to result in anisotropic thermal conductivity, with the conductivity along the non-backbone directions maintaining nearly bulk values[125] (Fig. 26(a)). Exacerbating the problem, a study from Choy *et al.*[336] showed that thermal conductivity in a perpendicular direction to stretching decreased below bulk values. In addition, the thickness of the material can also affect thermal transport for thin film polymers. Anharmonic interactions between surface and bulk phonons can reduce the overall in-plane thermal conductivity,[337] suggesting the challenges of designing polymers with high and isotropic thermal conductivity. Recent work by Wang *et al.*[334] explored the thermal conductivity of polyvinylidene (PVDF) films by inducing amorphous nanophases *via* cross-planar arrangements among the in-plane extended chain crystal lamellae. It was achieved by applying pressures up to 100 MPa in the direction opposite to stretching. This resulted in elevated thermal conductivity in both cross-plane (~1.99 W m^{-1} K^{-1}) and in-plane (~4.35 W m^{-1} K^{-1}) orientations, effectively rendering the material near thermally isotropic, as shown in Fig. 26(b). In the future, exploring strategies and design methods that could yield moderate-to-high thermal conductivity across all directions in a polymer is of great interest.

7.2 Nanoscale and single-molecule level study of thermal transport and thermoelectricity in polymers

Determining the ultimate thermal transport and thermoelectric properties of both electrically insulating and semiconducting molecules and polymers is challenging due to the strong heterogeneity in both the structural and energetic distribution. A polymer structure's inherently existing crystalline, amorphous, and crossover regimes naturally possess distinct thermal transport properties. Further, widely studied thermoelectric polymers such as PEDOT:PSS are non-homogeneous material systems with PEDOT-rich and PSS-rich domains. While controlling polymer morphology is challenging, it is essential to perform nanoscale studies to understand polymer structures' spatial heterogeneity and respective transport properties. This can provide insights into the optimal thermal transport and thermoelectricity in polymers. Specifically, the current strategies to improve polymers' *ZT* have focused on understanding electrical conductivity and Seebeck coefficients to maximize the power factor. One can also focus on the molecular design to achieve low thermal conductivity in semiconducting polymers. Reducing thermal conductivity below 0.1 W m^{-1} K^{-1} typically necessitates substantial defects or air gaps within the amorphous polymer structure, akin to those in aerogels. This presents significant challenges in molecular engineering, as it involves balancing between maintaining electrical conductivity while significantly hindering thermal transport, which has yet to be fully explored in OSCs. Molecular design and structuring[338] to optimize *ZT* for inorganic materials have paved the way for materials with *ZT* to be nearly 3.[339,340] Similar strategies are expected to be conducted in organic systems.

7.3 Machine learning (ML) guided material discovery of high-performance thermal and thermoelectric polymers

The morphologically heterogeneous nature of polymers and the complicated interactions within the molecular network make the theoretical prediction of physical properties challenging. In recent years, ML methods have emerged as valuable tools in discovering new polymer materials and enhancing the property prediction of existing materials.[341] Precisely, leveraging existing databases combined with ML algorithms, researchers can predict new polymer materials and structures with desired thermal and mechanical properties. While material discovery *via* computational means without human intervention presents challenges, they can be navigated effectively through techniques such as active learning and autonomous experimentation.[342] This method accelerates experimental cycles with iterative design, synthesis, and testing, all guided by ML. Along this line, thermal conductivity prediction in polymers is approached using methods like random forest (RF) models and Bayesian neural networks (BNNs). RF models, for instance, predict thermal conductivity from descriptors derived from polymer chemistry trained on comprehensive databases like PoLyInfo.[343] Ma *et al.*[344] used an RF model and identified 121 polymers with MD-calculated thermal conductivity above 0.3 W m^{-1} K^{-1}. Alternatively, BNNs are employed to predict thermal conductivity with an understanding of uncertainty, providing a range of possible values rather than a single-point prediction. Wu *et al.*[345] achieved a mean absolute error of 0.0204 W m^{-1} K^{-1} in predicting thermal conductivity using a transferred model from a pre-trained neural network, a 40% improvement compared to a baseline model.

While ML has demonstrated considerable potential in transforming the discovery and prediction of polymer physical properties, the precision and dependability of these forecasts are contingent upon procuring extensive, high-quality datasets.[346] There is a notable need for such data, particularly concerning newly synthesized or underexplored polymers.[347] Advancements in the field require continuous improvement in high-performance computation and high-throughput data acquisition. As these components progressively align, we anticipate an escalation in the influence of ML on polymer thermal science and thermoelectric renewable technologies in the upcoming years.

Author contributions

SY: writing – original draft, conceptualization, and visualization; CM: visualization; LC: writing – review and editing, supervision, and conceptualization.

Conflicts of interest

The authors declare no conflict of interest.

Acknowledgements

We acknowledge support from the National Science Foundation through a grant from the Thermal Transport Processes Program under NSF CAREER Award No. 2239004.

References

1 L. Cui, R. Miao, C. Jiang, E. Meyhofer and P. Reddy, *J. Chem. Phys.*, 2017, **146**, 092201.
2 N. Mehra, L. Mu, T. Ji, X. Yang, J. Kong, J. Gu and J. Zhu, *Appl. Mater. Today*, 2018, **12**, 92–130.
3 D. R. Anderson, *Chem. Rev.*, 1966, **66**, 677–690.
4 A. Henry, *Annu. Rev. Heat Transfer*, 2014, **17**, 485–520.
5 T. Zhang, X. Wu and T. Luo, *J. Phys. Chem. C*, 2014, **118**, 21148–21159.
6 F. DeAngelis, M. G. Muraleedharan, J. Moon, H. R. Seyf, A. J. Minnich, A. J. H. McGaughey and A. Henry, *Nanoscale Microscale Thermophys. Eng.*, 2019, **23**, 81–116.
7 A. Fraleoni-Morgera and M. Chhikara, *Adv. Eng. Mater.*, 2019, **21**, 1801162.
8 S. Liu, J. Duvigneau and G. J. Vancso, *Eur. Polym. J.*, 2015, **65**, 33–45.
9 M. Goel and M. Thelakkat, *Macromolecules*, 2020, **53**, 3632–3642.
10 B. Russ, A. Glaudell, J. J. Urban, M. L. Chabinyc and R. A. Segalman, *Nat. Rev. Mater.*, 2016, **1**, 1–14.
11 N. Lu, L. Li and M. Liu, *Phys. Chem. Chem. Phys.*, 2016, **18**, 19503–19525.
12 C.-P. Feng, F. Wei, K.-Y. Sun, Y. Wang, H.-B. Lan, H.-J. Shang, F.-Z. Ding, L. Bai, J. Yang and W. Yang, *Nano-Micro Lett.*, 2022, **14**, 127.
13 R. Hu, Y. Liu, S. Shin, S. Huang, X. Ren, W. Shu, J. Cheng, G. Tao, W. Xu, R. Chen and X. Luo, *Adv. Energy Mater.*, 2020, **10**, 1903921.
14 Y. Fang, G. Chen, M. Bick and J. Chen, *Chem. Soc. Rev.*, 2021, **50**, 9357–9374.
15 L. Lei, S. Shi, D. Wang, S. Meng, J.-G. Dai, S. Fu and J. Hu, *ACS Nano*, 2023, **17**, 1803–1830.
16 U. Zschieschang, F. Ante, T. Yamamoto, K. Takimiya, H. Kuwabara, M. Ikeda, T. Sekitani, T. Someya, K. Kern and H. Klauk, *Adv. Mater.*, 2010, **22**, 982–985.
17 T. Someya, Z. Bao and G. G. Malliaras, *Nature*, 2016, **540**, 379–385.
18 L. Wang, C. Yang, X. Wang, J. Shen, W. Sun, J. Wang, G. Yang, Y. Cheng and Z. Wang, *Composites, Part A*, 2023, **164**, 107320.
19 Z. He, C. Zhong, S. Su, M. Xu, H. Wu and Y. Cao, *Nat. Photonics*, 2012, **6**, 591–595.
20 L. Shao, A. Raghavan, G.-H. Kim, L. Emurian, J. Rosen, M. C. Papaefthymiou, T. F. Wenisch, M. M. K. Martin and K. P. Pipe, *Int. J. Heat Mass Transfer*, 2016, **101**, 764–771.
21 Q. Zhou, H. Li, C. Du, Z. Ye, L. Liang and G. Chen, *Nano Energy*, 2023, **118**, 109007.
22 Z. Liu and G. Chen, *Adv. Mater. Technol.*, 2020, **5**, 2000049.
23 X.-L. Shi, W.-Y. Chen, T. Zhang, J. Zou and Z.-G. Chen, *Energy Environ. Sci.*, 2021, **14**, 729–764.
24 W. Ren, Y. Sun, D. Zhao, A. Aili, S. Zhang, C. Shi, J. Zhang, H. Geng, J. Zhang, L. Zhang, J. Xiao and R. Yang, *Sci. Adv.*, 2021, **7**, eabe0586.
25 Y. Liu, X. Wang, S. Hou, Z. Wu, J. Wang, J. Mao, Q. Zhang, Z. Liu and F. Cao, *Nat. Commun.*, 2023, **14**, 3058.
26 Y. Hao, X. He, L. Wang, X. Qin, G. Chen and J. Yu, *Adv. Funct. Mater.*, 2022, **32**, 2109790.
27 L. Cui, S. Hur, Z. A. Akbar, J. C. Klöckner, W. Jeong, F. Pauly, S.-Y. Jang, P. Reddy and E. Meyhofer, *Nature*, 2019, **572**, 628–633.
28 P. Reddy, S.-Y. Jang, R. A. Segalman and A. Majumdar, *Science*, 2007, **315**, 1568–1571.
29 M. D. Bartlett, N. Kazem, M. J. Powell-Palm, X. Huang, W. Sun, J. A. Malen and C. Majidi, *Proc. Natl. Acad. Sci. U. S. A.*, 2017, **114**, 2143–2148.
30 J. Chen, X. Huang, B. Sun and P. Jiang, *ACS Nano*, 2019, **13**, 337–345.
31 X. Yu, M. R. Bhatti, X. Ren, P. Steiner, F. Di Sacco, M. Dong, H. Zhang, D. Papageorgiou, G. Portale, C. Kocabas, C. W. M. Bastiaansen, M. Reece, H. Yan and E. Bilotti, *Compos. Sci. Technol.*, 2022, **229**, 109695.
32 Z.-H. Ge, Y. Chang, F. Li, J. Luo and P. Fan, *Chem. Commun.*, 2018, **54**, 2429–2431.
33 C. Huang, X. Qian and R. Yang, *Mater. Sci. Eng., R*, 2018, **132**, 1–22.
34 X. Xu, J. Chen, J. Zhou and B. Li, *Adv. Mater.*, 2018, **30**, 1705544.
35 H. Chen, V. V. Ginzburg, J. Yang, Y. Yang, W. Liu, Y. Huang, L. Du and B. Chen, *Prog. Polym. Sci.*, 2016, **59**, 41–85.
36 X. Yang, C. Liang, T. Ma, Y. Guo, J. Kong, J. Gu, M. Chen and J. Zhu, *Adv. Compos. Hybrid Mater.*, 2018, **1**, 207–230.
37 F. Zhang, Y. Feng and W. Feng, *Mater. Sci. Eng., R*, 2020, **142**, 100580.
38 T. R. Vijaybabu, T. Ramesh, S. Pandipati, S. Mishra, G. Sridevi, C. P. Raja, R. A. Mensah, O. Das, M. Misra, A. Mohanty and K. B. Nb, *Macromol. Mater. Eng.*, 2023, **308**, 2300001.
39 G. Chen, W. Xu and D. Zhu, *J. Mater. Chem. C*, 2017, **5**, 4350–4360.
40 Y. Zhang, W. Wang, F. Zhang, K. Dai, C. Li, Y. Fan, G. Chen and Q. Zheng, *Small*, 2022, **18**, 2104922.
41 V. Raja, Z. Hu and G. Chen, *Compos. Commun.*, 2021, **27**, 100886.
42 J. Shin, J. Sung, M. Kang, X. Xie, B. Lee, K. M. Lee, T. J. White, C. Leal, N. R. Sottos, P. V. Braun and D. G. Cahill, *Proc. Natl. Acad. Sci. U. S. A.*, 2019, **116**, 5973–5978.
43 T. Zhou, Z. Li, Y. Cheng, Y. Ni, S. Volz, D. Donadio, S. Xiong, W. Zhang and X. Zhang, *Phys. Chem. Chem. Phys.*, 2020, **22**, 3058–3065.
44 G.-H. Kim, J. Kim and K. P. Pipe, *Appl. Phys. Lett.*, 2016, **108**, 093301.

45 R. Landauer, *IBM J. Res. Dev.*, 1957, **1**, 223–231.

46 R. Landauer, *Philos. Mag.*, 1970, **21**, 863–867.

47 P. N. Butcher, *J. Phys.: Condens.Matter*, 1990, **2**, 4869.

48 M. Paulsson and S. Datta, *Phys. Rev. B: Condens. Matter Mater. Phys.*, 2003, **67**, 241403.

49 M. H. Garner, H. Li, Y. Chen, T. A. Su, Z. Shangguan, D. W. Paley, T. Liu, F. Ng, H. Li, S. Xiao, C. Nuckolls, L. Venkataraman and G. C. Solomon, *Nature*, 2018, **558**, 415–419.

50 O. Karlström, H. Linke, G. Karlström and A. Wacker, *Phys. Rev. B: Condens. Matter Mater. Phys.*, 2011, **84**, 113415.

51 T. Cao, X.-L. Shi, J. Zou and Z.-G. Chen, *Microstructures*, 2021, **1**, 1–33.

52 Y. Yang, H. Deng and Q. Fu, *Mater. Chem. Front.*, 2020, **4**, 3130–3152.

53 Y. Chen, Y. Zhao and Z. Liang, *Energy Environ. Sci.*, 2015, **8**, 401–422.

54 A. Weathers, Z. U. Khan, R. Brooke, D. Evans, M. T. Pettes, J. W. Andreasen, X. Crispin and L. Shi, *Adv. Mater.*, 2015, **27**, 2101–2106.

55 H. Yan, N. Sada and N. Toshima, *J. Therm. Anal. Calorim.*, 2002, **69**, 881–887.

56 K. K. Lee, A. S. Alexandrov and W. Y. Liang, *Phys. Rev. Lett.*, 2003, **90**, 217001.

57 J. L. Bredas and G. B. Street, *Acc. Chem. Res.*, 1985, **18**, 309–315.

58 X. Zhang and L.-D. Zhao, *J. Materiomics*, 2015, **1**, 92–105.

59 K. Wang, E. Meyhofer and P. Reddy, *Adv. Funct. Mater.*, 2020, **30**, 1904534.

60 Q. Zhang, Y. Sun, W. Xu and D. Zhu, *Adv. Mater.*, 2014, **26**, 6829–6851.

61 N. W. Ashcroft, N. D. Mermin and S. Rodriguez, *Am. J. Phys.*, 1978, **46**, 116–117.

62 F. De Vita, G. Dematteis, R. Mazzilli, D. Proment, Y. V. Lvov and M. Onorato, *Phys. Rev. E*, 2022, **106**, 034110.

63 R. Landauer, *J. Phys.: Condens.Matter*, 1989, **1**, 8099.

64 T. S. Fisher, *Thermal Energy at the Nanoscale*, World Scientific Publishing Company, 2013.

65 J. C. Cuevas and E. Scheer, *Molecular Electronics: an Introduction to Theory and Experiment*, World Scientific, 2nd edn, 2017.

66 B. Gotsmann, A. Gemma and D. Segal, *Appl. Phys. Lett.*, 2022, **120**, 160503.

67 R. Maynard and E. Akkermans, *Phys. Rev. B: Condens. Matter Mater. Phys.*, 1985, **32**, 5440–5442.

68 K. Schwab, E. A. Henriksen, J. M. Worlock and M. L. Roukes, *Nature*, 2000, **404**, 974–977.

69 S. Jezouin, F. D. Parmentier, A. Anthore, U. Gennser, A. Cavanna, Y. Jin and F. Pierre, *Science*, 2013, **342**, 601–604.

70 L. Cui, W. Jeong, S. Hur, M. Matt, J. C. Klöckner, F. Pauly, P. Nielaba, J. C. Cuevas, E. Meyhofer and P. Reddy, *Science*, 2017, **355**, 1192–1195.

71 N. Mosso, U. Drechsler, F. Menges, P. Nirmalraj, S. Karg, H. Riel and B. Gotsmann, *Nat. Nanotechnol.*, 2017, **12**, 430–433.

72 C. Hua, L. Lindsay, X. Chen and A. J. Minnich, *Phys. Rev. B*, 2019, **100**, 085203.

73 G. Chen, *Nat. Rev. Phys.*, 2021, **3**, 555–569.

74 G. Chen, Nanoscale Energy Transport and Conversion: A Parallel Treatment of Electrons, *Molecules, Phonons, and Photons*, Oxford University Press, Oxford, New York, 2005.

75 J. M. Ziman, in *Electrons and Phonons: The Theory of Transport Phenomena in Solids*, ed. J. M. Ziman, Oxford University Press, 2001.

76 I. Pomeranchuk, *Phys. Rev.*, 1941, **60**, 820–821.

77 *Collected Papers of L.D. Landau*, ed. D. Ter haar, Pergamon, 1965, pp. 187–192.

78 P. G. Klemens and F. E. Simon, *Proc. R. Soc. London, Ser. A*, 1997, **208**, 108–133.

79 H. Ma, Y. Ma and Z. Tian, *ACS Appl. Polym. Mater.*, 2019, **1**, 2566–2570.

80 S. Datta, *Quantum Transport: Atom to Transistor*, Cambridge University Press, Cambridge, 2005.

81 W. Kohn and L. J. Sham, *Phys. Rev.*, 1965, **140**, A1133–A1138.

82 P. Giannozzi, S. de Gironcoli, P. Pavone and S. Baroni, *Phys. Rev. B: Condens. Matter Mater. Phys.*, 1991, **43**, 7231–7242.

83 A. Debernardi, S. Baroni and E. Molinari, *Phys. Rev. Lett.*, 1995, **75**, 1819–1822.

84 W. Li, J. Carrete, N. A. Katcho and N. Mingo, *Comput. Phys. Commun.*, 2014, **185**, 1747–1758.

85 D. A. Broido, M. Malorny, G. Birner, N. Mingo and D. A. Stewart, *Appl. Phys. Lett.*, 2007, **91**, 231922.

86 J. Zhang, F. Xu, Y. Hong, Q. Xiong and J. Pan, *RSC Adv.*, 2015, **5**, 89415–89426.

87 F. Müller-Plathe, *J. Chem. Phys.*, 1997, **106**, 6082–6085.

88 T. Terao, E. Lussetti and F. Müller-Plathe, *Phys. Rev. E*, 2007, **75**, 057701.

89 Y. Sheng, Y. Hu, Z. Fan and H. Bao, *Phys. Rev. B*, 2022, **105**, 075301.

90 W. Zhang, T. S. Fisher and N. Mingo, *Numer. Heat Transfer, Part B*, 2007, **51**, 333–349.

91 Y. Meir and N. S. Wingreen, *Phys. Rev. Lett.*, 1992, **68**, 2512–2515.

92 N. Mingo and L. Yang, *Phys. Rev. B: Condens. Matter Mater. Phys.*, 2003, **68**, 245406.

93 X. Wei, Z. Wang, Z. Tian and T. Luo, *J. Heat Transfer*, 2021, **143**, 072101.

94 R. Shrestha, P. Li, B. Chatterjee, T. Zheng, X. Wu, Z. Liu, T. Luo, S. Choi, K. Hippalgaonkar, M. P. de Boer and S. Shen, *Nat. Commun.*, 2018, **9**, 1664.

95 H. Wang, W. Chu and G. Chen, *Adv. Electron. Mater.*, 2019, **5**, 1900167.

96 J. Ding, Z. Li, F. Zhang, Y. Zou and C. Di, in *Organic Thermoelectrics*, John Wiley & Sons, Ltd, 2022, pp. 319–366.

97 M. M. Sadeghi, M. T. Pettes and L. Shi, *Solid State Commun.*, 2012, **152**, 1321–1330.

98 S. Shen, A. Henry, J. Tong, R. Zheng and G. Chen, *Nat. Nanotechnol.*, 2010, **5**, 251–255.

99 J. A. Johnson, A. A. Maznev, J. Cuffe, J. K. Eliason, A. J. Minnich, T. Kehoe, C. M. S. Torres, G. Chen and K. A. Nelson, *Phys. Rev. Lett.*, 2013, **110**, 025901.

100 B.-Y. Cao, Y.-W. Li, J. Kong, H. Chen, Y. Xu, K.-L. Yung and A. Cai, *Polymer*, 2011, **52**, 1711–1715.

101 A. Jain and K. E. Goodson, *J. Heat Transfer*, 2008, **130**(10), 102402.

102 A. Greppmair, B. Stoib, N. Saxena, C. Gerstberger, P. Müller-Buschbaum, M. Stutzmann and M. S. Brandt, *Rev. Sci. Instrum.*, 2017, **88**, 044903.

103 A. Narayanaswamy and N. Gu, *J. Heat Transfer*, 2011, **133**(4), 042401.

104 C. Canetta and A. Narayanaswamy, *Appl. Phys. Lett.*, 2013, **102**, 103112.

105 X. Qian, J. Zhou and G. Chen, *Nat. Mater.*, 2021, **20**, 1188–1202.

106 R. Shrestha, Y. Luan, S. Shin, T. Zhang, X. Luo, J. S. Lundh, W. Gong, M. R. Bockstaller, S. Choi, T. Luo, R. Chen, K. Hippalgaonkar and S. Shen, *Sci. Adv.*, 2019, **5**, eaax3777.

107 P. Jiang, X. Qian and R. Yang, *J. Appl. Phys.*, 2018, **124**, 161103.

108 S. Lee and D. Kim, *Thermochim. Acta*, 2017, **653**, 126–132.

109 V. Singh, T. L. Bougher, A. Weathers, Y. Cai, K. Bi, M. T. Pettes, S. A. McMenamin, W. Lv, D. P. Resler, T. R. Gattuso, D. H. Altman, K. H. Sandhage, L. Shi, A. Henry and B. A. Cola, *Nat. Nanotechnol.*, 2014, **9**, 384–390.

110 H. Fujishiro, M. Ikebe, T. Kashima and A. Yamanaka, *Jpn. J. Appl. Phys.*, 1997, **36**, 5633.

111 X. Wang, V. Ho, R. A. Segalman and D. G. Cahill, *Macromolecules*, 2013, **46**, 4937–4943.

112 Y. Liu, W. Zou, M. Yang, H. Luo, S. Yang, J. Xu and N. Zhao, *Adv. Funct. Mater.*, 2023, **33**, 2303561.

113 J. Ma, Q. Zhang, A. Mayo, Z. Ni, H. Yi, Y. Chen, R. Mu, L. M. Bellan and D. Li, *Nanoscale*, 2015, **7**, 16899–16908.

114 T. Kim, S. X. Drakopoulos, S. Ronca and A. J. Minnich, *Nat. Commun.*, 2022, **13**, 2452.

115 C. L. Choy, Y. W. Wong, G. W. Yang and T. Kanamoto, *J. Polym. Sci., Part B: Polym. Phys.*, 1999, **37**, 3359–3367.

116 S. Ronca, T. Igarashi, G. Forte and S. Rastogi, *Polymer*, 2017, **123**, 203–210.

117 Y. Zhang, X. Zhang, L. Yang, Q. Zhang, M. L. Fitzgerald, A. Ueda, Y. Chen, R. Mu, D. Li and L. M. Bellan, *Soft Matter*, 2018, **14**, 9534–9541.

118 Y. Xu, D. Kraemer, B. Song, Z. Jiang, J. Zhou, J. Loomis, J. Wang, M. Li, H. Ghasemi, X. Huang, X. Li and G. Chen, *Nat. Commun.*, 2019, **10**, 1771.

119 C. L. Choy, Y. Fei and T. G. Xi, *J. Polym. Sci., Part B: Polym. Phys.*, 1993, **31**, 365–370.

120 Z. Li, L. An, S. Khuje, J. Tan, Y. Hu, Y. Huang, D. Petit, D. Faghihi, J. Yu and S. Ren, *Sci. Adv.*, 2021, **7**, eabi7410.

121 M. K. Smith, T. L. Bougher, K. Kalaitzidou and B. A. Cola, *MRS Adv.*, 2017, **2**, 3619–3626.

122 P. Li, S. Yang, T. Zhang, R. Shrestha, K. Hippalgaonkar, T. Luo, X. Zhang and S. Shen, *Sci. Rep.*, 2016, **6**, 21452.

123 L. Dong, Q. Xi, D. Chen, J. Guo, T. Nakayama, Y. Li, Z. Liang, J. Zhou, X. Xu and B. Li, *Natl. Sci. Rev.*, 2018, **5**, 500–506.

124 L. Xiang, Y. Fang, K. Xu, Z. Zheng, J. Dong and Y. Xie, *Int. J. Heat Mass Transfer*, 2022, **193**, 122959.

125 K. Kurabayashi, M. Asheghi, M. Touzelbaev and K. E. Goodson, *J. Microelectromech. Syst.*, 1999, **8**, 180–191.

126 D. Yoon, H. Lee, T. Kim, Y. Song, T. Lee, J. Lee and J. Hun Seol, *Eur. Polym. J.*, 2023, **184**, 111775.

127 A. Shanker, C. Li, G.-H. Kim, D. Gidley, K. P. Pipe and J. Kim, *Sci. Adv.*, 2017, **3**, e1700342.

128 Y. Xu, X. Wang, J. Zhou, B. Song, Z. Jiang, E. M. Y. Lee, S. Huberman, K. K. Gleason and G. Chen, *Sci. Adv.*, 2018, **4**, eaar3031.

129 Z. Zhong, M. C. Wingert, J. Strzalka, H.-H. Wang, T. Sun, J. Wang, R. Chen and Z. Jiang, *Nanoscale*, 2014, **6**, 8283–8291.

130 A. Roy, T. L. Bougher, R. Geng, Y. Ke, J. Locklin and B. A. Cola, *ACS Appl. Mater. Interfaces*, 2016, **8**, 25578–25585.

131 C. Canetta, S. Guo and A. Narayanaswamy, *Rev. Sci. Instrum.*, 2014, **85**, 104901.

132 G. Wang, M. Kudo, K. Daicho, S. Harish, B. Xu, C. Shao, Y. Lee, Y. Liao, N. Matsushima, T. Kodama, F. Lundell, L. D. Söderberg, T. Saito and J. Shiomi, *Nano Lett.*, 2022, **22**, 8406–8412.

133 A. Majumdar, *Annu. Rev. Mater. Sci.*, 1999, **29**, 505–585.

134 L. Cui, R. Miao, K. Wang, D. Thompson, L. A. Zotti, J. C. Cuevas, E. Meyhofer and P. Reddy, *Nat. Nanotechnol.*, 2018, **13**, 122–127.

135 K. Kim, B. Song, V. Fernández-Hurtado, W. Lee, W. Jeong, L. Cui, D. Thompson, J. Feist, M. T. H. Reid, F. J. García-Vidal, J. C. Cuevas, E. Meyhofer and P. Reddy, *Nature*, 2015, **528**, 387–391.

136 L. Cui, W. Jeong, V. Fernández-Hurtado, J. Feist, F. J. García-Vidal, J. C. Cuevas, E. Meyhofer and P. Reddy, *Nat. Commun.*, 2017, **8**, 14479.

137 B. Xu and N. J. Tao, *Science*, 2003, **301**, 1221–1223.

138 M. Bharti, A. Singh, S. Samanta and D. K. Aswal, *Prog. Mater. Sci.*, 2018, **93**, 270–310.

139 H. Shirakawa, E. J. Louis, A. G. MacDiarmid, C. K. Chiang and A. J. Heeger, *J. Chem. Soc. Chem. Commun.*, 1977, 578–580.

140 O. Bubnova and X. Crispin, *Energy Environ. Sci.*, 2012, **5**, 9345–9362.

141 Y. W. Park, C. O. Yoon, B. C. Na, H. Shirakawa and K. Akagi, *Synth. Met.*, 1991, **41**, 27–32.

142 C. K. Chiang, C. R. Fincher, Y. W. Park, A. J. Heeger, H. Shirakawa, E. J. Louis, S. C. Gau and A. G. MacDiarmid, *Phys. Rev. Lett.*, 1977, **39**, 1098–1101.

143 R. Kroon, D. Alemu Mengistie, D. Kiefer, J. Hynynen, J. D. Ryan, L. Yu and C. Müller, *Chem. Soc. Rev.*, 2016, **45**, 6147–6164.

144 Y. Cao, P. Smith and A. J. Heeger, *Synth. Met.*, 1992, **48**, 91–97.

145 J. Wu, Y. Sun, W. Xu and Q. Zhang, *Synth. Met.*, 2014, **189**, 177–182.

146 S. N. Patel, A. M. Glaudell, D. Kiefer and M. L. Chabinyc, *ACS Macro Lett.*, 2016, **5**, 268–272.

147 R. A. Schlitz, F. G. Brunetti, A. M. Glaudell, P. L. Miller, M. A. Brady, C. J. Takacs, C. J. Hawker and M. L. Chabinyc, *Adv. Mater.*, 2014, **26**, 2825–2830.

148 K. Shi, F. Zhang, C.-A. Di, T.-W. Yan, Y. Zou, X. Zhou, D. Zhu, J.-Y. Wang and J. Pei, *J. Am. Chem. Soc.*, 2015, **137**, 6979–6982.

149 Z. Fan and J. Ouyang, *Adv. Electron. Mater.*, 2019, **5**, 1800769.

150 D. M. de Leeuw, M. M. J. Simenon, A. R. Brown and R. E. F. Einerhand, *Synth. Met.*, 1997, **87**, 53–59.

151 C. J. Boyle, M. Upadhyaya, P. Wang, L. A. Renna, M. Lu-Díaz, S. Pyo Jeong, N. Hight-Huf, L. Korugic-Karasz, M. D. Barnes, Z. Aksamija and D. Venkataraman, *Nat. Commun.*, 2019, **10**, 2827.

152 Q. Zhang, Y. Sun, W. Xu and D. Zhu, *Macromolecules*, 2014, **47**, 609–615.

153 A. M. Glaudell, J. E. Cochran, S. N. Patel and M. L. Chabinyc, *Adv. Energy Mater.*, 2015, **5**, 1401072.

154 U. Lang, E. Müller, N. Naujoks and J. Dual, *Adv. Funct. Mater.*, 2009, **19**, 1215–1220.

155 I. E. Jacobs and A. J. Moulé, *Adv. Mater.*, 2017, **29**, 1703063.

156 K. P. Pernstich, B. Rössner and B. Batlogg, *Nat. Mater.*, 2008, **7**, 321–325.

157 O. Bubnova, Z. U. Khan, A. Malti, S. Braun, M. Fahlman, M. Berggren and X. Crispin, *Nat. Mater.*, 2011, **10**, 429–433.

158 H. Park, S. Hwan Lee, F. Sunjoo Kim, H. Hee Choi, I. Woo Cheong and J. Hyun Kim, *J. Mater. Chem. A*, 2014, **2**, 6532–6539.

159 N. Massonnet, A. Carella, O. Jaudouin, P. Rannou, G. Laval, C. Celle and J.-P. Simonato, *J. Mater. Chem. C*, 2014, **2**, 1278–1283.

160 J. L. Blackburn, A. J. Ferguson, C. Cho and J. C. Grunlan, *Adv. Mater.*, 2018, **30**, 1704386.

161 M. Zeng, D. Zavanelli, J. Chen, M. Saeidi-Javash, Y. Du, S. LeBlanc, G. Jeffrey Snyder and Y. Zhang, *Chem. Soc. Rev.*, 2022, **51**, 485–512.

162 N. Wen, Z. Fan, S. Yang, Y. Zhao, T. Cong, S. Xu, H. Zhang, J. Wang, H. Huang, C. Li and L. Pan, *Nano Energy*, 2020, **78**, 105361.

163 O. Bubnova, M. Berggren and X. Crispin, *J. Am. Chem. Soc.*, 2012, **134**, 16456–16459.

164 L. Zhang, H. Deng, S. Liu, Q. Zhang, F. Chen and Q. Fu, *RSC Adv.*, 2015, **5**, 105592–105599.

165 G.-H. Kim, L. Shao, K. Zhang and K. P. Pipe, *Nat. Mater.*, 2013, **12**, 719–723.

166 S. Zhang, Z. Fan, X. Wang, Z. Zhang and J. Ouyang, *J. Mater. Chem. A*, 2018, **6**, 7080–7087.

167 A. J. Heeger, *Angew. Chem., Int. Ed.*, 2001, **40**, 2591–2611.

168 M. Culebras, B. Uriol, C. M. Gómez and A. Cantarero, *Phys. Chem. Chem. Phys.*, 2015, **17**, 15140–15145.

169 T. Park, C. Park, B. Kim, H. Shin and E. Kim, *Energy Environ. Sci.*, 2013, **6**, 788–792.

170 Z. U. Khan, O. Bubnova, M. J. Jafari, R. Brooke, X. Liu, R. Gabrielsson, T. Ederth, D. R. Evans, J. W. Andreasen, M. Fahlman and X. Crispin, *J. Mater. Chem. C*, 2015, **3**, 10616–10623.

171 J. Sun, M.-L. Yeh, B. J. Jung, B. Zhang, J. Feser, A. Majumdar and H. E. Katz, *Macromolecules*, 2010, **43**, 2897–2903.

172 A. Abtahi, S. Johnson, S. M. Park, X. Luo, Z. Liang, J. Mei and K. R. Graham, *J. Mater. Chem. A*, 2019, **7**, 19774–19785.

173 G. Zuo, X. Liu, M. Fahlman and M. Kemerink, *Adv. Funct. Mater.*, 2018, **28**, 1703280.

174 G. Zuo, X. Liu, M. Fahlman and M. Kemerink, *ACS Appl. Mater. Interfaces*, 2018, **10**, 9638–9644.

175 H. Li, E. Plunkett, Z. Cai, B. Qiu, T. Wei, H. Chen, S. M. Thon, D. H. Reich, L. Chen and H. E. Katz, *Adv. Electron. Mater.*, 2019, **5**, 1800618.

176 K. Hiraishi, A. Masuhara, H. Nakanishi, H. Oikawa and Y. Shinohara, *Jpn. J. Appl. Phys.*, 2009, **48**, 071501.

177 M. Culebras, C. M. Gómez and A. Cantarero, *J. Mater. Chem. A*, 2014, **2**, 10109–10115.

178 J. Yamamoto and Y. Furukawa, *J. Phys. Chem. B*, 2015, **119**, 4788–4794.

179 E. Lim, K. A. Peterson, G. M. Su and M. L. Chabinyc, *Chem. Mater.*, 2018, **30**, 998–1010.

180 K. Zuber, M. Fabretto, C. Hall and P. Murphy, *Macromol. Rapid Commun.*, 2008, **29**, 1503–1508.

181 W. Shi, Q. Yao, S. Qu, H. Chen, T. Zhang and L. Chen, *NPG Asia Mater.*, 2017, **9**, e405.

182 J. Hynynen, E. Järsvall, R. Kroon, Y. Zhang, S. Barlow, S. R. Marder, M. Kemerink, A. Lund and C. Müller, *ACS Macro Lett.*, 2019, **8**, 70–76.

183 Y. Hiroshige, M. Ookawa and N. Toshima, *Synth. Met.*, 2006, **156**, 1341–1347.

184 Y. Hiroshige, M. Ookawa and N. Toshima, *Synth. Met.*, 2007, **157**, 467–474.

185 B. T. O'Connor, O. G. Reid, X. Zhang, R. J. Kline, L. J. Richter, D. J. Gundlach, D. M. DeLongchamp, M. F. Toney, N. Kopidakis and G. Rumbles, *Adv. Funct. Mater.*, 2014, **24**, 3422–3431.

186 B. O'Connor, R. J. Kline, B. R. Conrad, L. J. Richter, D. Gundlach, M. F. Toney and D. M. DeLongchamp, *Adv. Funct. Mater.*, 2011, **21**, 3697–3705.

187 S. Nagamatsu, W. Takashima, K. Kaneto, Y. Yoshida, N. Tanigaki, K. Yase and K. Omote, *Macromolecules*, 2003, **36**, 5252–5257.

188 N. Kim, S. Kee, S. H. Lee, B. H. Lee, Y. H. Kahng, Y.-R. Jo, B.-J. Kim and K. Lee, *Adv. Mater.*, 2014, **26**, 2268–2272.

189 X. Crispin, F. L. E. Jakobsson, A. Crispin, P. C. M. Grim, P. Andersson, A. Volodin, C. van Haesendonck, M. Van der Auweraer, W. R. Salaneck and M. Berggren, *Chem. Mater.*, 2006, **18**, 4354–4360.

190 A. Hamidi-Sakr, L. Biniek, S. Fall and M. Brinkmann, *Adv. Funct. Mater.*, 2016, **26**, 408–420.

191 Z. Ye, X. Yang, H. Cui and F. Qiu, *J. Mater. Chem. C*, 2014, **2**, 6773–6780.

192 D. K. Taggart, Y. Yang, S.-C. Kung, T. M. McIntire and R. M. Penner, *Nano Lett.*, 2011, **11**, 125–131.

193 D. M. DeLongchamp, R. J. Kline, Y. Jung, D. S. Germack, E. K. Lin, A. J. Moad, L. J. Richter, M. F. Toney, M. Heeney and I. McCulloch, *ACS Nano*, 2009, **3**, 780–787.

194 L. Deng and G. Chen, *Nano Energy*, 2021, **80**, 105448.

195 B. Russ, M. J. Robb, F. G. Brunetti, P. L. Miller, E. E. Perry, S. N. Patel, V. Ho, W. B. Chang, J. J. Urban, M. L. Chabinyc, C. J. Hawker and R. A. Segalman, *Adv. Mater.*, 2014, **26**, 3473–3477.

196 D. Kiefer, A. Giovannitti, H. Sun, T. Biskup, A. Hofmann, M. Koopmans, C. Cendra, S. Weber, L. J. Anton Koster, E. Olsson, J. Rivnay, S. Fabiano, I. McCulloch and C. Müller, *ACS Energy Lett.*, 2018, **3**, 278–285.

197 R. B. Aïch, N. Blouin, A. Bouchard and M. Leclerc, *Chem. Mater.*, 2009, **21**, 751–757.

198 D. Huang, H. Yao, Y. Cui, Y. Zou, F. Zhang, C. Wang, H. Shen, W. Jin, J. Zhu, Y. Diao, W. Xu, C. Di and D. Zhu, *J. Am. Chem. Soc.*, 2017, **139**, 13013–13023.

199 H. Li, M. E. DeCoster, R. M. Ireland, J. Song, P. E. Hopkins and H. E. Katz, *J. Am. Chem. Soc.*, 2017, **139**, 11149–11157.

200 C.-K. Mai, R. A. Schlitz, G. M. Su, D. Spitzer, X. Wang, S. L. Fronk, D. G. Cahill, M. L. Chabinyc and G. C. Bazan, *J. Am. Chem. Soc.*, 2014, **136**, 13478–13481.

201 B. Endrődi, J. Mellár, Z. Gingl, C. Visy and C. Janáky, *J. Phys. Chem. C*, 2015, **119**, 8472–8479.

202 S. Qu, Q. Yao, B. Yu, K. Zeng, W. Shi, Y. Chen and L. Chen, *Chem.–Asian J.*, 2018, **13**, 3246–3253.

203 O. Bubnova, Z. U. Khan, H. Wang, S. Braun, D. R. Evans, M. Fabretto, P. Hojati-Talemi, D. Dagnelund, J.-B. Arlin, Y. H. Geerts, S. Desbief, D. W. Breiby, J. W. Andreasen, R. Lazzaroni, W. M. Chen, I. Zozoulenko, M. Fahlman, P. J. Murphy, M. Berggren and X. Crispin, *Nat. Mater.*, 2014, **13**, 190–194.

204 W. Ma, K. Shi, Y. Wu, Z.-Y. Lu, H.-Y. Liu, J.-Y. Wang and J. Pei, *ACS Appl. Mater. Interfaces*, 2016, **8**, 24737–24743.

205 L. Deng, X. Huang, H. Lv, Y. Zhang and G. Chen, *Appl. Mater. Today*, 2021, **22**, 100959.

206 F. F. Kong, C. C. Liu, J. K. Xu, F. X. Jiang, B. Y. Lu, R. R. Yue, G. D. Liu and J. M. Wang, *Chin. Phys. Lett.*, 2011, **28**(3), 037201.

207 I. Petsagkourakis, E. Pavlopoulou, G. Portale, B. A. Kuropatwa, S. Dilhaire, G. Fleury and G. Hadziioannou, *Sci. Rep.*, 2016, **6**, 30501.

208 R. M. W. Wolfe, A. K. Menon, T. R. Fletcher, S. R. Marder, J. R. Reynolds and S. K. Yee, *Adv. Funct. Mater.*, 2018, **28**, 1803275.

209 X. Huang, L. Deng, F. Liu, Q. Zhang and G. Chen, *Energy Mater. Adv.*, 2021, **2021**, 1572537.

210 X. Huang, L. Deng, F. Liu, Z. Liu and G. Chen, *Chem. Eng. J.*, 2021, **417**, 129230.

211 J. Duan, J. Ding, D. Wang, X. Zhu, J. Chen, G. Zhu, C. Chen, Y. Yu, H. Liao, Z. Li, C. Di and W. Yue, *Adv. Sci.*, 2023, **10**, 2204872.

212 S. R. Sarath Kumar, N. Kurra and H. N. Alshareef, *J. Mater. Chem. C*, 2016, **4**, 215–221.

213 J. Luo, D. Billep, T. Waechtler, T. Otto, M. Toader, O. Gordan, E. Sheremet, J. Martin, M. Hietschold, D. R. T. Zahn and T. Gessner, *J. Mater. Chem. A*, 2013, **1**, 7576–7583.

214 F. Kong, C. Liu, H. Song, J. Xu, Y. Huang, H. Zhu and J. Wang, *Synth. Met.*, 2013, **185–186**, 31–37.

215 W. Deng, L. Deng, Z. Li, Y. Zhang and G. Chen, *ACS Appl. Mater. Interfaces*, 2021, **13**, 12131–12140.

216 W. Deng, D. Liang, H. Yue, Z. Yichuan and C. Guangming, *Soft Sci.*, 2021, **1**, 1–14.

217 Z. Li, L. Deng, H. Lv, L. Liang, W. Deng, Y. Zhang and G. Chen, *Adv. Funct. Mater.*, 2021, **31**, 2104836.

218 A. Henry, G. Chen, S. J. Plimpton and A. Thompson, *Phys. Rev. B: Condens. Matter Mater. Phys.*, 2010, **82**, 144308.

219 E. Fermi, P. Pasta, S. Ulam and M. Tsingou, *Studies Of The Nonlinear Problems*, Los Alamos National Lab. (LANL), Los Alamos, NM (United States), 1955.

220 D. Segal, A. Nitzan and P. Hänggi, *J. Chem. Phys.*, 2003, **119**, 6840–6855.

221 J.-W. Jiang, J. Zhao, K. Zhou and T. Rabczuk, *J. Appl. Phys.*, 2012, **111**, 124304.

222 M. Simoncelli, N. Marzari and F. Mauri, *Nat. Phys.*, 2019, **15**, 809–813.

223 L. Isaeva, G. Barbalinardo, D. Donadio and S. Baroni, *Nat. Commun.*, 2019, **10**, 3853.

224 J. Liu and R. Yang, *Phys. Rev. B: Condens. Matter Mater. Phys.*, 2012, **86**, 104307.

225 J. C. Klöckner, M. Bürkle, J. C. Cuevas and F. Pauly, *Phys. Rev. B: Condens. Matter Mater. Phys.*, 2016, **94**, 205425.

226 J. C. Klöckner, J. C. Cuevas and F. Pauly, *Phys. Rev. B*, 2018, **97**, 155432.

227 H. D. Pandey and D. M. Leitner, *J. Chem. Phys.*, 2017, **147**, 084701.

228 D. M. Leitner, in *Handbook of Materials Modeling: Applications: Current and Emerging Materials*, ed. W. Andreoni and S. Yip, Springer International Publishing, Cham, 2020, pp. 865–885.

229 X. Wei and T. Luo, *Phys. Chem. Chem. Phys.*, 2019, **21**, 15523–15530.

230 P. Cheng, N. Shulumba and A. J. Minnich, *Phys. Rev. B*, 2019, **100**, 094306.

231 M. Wang and S. Lin, *Sci. Rep.*, 2015, **5**, 18122.

232 A. Henry and G. Chen, *Phys. Rev. Lett.*, 2008, **101**, 235502.

233 C. Yang, S. Raza, X. Li and J. Liu, *J. Phys. Chem. B*, 2023, **127**, 6804–6813.

234 N. Mosso, H. Sadeghi, A. Gemma, S. Sangtarash, U. Drechsler, C. Lambert and B. Gotsmann, *Nano Lett.*, 2019, **19**, 7614–7622.

235 Z. Wang, J. A. Carter, A. Lagutchev, Y. K. Koh, N.-H. Seong, D. G. Cahill and D. D. Dlott, *Science*, 2007, **317**, 787–790.

236 A. Yamanaka, Y. Izumi, T. Kitagawa, T. Terada, H. Sugihara, H. Hirahata, K. Ema, H. Fujishiro and S. Nishijima, *J. Appl. Polym. Sci.*, 2006, **101**, 2619–2626.

237 D. Hands, K. Lane and R. P. Sheldon, *J. Polym. Sci., Polym. Symp.*, 1973, **42**, 717–726.

238 A. Yamanaka and T. Takao, *Int. Scholarly Res. Not.*, 2011, **2011**, e718761.

239 B. Xie, W. Zhao, X. Luo and R. Hu, *Mater. Sci. Eng., R*, 2023, **154**, 100738.

240 J. Shin, M. Kang, T. Tsai, C. Leal, P. V. Braun and D. G. Cahill, *ACS Macro Lett.*, 2016, **5**, 955–960.

241 B. Zhu, J. Liu, T. Wang, M. Han, S. Valloppilly, S. Xu and X. Wang, *ACS Omega*, 2017, **2**, 3931–3944.

242 J. Liu and R. Yang, *Phys. Rev. B: Condens. Matter Mater. Phys.*, 2010, **81**, 174122.

243 A. Shi, Y. Li, W. Liu, J. Lei and Z.-M. Li, *J. Appl. Phys.*, 2019, **125**, 245110.

244 A. Peterlin, *Kolloid Z. Z. Polym.*, 1969, **233**, 857–862.
245 K. Tao, G. Sun, C. Feng, G. Liu, Y. Li, R. Chen, J. Wang and S. Han, *Macromol. Rapid Commun.*, 2023, **44**, 2300060.
246 S. A. Harfenist, S. D. Cambron, E. W. Nelson, S. M. Berry, A. W. Isham, M. M. Crain, K. M. Walsh, R. S. Keynton and R. W. Cohn, *Nano Lett.*, 2004, **4**, 1931–1937.
247 A. S. Nain, C. Amon and M. Sitti, *IEEE Trans. Nanotechnol.*, 2006, **5**, 499–510.
248 R. Shrestha, S. Shen and M. P. de Boer, *Actuators*, 2018, **7**, 71.
249 L. Jing, R. Cheng, M. Tasoglu, Z. Wang, Q. Wang, H. Zhai, S. Shen, T. Cohen-Karni, R. Garg and I. Lee, *Small*, 2023, **19**, 2207015.
250 T. Luo, K. Esfarjani, J. Shiomi, A. Henry and G. Chen, *J. Appl. Phys.*, 2011, **109**, 074321.
251 K. Sasikumar and P. Keblinski, *J. Appl. Phys.*, 2011, **109**, 114307.
252 X. Duan, Z. Li, J. Liu, G. Chen and X. Li, *J. Appl. Phys.*, 2019, **125**, 164303.
253 H. Ma and Z. Tian, *Appl. Phys. Lett.*, 2017, **110**, 091903.
254 B. Liu, Y. Zhou, L. Dong, Q. Lu and X. Xu, *iScience*, 2022, **25**, 105451.
255 D. Luo, C. Huang and Z. Huang, *J. Heat Transfer*, 2018, **140**(3), 031302.
256 H. Ma and Z. Tian, *J. Mater. Res.*, 2019, **34**, 126–133.
257 T. Zhang and T. Luo, *J. Appl. Phys.*, 2012, **112**, 094304.
258 X. Wei, T. Zhang and T. Luo, *Phys. Chem. Chem. Phys.*, 2016, **18**, 32146–32154.
259 L. Zhang, M. Ruesch, X. Zhang, Z. Bai and L. Liu, *RSC Adv.*, 2015, **5**, 87981–87986.
260 H. Subramanyan, W. Zhang, J. He, K. Kim, X. Li and J. Liu, *J. Appl. Phys.*, 2019, **125**, 095104.
261 X. Xie, K. Yang, D. Li, T.-H. Tsai, J. Shin, P. V. Braun and D. G. Cahill, *Phys. Rev. B*, 2017, **95**, 035406.
262 T. Zhang and T. Luo, *J. Phys. Chem. B*, 2016, **120**, 803–812.
263 Y. Wu, K. Wu, F. Xiao, E. Jiao, J. Shi and M. Lu, *J. Appl. Polym. Sci.*, 2023, **140**, e53951.
264 G.-H. Kim, D. Lee, A. Shanker, L. Shao, M. S. Kwon, D. Gidley, J. Kim and K. P. Pipe, *Nat. Mater.*, 2015, **14**, 295–300.
265 X. Xiong, M. Yang, C. Liu, X. Li and D. Tang, *J. Appl. Phys.*, 2017, **122**, 035104.
266 J. N. Tomlinson, D. E. Kline and J. A. Sauer, *Polym. Eng. Sci.*, 1965, **5**, 44–48.
267 G. Kikugawa, T. G. Desai, P. Keblinski and T. Ohara, *J. Appl. Phys.*, 2013, **114**, 034302.
268 V. Rashidi, E. J. Coyle, K. Sebeck, J. Kieffer and K. P. Pipe, *J. Phys. Chem. B*, 2017, **121**, 4600–4609.
269 S. Yu, C. Park, S. M. Hong and C. M. Koo, *Thermochim. Acta*, 2014, **583**, 67–71.
270 J. He and J. Liu, *J. Appl. Phys.*, 2021, **130**, 225101.
271 C. L. Choy, *Polymer*, 1977, **18**, 984–1004.
272 N. Shulumba, O. Hellman and A. J. Minnich, *Phys. Rev. Lett.*, 2017, **119**, 185901.
273 R. C. Zeller and R. O. Pohl, *Phys. Rev. B: Solid State*, 1971, **4**, 2029–2041.
274 L. H. Sperling, *Introduction to Physical Polymer Science*, John Wiley & Sons, Ltd, 2005, pp. 1–28.
275 M. Hattori, *Kolloid Z. Z. Polym.*, 1962, **185**, 27–31.
276 S. Kommandur and S. K. Yee, *J. Polym. Sci., Part B: Polym. Phys.*, 2017, **55**, 1160–1170.
277 C. L. Choy, F. C. Chen and W. H. Luk, *J. Polym. Sci., Polym. Phys. Ed.*, 1980, **18**, 1187–1207.
278 S. Das and M. Muthukumar, *Macromolecules*, 2023, **56**, 393–403.
279 T. Lu, K. Kim, X. Li, J. Zhou, G. Chen and J. Liu, *J. Appl. Phys.*, 2018, **123**, 015107.
280 T. Ito, H. Matsubara, D. Surblys and T. Ohara, *AIP Adv.*, 2022, **12**, 105223.
281 X. Liu, X. Yu, Z. Yang, X. Zhuang, H. Guo, X. Luo, J. Chen, Y. Liang and Y. Chen, *J. Electron. Mater.*, 2023, **52**, 2831–2842.
282 J. He, K. Kim, Y. Wang and J. Liu, *Appl. Phys. Lett.*, 2018, **112**, 051907.
283 A. Henry and G. Chen, *Nanoscale Microscale Thermophys. Eng.*, 2009, **13**, 99–108.
284 A. B. Robbins, S. X. Drakopoulos, I. Martin-Fabiani, S. Ronca and A. J. Minnich, *Proc. Natl. Acad. Sci. U. S. A.*, 2019, **116**, 17163–17168.
285 K. Eiermann, *Kolloid Z. Z. Polym.*, 1965, **201**, 3–15.
286 C. L. Choy, W. H. Luk and F. C. Chen, *Polymer*, 1978, **19**, 155–162.
287 D. B. Mergenthaler, M. Pietralla, S. Roy and H. G. Kilian, *Macromolecules*, 1992, **25**, 3500–3502.
288 Y. Guo, Y. Zhou and Y. Xu, *Polymer*, 2021, **233**, 124168.
289 A. Petran, T. Radu, M. Dan and A. Nan, *Int. J. Mol. Sci.*, 2023, **24**, 7606.
290 G. Lv, X. Li, E. Jensen, B. Soman, Y.-H. Tsao, C. M. Evans and D. G. Cahill, *Macromolecules*, 2023, **56**, 1554–1561.
291 L. Liu, L. Liang, L. Deng, H. Wang and G. Chen, *Appl. Mater. Today*, 2022, **27**, 101496.
292 N. Lu, L. Li, N. Gao and M. Liu, *J. Appl. Phys.*, 2016, **120**, 195108.
293 X. Xu, J. Zhou and J. Chen, *Adv. Funct. Mater.*, 2020, **30**, 1904704.
294 H. Ushirokita and H. Tada, *Chem. Lett.*, 2016, **45**, 735–737.
295 Y. Sun, L. Qiu, L. Tang, H. Geng, H. Wang, F. Zhang, D. Huang, W. Xu, P. Yue, Y. Guan, F. Jiao, Y. Sun, D. Tang, C. Di, Y. Yi and D. Zhu, *Adv. Mater.*, 2016, **28**, 3351–3358.
296 J. Liu, X. Wang, D. Li, N. E. Coates, R. A. Segalman and D. G. Cahill, *Macromolecules*, 2015, **48**, 585–591.
297 D. Scheunemann and M. Kemerink, *Phys. Rev. B*, 2020, **101**, 075206.
298 M. Scholdt, H. Do, J. Lang, A. Gall, A. Colsmann, U. Lemmer, J. D. Koenig, M. Winkler and H. Boettner, *J. Electron. Mater.*, 2010, **39**, 1589–1592.
299 K. Utimula, T. Ichibha, R. Maezono and K. Hongo, *Chem. Mater.*, 2019, **31**, 4649–4656.
300 R. Muthaiah and J. Garg, *J. Appl. Phys.*, 2018, **124**, 105102.
301 L. Bai, X. Zhao, R.-Y. Bao, Z.-Y. Liu, M.-B. Yang and W. Yang, *J. Mater. Sci.*, 2018, **53**, 10543–10553.

302 K. Eiermann and K.-xH. Hellwege, *J. Polym. Sci.*, 1962, **57**, 99–106.

303 J. Morikawa, J. Tan and T. Hashimoto, *Polymer*, 1995, **36**, 4439–4443.

304 P. Andersson and B. Sundqvist, *J. Polym. Sci., Polym. Phys. Ed.*, 1975, **13**, 243–251.

305 G. Wehmeyer, T. Yabuki, C. Monachon, J. Wu and C. Dames, *Appl. Phys. Rev.*, 2017, **4**, 041304.

306 J. A. Tomko, A. Pena-Francesch, H. Jung, M. Tyagi, B. D. Allen, M. C. Demirel and P. E. Hopkins, *Nat. Nanotechnol.*, 2018, **13**, 959–964.

307 A. L. Cottrill, S. Wang, A. T. Liu, W.-J. Wang and M. S. Strano, *Adv. Energy Mater.*, 2018, **8**, 1702692.

308 H. Ma and Z. Tian, *Nano Lett.*, 2018, **18**, 43–48.

309 N. Li, J. Ren, L. Wang, G. Zhang, P. Hänggi and B. Li, *Rev. Mod. Phys.*, 2012, **84**, 1045–1066.

310 T. Zhang and T. Luo, *ACS Nano*, 2013, **7**, 7592–7600.

311 T. Zhang and T. Luo, *Small*, 2015, **11**, 4657–4665.

312 R. Shrestha, Y. Luan, S. Shin, T. Zhang, X. Luo, J. S. Lundh, W. Gong, M. R. Bockstaller, S. Choi, T. Luo, R. Chen, K. Hippalgaonkar and S. Shen, *Sci. Adv.*, 2019, **5**, eaax3777.

313 C. Li, Y. Ma and Z. Tian, *ACS Macro Lett.*, 2018, **7**, 53–58.

314 H. Feng, N. Tang, M. An, R. Guo, D. Ma, X. Yu, J. Zang and N. Yang, *J. Phys. Chem. C*, 2019, **123**, 31003–31010.

315 G. G. D. Han, H. Li and J. C. Grossman, *Nat. Commun.*, 2017, **8**, 1446.

316 L. Wan, X. Min, W. Yue, F. Lin, J. Feng, X. Liu, D. She, C. Wang, Z. Huang and L. Wang, *ACS Appl. Polym. Mater.*, 2023, **5**, 6540–6548.

317 L. Wan, F. Lin, W. Yue, J. Feng, X. Liu, X. Min, C. Wang and Z. Huang, *J. Mater. Sci.*, 2023, **58**, 5072–5085.

318 R. Shrestha, Y. Luan, X. Luo, S. Shin, T. Zhang, P. Smith, W. Gong, M. Bockstaller, T. Luo, R. Chen, K. Hippalgaonkar and S. Shen, *Nat. Commun.*, 2020, **11**, 4346.

319 S. Xu, X.-L. Shi, M. Dargusch, C. Di, J. Zou and Z.-G. Chen, *Prog. Mater. Sci.*, 2021, **121**, 100840.

320 G. Schwartz, B. C.-K. Tee, J. Mei, A. L. Appleton, D. H. Kim, H. Wang and Z. Bao, *Nat. Commun.*, 2013, **4**, 1859.

321 C. Liu, B. Lu, J. Yan, J. Xu, R. Yue, Z. Zhu, S. Zhou, X. Hu, Z. Zhang and P. Chen, *Synth. Met.*, 2010, **160**, 2481–2485.

322 Y. Sun, P. Sheng, C. Di, F. Jiao, W. Xu, D. Qiu and D. Zhu, *Adv. Mater.*, 2012, **24**, 932–937.

323 S. Qu, Q. Yao, L. Wang, Z. Chen, K. Xu, H. Zeng, W. Shi, T. Zhang, C. Uher and L. Chen, *NPG Asia Mater.*, 2016, **8**, e292.

324 K. Lee, S. Cho, S. Heum Park, A. J. Heeger, C.-W. Lee and S.-H. Lee, *Nature*, 2006, **441**, 65–68.

325 C. O. Yoon, M. Reghu, D. Moses and A. J. Heeger, *Phys. Rev. B: Condens. Matter Mater. Phys.*, 1994, **49**, 10851–10863.

326 A. B. Kaiser, *Phys. Rev. B: Condens. Matter Mater. Phys.*, 1987, **35**, 4677–4681.

327 T. H. Gilani and T. Ishiguro, *Synth. Met.*, 1997, **84**, 845–846.

328 C. Nath, A. Kumar, Y.-K. Kuo and G. S. Okram, *Appl. Phys. Lett.*, 2014, **105**, 133108.

329 Z. Fan, D. Du, Z. Yu, P. Li, Y. Xia and J. Ouyang, *ACS Appl. Mater. Interfaces*, 2016, **8**, 23204–23211.

330 O. E. Parfenov and F. A. Shklyaruk, *Semiconductors*, 2007, **41**, 1021–1026.

331 T. E. Whall, *J. Phys. C: Solid State Phys.*, 1981, **14**, L887.

332 Q. Zhang, Y. Sun, W. Xu and D. Zhu, *Energy Environ. Sci.*, 2012, **5**, 9639–9644.

333 Q. Wei, M. Mukaida, K. Kirihara, Y. Naitoh and T. Ishida, *Appl. Phys. Express*, 2014, **7**, 031601.

334 Q. Wang, S. Liu, H. Guo, B. Hu, Y. Li, J. Wang and B. Li, *Polymers*, 2023, **15**, 2331.

335 Y. Lu, J. Liu, X. Xie and D. G. Cahill, *ACS Macro Lett.*, 2016, **5**, 646–650.

336 C. L. Choy, E. L. Ong and F. C. Chen, *J. Appl. Polym. Sci.*, 1981, **26**, 2325–2335.

337 M. Morita and T. Shiga, *Phys. Rev. B*, 2021, **103**, 195418.

338 M. S. Dresselhaus, G. Chen, M. Y. Tang, R. G. Yang, H. Lee, D. Z. Wang, Z. F. Ren, J.-P. Fleurial and P. Gogna, *Adv. Mater.*, 2007, **19**, 1043–1053.

339 J. Wei, L. Yang, Z. Ma, P. Song, M. Zhang, J. Ma, F. Yang and X. Wang, *J. Mater. Sci.*, 2020, **55**, 12642–12704.

340 J. He and T. M. Tritt, *Science*, 2017, **357**, eaak9997.

341 T. B. Martin and D. J. Audus, *ACS Polym. Au*, 2023, **3**, 239–258.

342 X. Qian and R. Yang, *Mater. Sci. Eng., R*, 2021, **146**, 100642.

343 S. Otsuka, I. Kuwajima, J. Hosoya, Y. Xu and M. Yamazaki, in *2011 International Conference on Emerging Intelligent Data and Web Technologies*, 2011, pp. 22–29.

344 R. Ma, H. Zhang and T. Luo, *ACS Appl. Mater. Interfaces*, 2022, **14**, 15587–15598.

345 S. Wu, Y. Kondo, M. Kakimoto, B. Yang, H. Yamada, I. Kuwajima, G. Lambard, K. Hongo, Y. Xu, J. Shiomi, C. Schick, J. Morikawa and R. Yoshida, *npj Comput. Mater.*, 2019, **5**, 1–11.

346 M. Li, L. Dai and Y. Hu, *ACS Energy Lett.*, 2022, **7**, 3204–3226.

347 C. Yan and G. Li, *Adv. Intell. Syst.*, 2023, **5**, 2200243.